UNIVERSITY OF OKLAHOMA

GRADUATE COLLEGE

MODELING STELLAR SURFACE FEATURES WITH HIGH-PRECISION
PHOTOMETRY

A DISSERTATION

SUBMITTED TO THE GRADUATE FACULTY

in partial fulfillment of the requirements for the

Degree of

DOCTOR OF PHILOSOPHY

By

MARIA SCHUTTE
Norman, Oklahoma
2023

MODELING STELLAR SURFACE FEATURES WITH HIGH-PRECISION PHOTOMETRY

A DISSERTATION APPROVED FOR THE
HOMER L. DODGE DEPARTMENT OF PHYSICS AND ASTRONOMY

BY

Dr. Mukremin Kilic, Chair

Dr. John Wisniewski, Co-Chair

Dr. Doerte Blume

Dr. Nathan Kaib

Dr. Keri Kornelson

Dr. Leslie Hebb

To my family, I am *so* proud that I get to call you all my family and my best friends. I

would not be where I am today without you.

Acknowledgements

This work was done in collaboration with many co-authors who were critical to the completion of this research. Please refer to the beginning of each chapter for the list of co-authors for that specific research paper.

I would like to especially thank my research advisors Dr. John Wisniewski and Dr. Leslie Hebb for mentoring and guiding me throughout my graduate school career. I would also like to thank all of my amazing friends, family, teachers, and classmates for helping to broaden my scientific horizons and for providing the motivation to get me through the last six years.

Table of Contents

List of Tables

List of Figures

Abstract

Starspots are a major source of stellar contamination in transmission spectroscopy of exoplanet atmospheres, and the correction for exoplanet analyses depends on the temperature of the starspots and the covering fraction. Using high-precision data from both space-based and ground-based observatories, we use the starspot modeling program `STSP` to measure the position and size of stellar surface features on KOI-340, an eclipsing binary consisting of G-type subgiant with an M-dwarf companion and TOI-3884, an M dwarf with a planetary companion. `STSP` uses a novel technique to measure the spot positions and radii by using the transiting secondary as a magnifying glass to probe down to less than 1% changes in the surface brightness of the star for high-precision photometry. Our published results on the starspot properties of KOI-340, and our preliminary starspot modeling results for TOI-3884 are presented here. One necessary component to all of our analyses is the contrast of the spot which is related to the spot temperature, photosphere temperature, and the filter of the observed transit. With known spot position and radius, simultaneous multi-filter transits will show different spot signatures that can only be attributed to differences in the contrast (or temperature) of the spot. We have developed a technique to compare the contrast found using simultaneous multi-filter transits to theoretically determined contrast curves, which are determined by interpolating synthetic spectra over a given filter for both the stellar photosphere and a range of spot temperatures. We introduce this technique for HAT-P-11, a K-dwarf with known spot properties and a high-precision (diffuser-aided) simultaneous multi-filter transit obtained using the MuSCAT3 instrument on LCOGT's 2-m telescope at Haleakala Observatory.

Chapter 1

Introduction

1.1 Magnetic Fields and The Sun

1.1.1 Magnetic Fields of Stars

Magnetic fields and their subsequent effects are a key component to the structure and evolution of stars. Stars are made up of extremely hot and dense plasma that can act as a fluid [20]. For all stars, the core of the star is the densest region with the density lowering as you move to the surface of the star. Low mass stars that lie above the fully convective boundary (0.35 $M_\odot$ < M < 1.5 $M_\odot$ [21]), like the Sun, transport the energy being produced in the dense core of the star through radiation, so the energy transport mechanism works through radiative transfer processes where the photons move in a random walk fashion [22]. Once the temperature and density in the interior of the star is low enough to act more like fluid, the type of energy transport changes to convection until the star's surface (photosphere) is reached, so the photons are now being moved via convection cells where the hotter, denser plasma moves up and the cooler, less dense plasma moves down just like the bubbles when water boils, this is called the Solar Dynamo [22]. When hot, ionized plasma moves in this fashion, magnetic fields are generated both on a small single convection cell basis and a large bulk stellar motion basis. The primary driver of the bulk motion of the star is the rotation of the star, which is started when the star itself is forming from the gravitational collapse of a cold, dense, molecular cloud [20]. The rotational period of the star then increase as the star continues to collapse and get smaller as the angular momentum must be conserved, and once the star reaches the main sequence, it maintains its rotation period until the radius of the star once again changes as the star starts to die [22]. While the star is on the main sequence however, its rotation combined with the convective nature of the plasma under the surface of the star creates a number of phenomena, referred to generally as "activity", that can be seen by observing the star. These phenomena all arise from some form of interplay between magnetic field lines themselves or between magnetic fields and other matter [22]. While it is well known that active regions form because of magnetic fields and ionized plasma flow, the exact mechanism that drives the formation of sunspots and other active regions is still unknown and an active area of research [23].

1.1.2 Sunspots and Their Structure

When there is magnetic activity that inhibits the convection occurring in small portions of the photosphere, the photosphere in that section will appear darker compared to the rest of the photosphere, i.e. a starspot or sunspot for the Sun [24]. Sunspots have been observed for over 2000 years, and once telescopes had been invented, Galileo and others in the 1600s observed sunspots moving across the surface of the Sun, which became the first evidence that the Sun was rotating [23]. Sunspots have complex structures that consist of a darker central region called the umbra and a lighter outer ring called a penumbra, and they are often circular in shape though they are usually asymmetric (see Figure 1.1 for an image of an active region with multiple sunspots) [20]. The contrast of sunspots can range from 0.5-0.8 in the umbra to 0.15-0.25 in the penumbra, where the contrast of a spot is a measure of the flux of the spot region to the flux of the star's warmer photosphere (i.e. a spot with a contrast of 1 is perfectly dark) [23]. Sunspots also tend to form in groups that are referred to as groups, complexes, or networks [24]. We have also known that sunspots are variable on a cycle since the 1800s with sunspot activity moving from no sunspots at all on the Sun during Solar minimums to 10s of sunspots during Solar maximum periods [23]. Additionally, during this Solar cycle, sunspots appear at higher latitudes earlier in the cycle and move closer to the equator as the cycle progresses, as seen in the "butterfly" diagrams (see Figure 1.2) [11]. While sunspots do move in latitude during the course of the Solar cycle, they typically appear at only the two active latitudes which start at up to 40° on either side of the equator. Sunspots do eventually disappear or decay, and though the exact decay rate equation is not agreed upon, they will decay within days or weeks typically [25].

1.1.3 Other Magnetic Activity on Sun

Sunspots are only one sign of magnetic activity occurring on or starting from the surface of the Sun. Indeed, all of the magnetic activity signatures that are observed on the Sun are interconnected as they are all formed from the same process [24]. As a whole, these regions of magnetic activity are called active regions because they consist of darker regions of the photosphere (sunspots), brighter regions of the photosphere (faculae, see Figure 1.3), bursts of plasma from the photosphere (flares and prominences), and large bursts of energy that interact with the extremely hot corona that surrounds the Sun (coronal mass ejections) [24]. Figure 1.4 shows an image of multiple prominences and flares on the Sun observed in the ultraviolet (UV) as they are higher energy activity signatures. Each signature is unique, but they are all connected, which means a coronal mass ejection (CME) is linked to an active region on the surface of the star, like a sunspot or flare [22]. Since we know that the smaller
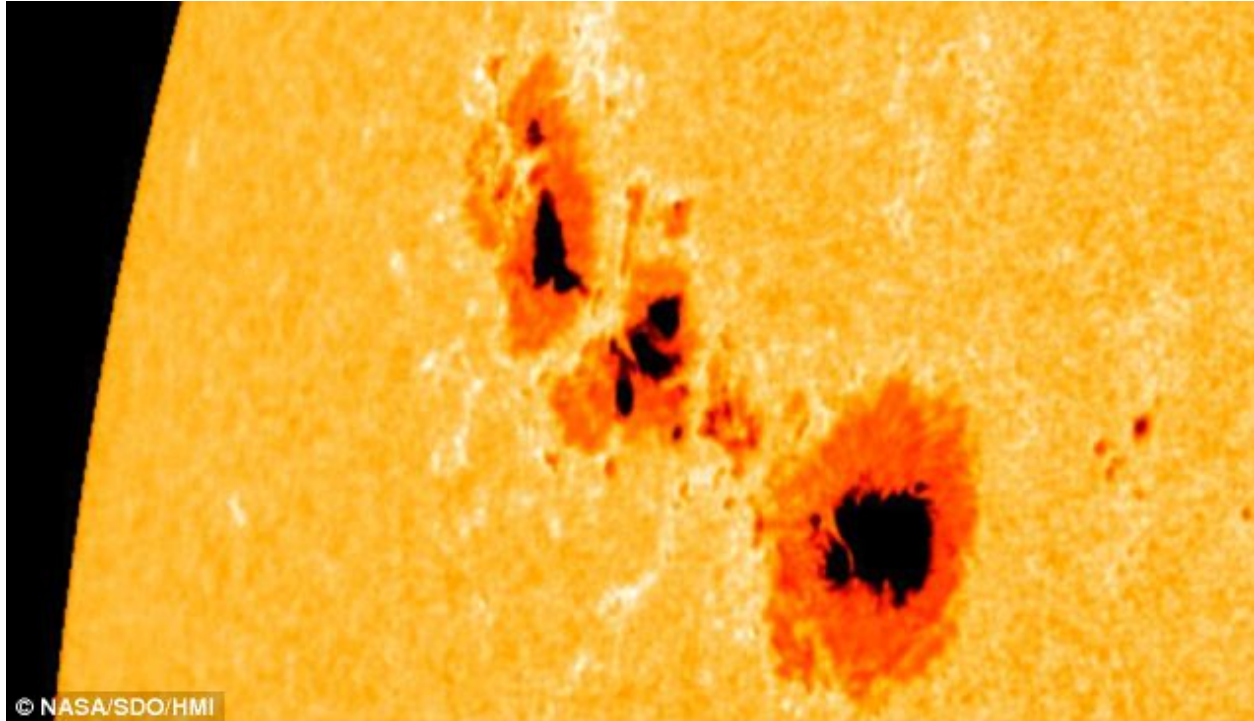
Figure 1.1: Image of an active region from NASA's Solar Dynamics Observatory (SDO) in 2011, specifically active region 1302. In this image, the darkest central part of each sunspot is the umbra, and the less dark region surrounding the umbra is the penumbra, which is larger in area. Also, this image shows that sunspots are not perfect circles and tend to form in groups, which is seen the easiest with the middle sunspot group that has multiple umbral regions. Courtesy of NASA/SDO and the AIA, EVE, and HMI science teams.
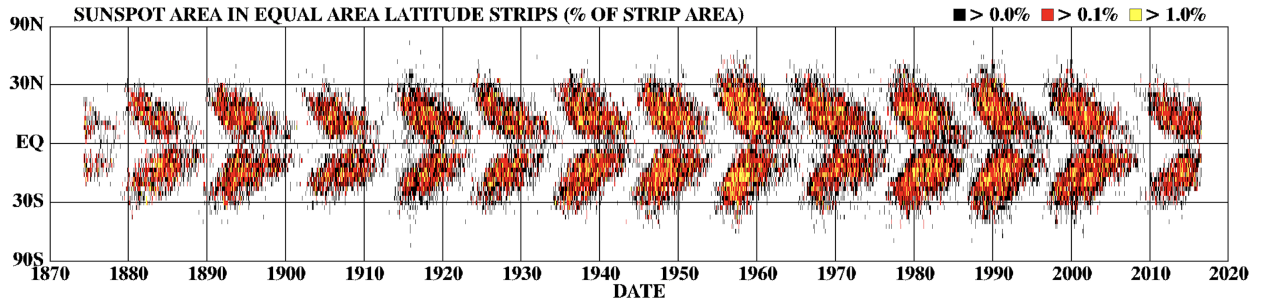
Figure 1.2: Observations of sunspots from the Royal Greenwich Observatory (RGO) started in 1874 and include measurements of the size (percent of the latitude strip in this case) and position (latitude on the Sun's surface). This "butterfly" diagram plots the latitude of each sunspot versus the day it was observed from 1875 to 2016. The color of each point corresponds to the percent of the latitude strip area of each spot, which is used as the sunspot size indicator. For this diagram, the large sunspots are yellow, with the smallest sunspots in black and red in the middle. It is called a "butterfly" diagram because of the shape the sunspots make over time looks like a butterfly. This indicates that sunspots form at higher latitudes in equal numbers on the either side of the Sun's equator, and then, they form more towards the equator as the Solar cycle continues in time. This diagram also shows the sunspot cycle as the sunspots form then disappear and reappear over the course of approximately 11 years. Courtesy of NASA's Marshall Space Flight Center (data available at http://solarscience.msfc.nasa.gov/).

scale activity signatures on the Sun like spots and faculae are connected to the larger scale activity like CMEs, it is necessary to study both small and large scale magnetic activity in order to fully understand the magnetic dynamo of the Sun. In theory since most low mass stars have a similar interior structure with a radiative zone near the core surrounded by a convective zone, low mass stars should all have similar magnetic activity properties, and many low mass stars exhibit similar activity features like spots [3] and flares [26] though there no CMEs have been observed thus far [20]. Once stars drop below a mass of $\sim$ 0.35 $M_\odot$, they become fully convective with no radiative zone, but even fully convective stars should exhibit the same types of magnetic activity as the convection is driving the active regions [21]. For high mass stars, the story is much different because they have a convective zone around the core and then a radiative zone right underneath the photosphere [20], and therefore, I will focus on low mass stars.

1.2   Methods for Measuring Starspots on Other Stars

While we can resolve sunspots easily, it is not trivial to measure spot properties on other stars. In general, there are two main properties of starspots that are measured: (1) spot temperature (or contrast) and (2) the covering fraction. In addition to studying the magnetic activity of stars other than the Sun, there is another key benefit to measuring these properties

4
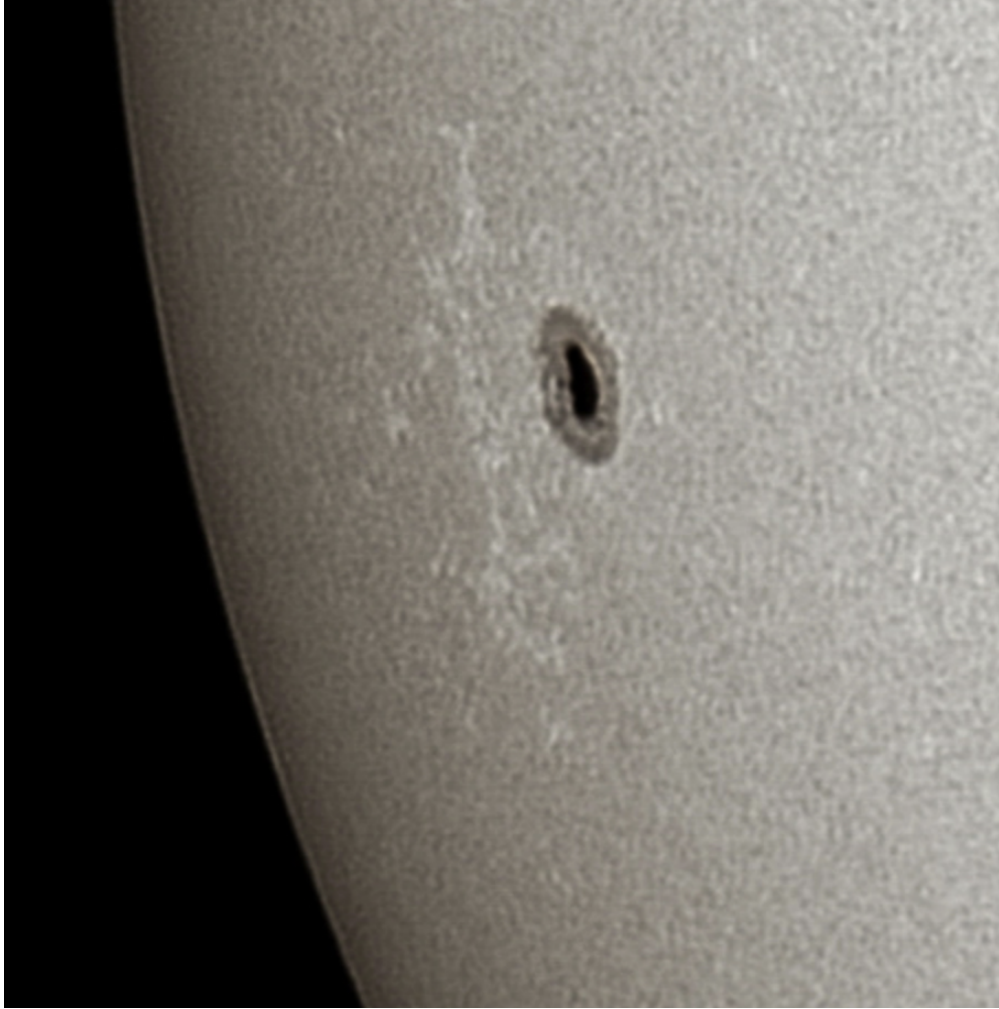
Figure 1.3: Image of an active region from SDO in 2019 in white light showing active region 2741. The darker sections show the sunspot portion of the active region, with the smaller, brighter parts to the left of the sunspot indicating the faculae, which is hotter than the Sun's photosphere. In this case, the active region is an individual sunspot with the faculae region following. Courtesy of NASA/SDO and the AIA, EVE, and HMI science teams.

2017-04-03T14:28:17
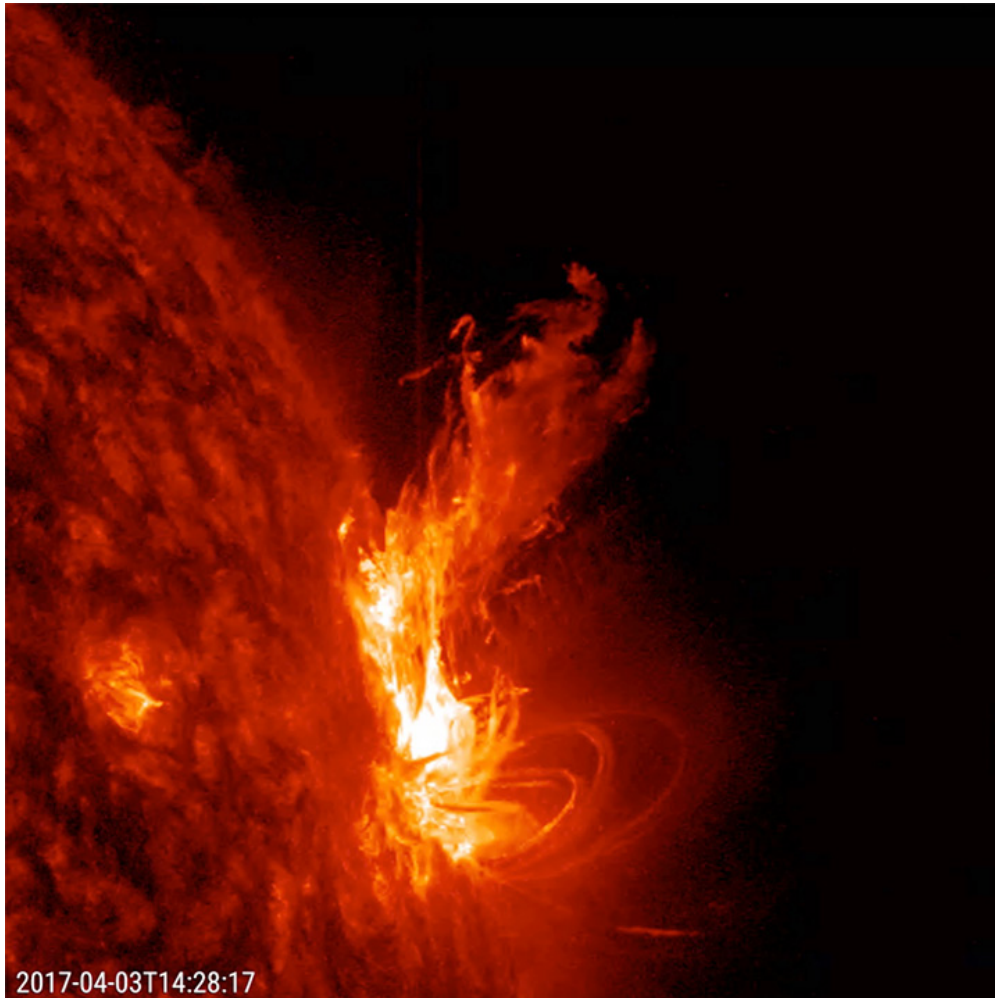
Figure 1.4: Image of an active region from SDO in 2017 in the UV region of light that shows prominences (the streams of plasma that reconnect back to the Sun in the bottom right) and several medium sized flares (the outbursts of plasma that escape the Sun's gravity above the prominences). These prominences and flares are clearly connected to the active region below them, and they are showing up very clearly in the UV because they are higher energy than the Sun's surface. Another smaller active region can also be seen in the bottom left of the image. Courtesy of NASA/SDO and the AIA, EVE, and HMI science teams.

The Transit Light Source Effect

Pre-transit Stellar Disk is the **Assumed Light Source**

Actual Light Source is the Chord Defined by the Planet's Projection

Spectral Difference due to Different Spot/Faculae Contributions Contaminates Transit Spectrum

Observed Transit Spectrum
True Planetary Spectrum
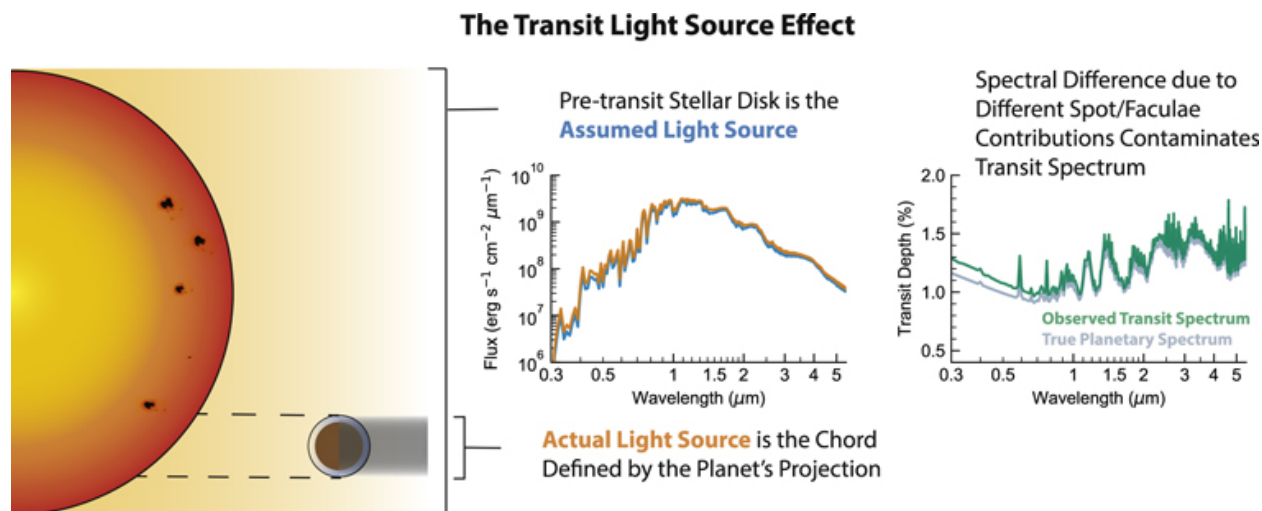
Figure 1.5: The transit light source effect is shown here as a schematic, taken from [1]. The figure shows a schematic of a star with dark spots both in the path of the planet on the bottom and out of the path of the planet on top. The figure of the two plots to the right of the schematic shows the stellar spectrum (flux versus wavelength) for the assumed star that is unspotted (blue) versus the actual light source which has many spots (orange), and they are noticeably different. The second figure shows the difference to the transit planetary spectrum (this is plotted as transit depth as a percentage versus wavelength) because of the spots with the observed spectrum shown in green and the true spectrum shown in gray. Again, in this figure, there is a clear difference between the observed spectrum and the true planetary spectrum once it has been corrected for stellar activity contamination.

in the field of exoplanet transmission spectroscopy [1]. When an exoplanet transits in front of its host star, the light coming from the star passes through the exoplanet's atmosphere (if it has one), and if spectroscopy is performed for the duration of the transit, the exoplanet's atmospheric spectrum can be disentangled from its host star's spectrum (e.g. the transit light source effect, see Figure 1.5) [1]. However, if the star itself has stellar surface features like spots, those will contaminate the exoplanet's spectrum. In fact, even spot covering fractions of 1% will contaminate the resulting spectrum more than any other potential uncertainties in the observations [27]. Thus, as transmission spectroscopy becomes increasingly more important with JWST, it is becoming even more vital to characterize the starspot properties of many stars using multiple techniques.

1.2.1 Spectroscopic Methods

The most common methods of studying the spot properties of stars are all spectroscopic methods. Each method is slightly different, but they all employ some form of spectroscopic

measurements. Two of the most powerful methods for mapping the spot distribution of active stars is Doppler imaging and Zeeman-Doppler imaging. Doppler imaging involves using the spectral line profiles as a map of the stellar surface, though this technique is reserved for only rapidly rotating stars [28]. As the star rapidly rotates, there will rotational broadening of the line profiles, and if a cool spot is present on the surface, a bump will appear in the line profile as it rotates into and out of view, see Figure 1.6 [2]. By studying changes in the bump in the line profile over time, a map of the stellar surface can be produced. Doppler imaging by nature relies heavily on the stellar atmosphere models, the stellar parameters, and the atomic line lists that are used. Since these parameters must be assumed, a wrong estimate of the temperature of the photosphere will impact the resulting spot distribution [2]. Additionally, Doppler imaging has trouble when the star rotates near equator-on because the spots will create symmetric Doppler shifts in the line profiles [29]. Zeeman-Doppler imaging is similar to Doppler except it uses spectropolarimetric data, which allows for the disentanglement of different magnetic field distributions by using the Zeeman-splitting of line profiles [30]. Typically the Zeeman signatures caused by starspots would be too small to be observed given the current instrumentation, but if multiple lines are combined together to increase the signal-to-noise, it can be done [31]. Given the additional polarmetric data obtained with Zeeman-Doppler imaging, more detailed mapping of the magnetic field can be done, which means the different components of the magnetic field like the radial and azimuthal fields. While this technique can be very powerful, these measurements require very precise spectropolarimetric observations, and again depend on the assumed stellar photospheric temperature and line profiles [2].

The other main spectroscopic techniques involve using the molecular bands present in the spectra of active stars. Specifically, certain molecular lines can only be formed in cooler temperatures, like in spots for G and K type stars, but these cooler temperature lines form in the photospheres of M type stars. TiO lines are the most commonly used molecular bands as they produce the strongest features [32]. This technique combines the spectra of a standard star of one temperature for the photosphere and one for the spot with a spot covering fraction weight applied [32]. The spot covering fraction is simply the fraction (or percent) of the surface of the star that is covered in spots. It is important to note that the spot covering fraction is variable, and there is a degeneracy between the spot covering fraction and spot temperature (i.e. cooler spots will produce lower spot covering fractions and vice versa). Once the correct covering fraction and spot temperature has been found, then the resulting model spectrum of the star will match the observed spectrum. This is then done multiple times over the course of one stellar rotation in order to create a spot distribution map for that time period. This technique is great at determining an estimate of the overall covering
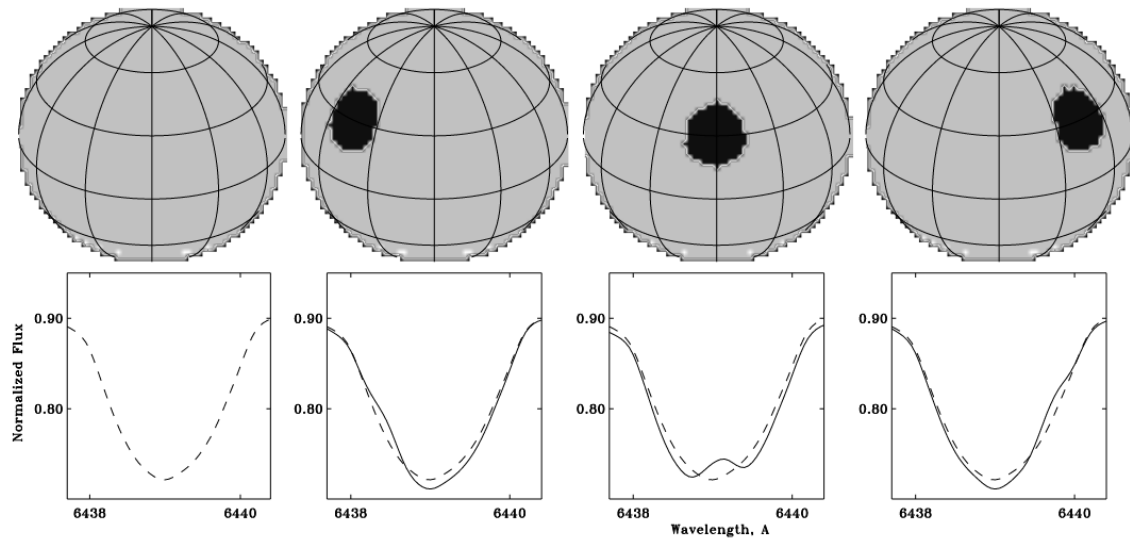
Figure 1.6: Doppler imaging as a starspot measuring technique shown for a fictional fast rotating star with one large starspot, taken from [2]. The schematic shows the star with one large starspot (radius 20% the radius of the star) as a sphere on top at four different points in the star's rotation. Below the star itself is one example corresponding line profile for a Calcium I line (normalized flux versus wavelength) for a star with no spots (dashed line) versus the star shown above it with one large starspot (solid line). The solid line shows a clear bump in the third panel, when the spot is at the center of the star, with smaller bumps in panels two and four as the spot moves in and out of view.

fraction of a star, but because these temperature sensitive lines only appear at low enough temperatures, this method is sensitive to the umbra of the spot [2]. Additionally, once the effective temperature of the star is low enough to start producing these molecules in the photosphere, this method is no longer as ideal because it becomes very difficult to disentangle the spot versus photosphere [18]. A variant of this technique involves using a comparison between the line depth between a temperature sensitive line compared to an insensitive one. The line depth ratio will then change depending on the temperature of the spots and the spot covering fraction [33]. However, the temperature of the spots and the spot area are closely entwined parameters no matter the technique, so a measured spot covering fraction is dependent on the spot temperature or vice versa. In order to break this degeneracy, another independent measurement is needed, such as simultaneous photometry [34].

1.2.2 Photometric Methods

There are photometric techniques that can model the stellar variations caused by spots on the surface of the star. Since starspots are darker than the rest of the photosphere of the star when an image is taken of the star with spots on the surface, the overall flux of the star will be less than when there are no spots on the surface [20]. Thus, starspots create large amplitude variations in the flux of stars over time, and these starspot modulations can be seen in long term photometric data of stars. Typically, the modulation created by the spot themselves is semi-periodic and appears sinusoidal in nature. These techniques all involve using the light curve of an object or system, i.e. the normalized flux of the star over time. An example of spot modulation in a light curve in Figure 1.7 for the M dwarf star AU Mic [3]. It can be very difficult to measure the amplitude of the starspot modulations as the precision of the data plays an important role. One such method of this light curve modeling is by simple trial and error, where a number of spots of a pre-defined shape are placed on the surface of the star and the resulting light curve is modeled (see [35] and references therein). This type of technique is numerical in nature, and it requires many free parameters. Also, while the modeled light curve may match the data well, the solution is not unique as different spot distributions than the one assumed could also fit the data just as well. Rather than assuming the spot distribution, another photometric technique called light curve inversion was developed. This method assumes that the intensity coming from the star contains contributions from both the lower temperature spots and the hotter photosphere with the weight of each being determined by the spot covering fraction. Then, if you measure the flux of the star over an entire rotation period, the inverted light curve can produce a distribution of the spot covering fraction [2] over one rotation of the star. In this case, the distribution of the spot covering fraction produced gives only a sense of the large scale spot structure,
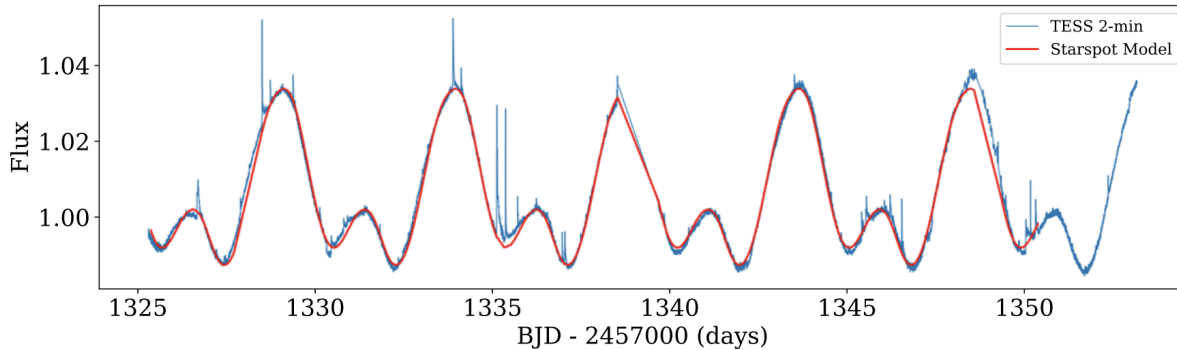
Figure 1.7: TESS 2 minutes data for AU Mic (blue) with starspot modulation and flares (large spikes in data). The best fit starspot model with two stationary spots is shown in red. This figure is reproduced from [3].

and it is dependent on the assumed spot temperature. Both of these photometric techniques once again only provide information on the general sense of the covering fraction for stars, and given that spot distributions can change on quick time scales, there is no guarantee that modeled spot covering fractions are the same for any later observations of the star. Figure 1.7 also shows an example of a starspot model created using a photometric technique.

1.3 STarSPot: Strengths and Limitations

1.3.1 Unique Photometric Method

Unlike other techniques for measuring the properties of starspots, STarSPot (`STSP`) uses a novel photometric method involving the primary transit of a secondary object [4]. When a planet or other companion transits in front of a star, a portion of the flux received from the star is blocked. The amount of flux blocked by the companion is directly related to the radius of the object, and this technique has been used since 1999 to detect and characterize exoplanets [36]. However, if the star has dark or bright spots on its surface, there is the possibility a transiting companion will cross one during a transit (see Figure 1.8). When one of these starspot crossing events occurs, the planet crosses in front of less flux because spots are darker than the rest of the star's photosphere, and this creates a sudden decrease in the observed transit depth, i.e. a bump appears in the transit when crossing a dark spot (see Figure 1.9) [37, 4, 38]. In the same way, if a companion crosses in front of a bright spot (i.e. a facula), a sudden increase in the transit depth, or a dip, occurs [38]. From these in transit depth changes, three measurements can be made: (1) the amplitude of the bump or dip; (2) the width of the bump or dip; and (3) the timing of the bump or dip. These three

measurements are inherent in the input data file for STSP, but STSP also requires information about the orbit of the companion in order to correctly determine where the planet is in its orbit compared to the star [4]. The orbital information is usually determined from modeling any unspotted transits of the object; though if there are no unspotted transits, more rigorous modeling is required. Lastly, STSP also requires information about certain stellar properties including the rotational period of the star and the inclination of the star's spin axis. Then, STSP can take all of this knowledge and use the companion as a knife-edge probe of the stellar surface itself [4].

1.3.2   How the Code Works

STSP is an entirely C based code that consists of two main parts: (1) a light curve generating engine and (2) an affine-invariant Markov Chain Monte Carlo (MCMC) optimizer (similar to [39]). The light curve generating engine is where the main calculations take place. The precise information about the companion's position in its orbit along with the star's properties allow for specific information about the location of the spots with respect to the path of the companion. The way this is calculated is that circular spots are projected on the spherical surface of the star and fixed in one location [4]. At every time step in the input light curve, the flux coming from the star is modified by the spots and the transiting planet according to the area of the spot (i.e. the radius), the contrast of the spot (i.e. how dark the spot is compared to the photosphere), the crossing of the planet and the star, and crossing of each spot and the star. The center of the light curve generating engine is the mathematical calculation for the intersections between the planet and star and the spots and the star. These are calculated for every time step and for every spot, but they have analytic solutions since the spots are defined to be circular [4].

The light curve generating engine is then wrapped by an affine-invariant MCMC which actually solves for the best fit set of spot properties for the input number of spots (N_s). STSP is designed to model three spot properties: (1) the latitude (θ_i); (2) the longitude (ϕ_i); and (3) the radius (r_i) for each spot. This type of optimizer allows the user to have many "walkers" (or chains) with different initial guesses for the spot properties that move through the parameter space towards the minimum χ^2 for a given number of steps. The best fit solution is then determined when all of the walkers converge on one minimum χ^2 solution [39]. As the spot latitude and longitude are not independent parameters, the coordinates for the next guess (or step) for the walker are determined from the current θ_i and ϕ_i. The distance that is moved away from the current position is determined randomly but is constrained by a scaling factor, a, which is a tunable input parameter. Thus, a moderates the step size, so a smaller a value results in steps that are closer to the current spot properties.
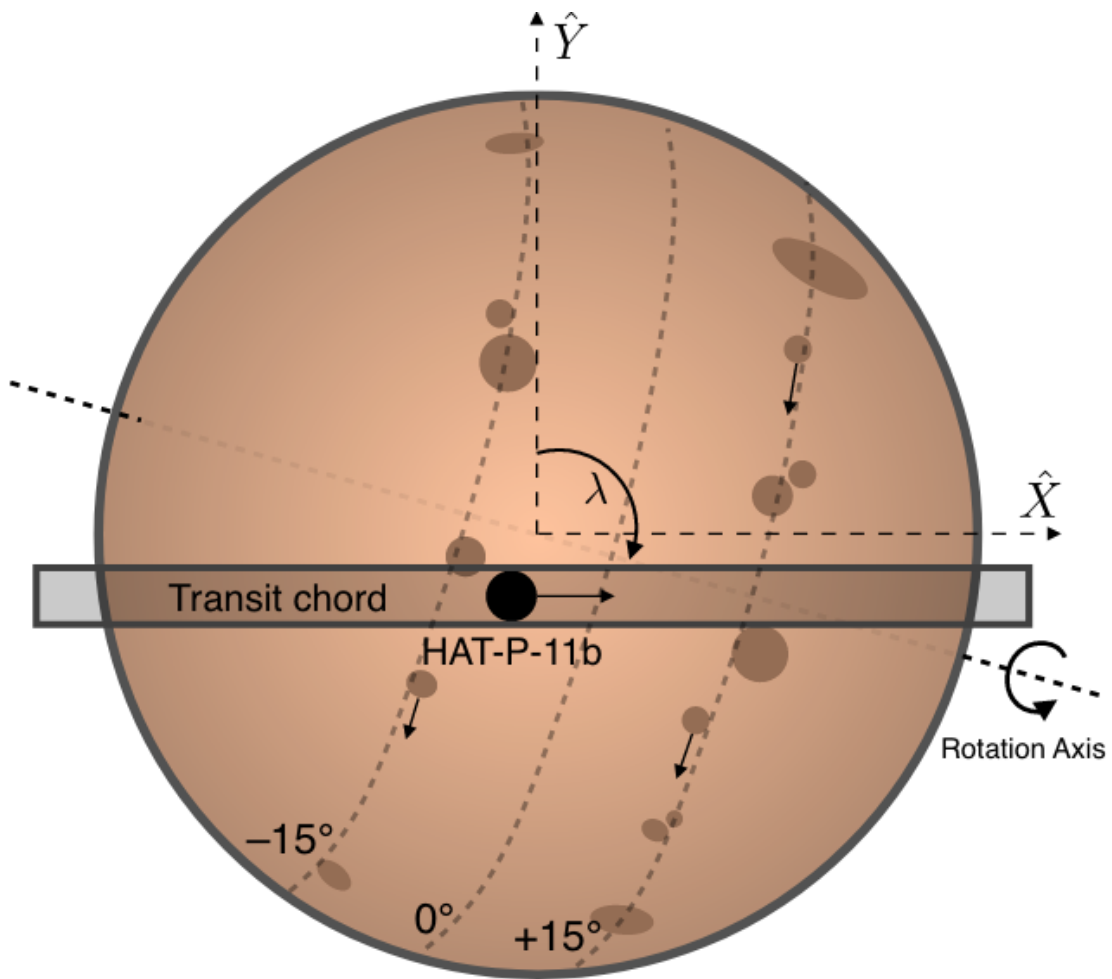
Figure 1.8: Schematic of HAT-P-11 star and planet system with spots and transit chord shown, taken from [4]. The HAT-P-11 star and planet are misaligned such that the star's rotation axis (dashed line through the star's poles) is not perpendicular to the planet's transit chord (e.g. $\lambda \neq 0°$) [5]. STSP then was used to measure this star's spot sizes and positions as the planet crosses in front of the spots, like in this schematic.

STSP can then produce a precise location and size for each spot in a given transit after the MCMC has reached the global minimum χ^2. Given that STSP is a light curve generating engine wrapped in an MCMC, it also produces a model light curve for the best fit spot parameters [4]. This model light curves can then be compared directly to the data and studied by eye to determine if the current best fit model has enough detail to match the data well. The bump structures within transits can be very complex, and that level of complexity can be hard to match with the model if we only consider the statistics [38]. Additionally, by comparing the STSP model and data directly, it is much easier to determine if the number of spots that was assumed at the start was the correct number of spots needed. Lastly, since STSP does have an optimizer built in, uncertainties can be calculated for all of the spot properties, and these are important due to the many degeneracies involved [4].

1.3.3   Limitations of STSP

While STSP is unique in its method, it does have limitations as all methods do. There are a few assumptions that must be made in order to be able to calculate the intersection points, namely the spots must be circular and they are assumed to be only one temperature. These assumptions are unlikely to be physically true as sunspots are asymmetric and have two distinct temperatures [23], but they must be made in order to do the analytic calculations. Another assumption that must be made in order to solve the problem is the contrast of the spot. Since there are only three measurements (see Section 1.3.1) but four properties (spot contrast, spot size and two spot position parameters) to measure, one property must be assumed. The easiest one to assume is the contrast. Additionally, there are a number of degeneracies inherent to the problem even after these assumptions [4]. The first major degeneracy is between the contrast of the spot and the size of the spot. If the contrast of the spot is changed to a darker spot, the spots themselves would need to change in size and latitude in order to create the same bump height [4]. The other degeneracy is between the spot latitude and spot radius. As the center of the spot moves closer to the center of the path of the companion, the bump height grows because the companion is covering more of the darker section and thus less light is seen by the observer [4]. Thus, if the spot is large in radius and directly in the center of the companion, the bump height would also be large, as shown in Figure 1.9. Since these two parameters are so closely entwined, it can be difficult to finesse the exact right combination to match the data. However, with enough steps and close monitoring of the model light curves, STSP can manage to combat this issue while in the path of the companion. That leads to the final limitation of STSP, which is it is most sensitive to the portion of the star that is traversed by the companion [38]. STSP is not technically limited to only in transit data, so it can model full out of transit light curves with observed spot

modulation. However, given the degeneracy between the spot radius and latitude, it is more difficult to achieve physically realistic and/or complex results without the latitude constraint that is provided by a transit crossing. Again, STSP can model these types of light curves successfully (see [3]), but it is more likely to provide a general sense of the total spotted area of the star rather than detailed information about the spot properties of a star.

There are other codes that are similar to STSP in that they also model stellar surfaces using photometry. Cheetah is a starspot modeling code that was designed to test the effects of various spot parameters as well as differential rotation on Kepler light curves [40]. Cheetah was only designed to simulate the full out of transit light curves, such that there are no additional constraints for the system like in transit spot crossing events [40]. Thus, it is different from STSP as STSP is designed to model both the in transit spot features as well as the out-of-transit light curves. Another similar starspot modeling code uses Bayesian inference and an adaptive parallel tempering algorithm to model the spot properties, their contrast, and their emergence and decay rates using a star's full out-of-transit light curve [41]. Lastly, starry is another starspot modeling code that uses spherical harmonics to model the brightness of the star's surface as one smooth continuous function [42]. On its own, starry does not model starspot properties like their size or location, but it can be wrapped in another optimization tool (e.g. pymc3 [43]) to produce starspot properties including their sizes, locations, and contrasts. This code has been used to model starspots (see [?] as an example), but it is important to note that because starry uses spherical harmonics, there will be a minimum size for any spot that is modeled based on the degree of the spherical harmonic used [42]. For all of these codes, another important thing to note is that it is unclear if these codes treat the longitude and latitude of spots as independent parameters in their optimization procedures. For spots, their latitude and longitude are not independent parameters, and so they must be dependent on each other in any optimization procedure that fits for those properties. For a code like starry, this could be controlled since the code itself is being wrapped in an optimization procedure that is chosen and defined by the user.

1.4 Previous STSP Results

To date, STSP has only been used on a handful of systems as the program is powerful but does require large amounts of computing time and finesse to get the best results [4, 3, 38, 44]. Most of the systems that have been modeled with STSP are objects with space-based photometric data. Using space-based photometry is ideal for STSP as high-precision, high-cadence data is necessary to get the most detailed model of the stellar surface. Additionally, space-based data allows for less observing constraints, so the highest number of transits can be observed
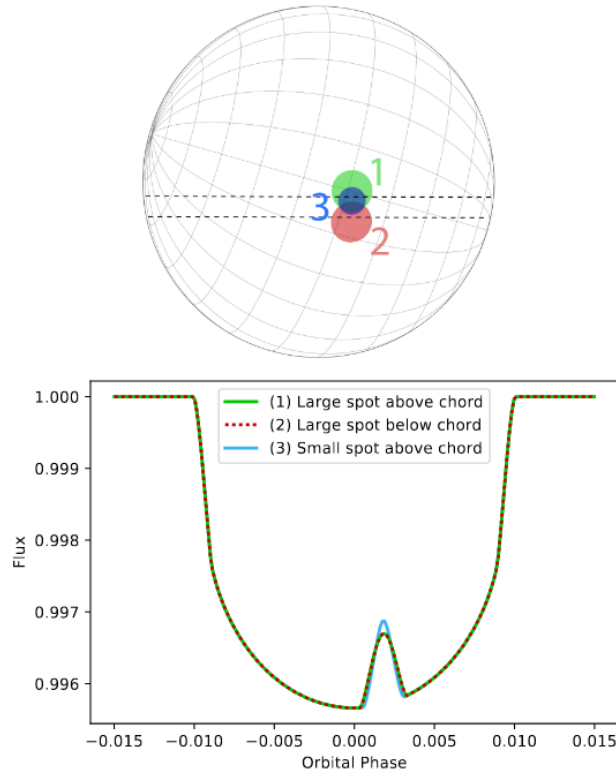
Figure 1.9: This figure shows three theoretical spots on HAT-P-11's surface in the top panel with the corresponding in-transit bumps shown in the light curve below the star. The top plot specifically shows three different size spots (in green, blue, and red) with different positions with respect to the transit chord (shown by dashed lines). The bottom plot shows relative flux versus orbital phase for each of the three theoretical spot models made with STSP with each line being the same color as its corresponding spot. This figure shows both how the STSP method works (see Section 1.3.1), and the degeneracy between spot size and position in the transit chord (latitude usually). In this case, all three theoretical spots produce very similar bumps in the model light curves because a smaller spot directly in the transit chord produces a similar amplitude bump to a larger spot that is slightly above or below the transit chord (see Section 1.3.3).

for each system. Here I will mention one example before moving onto the systems I analyzed and modeled with STSP.

1.4.1 HAT-P-11

HAT-P-11 is a K4 dwarf (T_{eff} = 4770 K) with a known rotation period of 29.2 days that hosts one known transiting planet [45, 5]. HAT-P-11b is a Neptune sized planet with P_{orb} = 4.88 days, R = 0.4 R_J, and M = 0.08 M_J. [46] used the Rossiter-McLaughlin effect to measure the angle between the rotation axis of the star and the orbital plane of the planet, and these measurements revealed that the planet orbits from pole-to-pole (i.e. λ = 106+26//−10°). This means that the planet will cross many latitudes during one transit but stay over approximately the same stellar longitude. There are 205 transits in the short cadence *Kepler* dataset with only 10 of those transits showing no signs of starspots in the transit chord [4]. [4] modeled all of the spotted transits using STSP with an assumed spot contrast that is a combination of sunspot umbral and penumbral average contrasts. Sunspots have complex structures with a smaller, darker umbral region and larger, less dark penumbral region, and if you combine the two with the correct area for each region, a contrast (c) of 0.3 is calculated. For HAT-P-11, [4] found that 95% of the spots could be modeled with this contrast with the other 5% needing a range of higher contrasts (i.e. darker spots). As the majority of spots only required the average sunspot contrast values, $c = 0.3$ was adopted for the STSP modeling.

[4] found that most of the spots on HAT-P-11 are similar in radius to Solar maximum sunspots, but with some spots having radii up to 30% the radius of the star. Due to the circular nature of spots within STSP, these larger spots are more likely to be asymmetric spot complexes that consist of many smaller spots very close together. HAT-P-11 itself has a radius that is about 70% the radius of the Sun, so the physical size of its spots are again very similar to Solar maximum sunspots. Spots on HAT-P-11 were also found at two active latitudes near ±15°, which is a similar structure to the Sun [4]. While there are many *Kepler* transits, the longitude coverage for HAT-P-11 is unfortunately not as complete as the latitude coverage because the planet orbits misaligned and with a nearly 6:1 resonance between the rotaional period and orbital period. Therefore, HAT-P-11b only covers about 6 longitude regions, so [4] found no conclusive results about longitudinal spot coverage patterns. While the spot radii for HAT-P-11 are similar to sunspots, the total area of spot coverage (also called the spot covering fraction) is 10-100x higher for HAT-P-11 due in part to the larger number of spots compared to the Sun [4]. With STSP, the in transit modeling is only sensitive to the transit chord (or path of the companion), which usually means we can only see one latitude band on the star without any knowledge of the rest of the star's surface. However,

since HAT-P-11 orbits across many latitudes in one transit and spot coverage should be symmetric across the star's surface longitudinally, each transit should sample an unbiased slice of the star's stellar surface. Thus, [4] conclude that the surface of HAT-P-11 has a total spotted area of $3^{+6}_{-1}\%$, which is much larger than the maximum sunspot covering fractions of 0.6% [47]. [4] conclude from their detailed STSP modeling of the high-precision *Kepler* transits of HAT-P-11b that a K4 dwarf star has a very similar dynamo to the Sun due to the similar contrasts, sizes, and active latitudes.

1.4.2 Thesis Outline

The rest of my dissertation will be structured as follows. Chapter 2, Modeling Surface Features on a Subgiant Star, will introduce and provide the results of using STSP to model the stellar surface features of s subgiant star with an M-dwarf companion using its *Kepler* high-precision data. This was published in a paper in the Astronomical Journal in 2022. Chapter 3, Measuring the Temperature of Starspots from Multi-filter Photometry, will introduce and show the results of using multi-filter, high-precision, ground-based data to measure the temperature of starspots that have been modeling using STSP. This paper was recently accepted to the American Astronomical Society's (AAS) journals in June 2023 and is currently under final edits. Chapter 4, Modeling Surface Features on an M dwarf, introduces and provides the results for an M dwarf with a gas giant planet that has a persistent starspot feature in every transit, which I modeled using high-precision ground-based data. This chapter was recently published in the Astronomical Journal in June 2023. The final chapter will address future work endeavors relating to modeling stellar surface features.

Chapter 2

Modeling Surface Features on a Subgiant Star

Reproduced from my first author paper published in the Astronomical Journal (volume 164, issue 1) in 2022.[1]

2.1 Introduction

Sunspots, the locations of where magnetic fields tangle and erupt to the surface of the Sun, have been observed and studied since the late 19th century. They are known to form in groups and have a non-uniform temperature with a darker cooler umbra surrounded by a slightly warmer, brighter penumbra. Sunspot groups are complex in nature, and their size and overall complexity play a significant role in the underlying magnetic activity level [24]. The overall sizes of sunspot groups vary on the eleven year solar cycle with groups range in radius from ~ 0.3 % of the Sun during a typical Solar minimum period and on average ~ 7 % during a typical solar maximum period with the largest sunspot on record having a radius of 11% the radius of the Sun [10]. Sunspots also grow and decay over time, though for individual spots the decay rate appears to be constant no matter the area of the spot. The number of sunspots in each group increases as the area of the group gets larger, meaning there are more likely to be many small spots within a group rather than one large spot [25].

Detailed studies of starspots, the stellar equivalent of sunspots, are key to understanding the magnetic activity on the surface of stars. These studies expose key underlying magnetic features which can provide valuable constraints on stellar dynamos [48]. Stellar activity that is similar to the Sun can be seen on M-dwarfs, including a subset of active M-dwarfs that exhibit significantly more activity and more energetic flares than seen on the Sun (see e.g. [48]). Stellar activity on other spectral types can be found as well through studying the brightness fluctuations of the stars over time [49]. For solar type stars, there is also a distinct connection between the rotation period of a star and the magnetic activity level, with faster rotating late-type stars exhibiting stronger activity [50]. Thus, a late-type star with a fast rotational period will be much more active than a slowly rotating star of a similar temperature. Furthermore, giant stars in short-period binary systems, e.g. RS CVn systems, can also be much more active than their younger, main sequence counterparts [14].

Analyses of the spotted areas of stars is also key to studying planet atmospheres using transmission spectroscopy as stellar activity is a major source of contamination for these

---

[1]https://ui.adsabs.harvard.edu/abs/2022AJ....164...14S/abstract

observations [51]. When considering the effect of spots on the surfaces of stars in transmission spectroscopy, the overall fraction of the star that is covered in spots is a key parameter, and [27] showed that for even a total spotted area of 1%, starspots would be the dominant source of uncertainty for a transmission spectrum of an exoplanet. [1] also showed that spot and faculae covering fractions for M-dwarfs generally underestimate the stellar contamination, and with realistic stellar contamination levels, the resulting transit depth effects can be up to 10 times that of planetary atmospheric features. This has been shown with the M dwarf K2-18 where [52] found that stellar surface brightness variations could explain the inferred detection of a water absorption feature on its sub-Neptune habitable zone planet's atmosphere found by [53].

With some active stars having spotted areas of up to 40% [13], the characterization of the activity on all stars is imperative to correctly understanding the transmission spectra of exoplanets around all stars. At the high levels of spectrophotometric precision that missions like JWST and ARIEL will provide, this is now a critical effect to understand and mitigate [51]. The Pandora SmallSat mission will also allow for simultaneous visible time-series photometry and near-IR spectroscopy of exoplanet targets to understand and mitigate the effect of stellar activity on exoplanet atmospheres [54].

There are many different techniques that have been developed to study starspots including Doppler imaging [55], observations of molecular lines [32], spectropolarimetry [31], and long-term photometric observations [4]. Each individual technique is important because each one tells us about various aspects of starspots such as their temperature from molecular line observations, differential rotation with Doppler imaging, and stellar activity evolution from photometric observations [48]. Additionally, high precision transit photometry can allow one to spatially resolve starspots, using the transit (whether planetary or stellar) as a knife-edge probe of the star. While the transit is occurring, the overall flux of the host star is reduced. If the companion crosses in front of a spot (or a plage), there will be a signature positive (or negative) bump during the in-transit part of the light curve. Both spectroscopy and transit photometry provide insight into the overall spotted area of a star, i.e. the filling or covering factor. Spectroscopic observations probe the net amount of spatially unresolved spots, whereas transit photometry can spatially resolve spots along the transit chord blocked by the companion during transit.

[56] were the first to use this novel technique to map a starspot on the surface of CoRoT-2 were the spot was occulted during a planetary transit. [4] and [57] then applied this novel photometric technique to *Kepler* satellite data of the K-dwarf star, HAT-P-11, and the young solar analogue, Kepler-63, respectively. HAT-P-11 has a similar rotation period to the Sun at $\sim$ 29 days, but as it is a cooler star, it has a deeper convection zone which could lead to

20

higher levels of activity than seen in the Sun [4]. The deeper convection zone of cooler stars leads to more turbulence in the star and thus more activity [48]. [57] found that Kepler-63 has two bands of spots in its Northern hemisphere with larger spots closer to the equator and pole. Kepler-63's fast rotation rate ($\sim$ 5.4 day period) could explain why it has larger spots near the equator and pole of the star [57]. Both [4] and [57] were able to study distribution of spot latitudes and the change in the spot latitudes over time because both planets have nearly polar orbits. [57] found little evidence of differential rotational in Kepler-63, indicating that it rotates almost as a solid body.

We identify KOI-340 (KIC 10616571, TIC 273376221, 2MASS J19503952+4748050) as an eclipsing binary system consisting of a G subgaint primary and an M dwarf companion that exhibits in-transit starspot crossing features in the original long cadence *Kepler* data. Figure 2.1 shows all 38 normalized transits of KOI-340 overplotted by the model generated from the DR25 data release [6]. The residuals compared to that model plotted in Figure 2.1. These residuals exhibit a significant increase in in-transit scatter compared to the immediately adjacent out-of-transit data, which is the signature of variations in surface brightness (i.e. active regions) on the primary star being occulted by the secondary star during the transit.

In this paper, we model the *Kepler* long cadence light curves of KOI-340 to characterize the starspots on the primary star. In Section 3.2, we present updated physical and orbital parameters of the eclipsing system to determine the unspotted transit light curve. In Section 3.2.1, we describe the modeling of all *Kepler* transits showing in-transit starspot crossing features to derive the properties of the spots. In Section 3.4, we discuss the implications of the derived spot properties and put KOI-340 into the broader context of known objects with starspot measurements. Finally, in Section 3.5, we summarize the main conclusions of the paper.

2.2 Physical and Orbital Properties of KOI-340

KOI-340 is a highly eccentric eclipsing binary consisting of a G subgiant primary star with an M-dwarf companion in a 23.67 day orbit. [58] were the first to conclude that the system was a single-line spectroscopic binary based on two radial velocity (RV) measurements made at quadrature with the SOPHIE instrument. An additional 21 RV measurements obtained at eight different phases with the high resolution spectrograph, CAFE, on the 2.2-meter telescope at Calar Alto Observatory [59] were modeled along with the primary and secondary transits from *Kepler* [9] to derive the orbital parameters and determine this is a highly eccentric ($e = 0.513 \pm 0.005$) eclipsing system with a mass ratio, $q = 0.20 \pm 0.05$.

[60] present the spectroscopic stellar parameters, T_{eff}, $\log g$, $v \sin i$ and metallicity, for

KOI-340 as determined by fitting its stellar spectrum with synthetic spectra, and fit isochrones to obtain a mass and radius estimate for the primary star. Using these techniques, the authors find the following stellar parameters for the primary star: $T_{eff} = 5593\pm27$ K, $\log g = 3.96\pm0.05$, $[M/H] = 0.28\pm0.01$, $v\sin i = 6.9\pm0.5$ km s^{-1}, $M_\star = 1.21^{+0.04}_{-0.03}$ $M_\odot$, and $R_\star = 1.89$ $R_\odot$. Furthermore, [61] analyzed 10 months of *Kepler* data to measure the rotation period of 1570 objects. KOI-340 was included in this analysis, and [61] found a rotational period for KOI-340 of 12.942 ± 0.018 days.

The transit model presented in the DR25 *Kepler* data release and shown as the black line in Figure 2.1 was derived from all the primary transits of KOI-340, most of which have starspot crossing features. This results in a default model with a depth that is shallower than what would have been derived from unspotted transits. However, accurate characterization of the starspots depends on an underlying transit model shape that reflects the non-spotted stellar surface flux with limb darkening. In addition, correct characterization of the longitude and latitude of the starspots on the surface depends on the most accurate orbital properties of the two-body system and knowledge of the stellar rotation period and tilt of the spin axis of the star. Therefore, we derive updated values for the physical and orbital properties of the KOI-340 system using only a subset of transits that show little or no in-transit spots, while also incorporating in the fit the 21 existing radial velocity measurements from [9] and all the secondary transits in the *Kepler* light curve to fully constrain the eccentric orbit.

The primary and secondary transits are normalized while preserving the transit depth in the presence of out-of-transit variability using the technique discussed in [4]. We normalize all primary and secondary transits using the following steps:

- Fitting and subtracting a second-order polynomial from the out-of-transit fluxes within 3 hours of each transit.

- Add the peak quarterly flux to each detrended transit (which approximates the unspotted brightness of the star)

- Divide the fluxes by that same peak value

This technique removes trends in flux due to stellar variability and normalizes the out-of-transit fluxes to near-unity, while maintaining a uniform transit depth over all transits.

We then apply a Markov-Chain Monte Carlo (MCMC) analysis simultaneously to the normalized light curves and radial velocity points following the method described in [62] and [63]. Our light curve model adopts the analytic formulae presented in [8] to describe the shape of the primary transit with limb darkening. As a single-lined eclipsing binary with a mass ratio, $q \sim 0.2$, we have chosen to use this well-tested code to characterize the precise shape of

the unspotted primary transit and directly measure the orbital parameters that describe the position of the secondary companion. These parameters include the orbital period P_{orbital}, the time of mid-primary transit T_0, the eccentricity e, the argument of periastron ω, the radial velocity semi-amplitude K_1, the centre-of-mass velocity of the system γ, and depth of the secondary transit (ΔF_{sec}). These parameters with their robust uncertainties are given in Table 2.1. While definitive masses and radii are beyond the scope of this paper, adopting a mass for the primary star from [60] as mentioned above allows for analytically calculating the amplitude of the secondary radial velocity curve, K_2, the mass ratio, q, and the orbital separation, $a \sin i$ by inverting the equations given in [64]. These values are also provided in Table 2.1. Finally, the shape of the primary transit is accurately described by the [8] model with a depth, $\delta = 0.020164 \pm 0.000096$, impact parameter, $b = 0.331 \pm 0.020$, and mean stellar density, $\rho_* = 0.208 \pm 0.018$ with theoretical four parameter limb darkening coefficients of $c_1 = 0.624, c_2 = -0.286, c_3 = 0.867, c_4 = -0.447$ which were determined using quasi-spherical PHOENIX model atmospheres [65]. The primary transit model and the secondary transit are shown in Figure 2.2. The radial velocity curve is shown in Figure 2.3.

Table 2.1: Ephemeris and orbital properties of KOI-340 system

	Value	Units
T_0	6200.95698 ± 0.00025^a	days
P_{orbit}	23.673113 ± 0.000011	days
e	0.493 ± 0.019	
ω	-122.0 ± 1.2	degrees
K_1	15.80 ± 0.40	$\mathrm{km\,s^{-1}}$
γ	-83.97 ± 0.02	$\mathrm{km\,s^{-1}}$
ΔF_{sec}	0.00088 ± 0.00016	
K_2	80.6 ± 1.0^b	$\mathrm{km\,s^{-1}}$
q	0.20 ± 0.05^b	
$a \sin i$	39.2 ± 0.5^b	$R_\odot$

[a] Barycentric Julian Date – 2 450 000
[b] Calculated assuming $M = 1.21 M_\odot$[60]

In addition to the orbital properties and shape of the transit, we measured the stellar rotation period and the tilt of the rotation axis out of the plane of the sky. The period is measured from all available quarters of long cadence *Kepler* light curves after eliminating the transits of the companion star. We run a Lomb-Scargle periodogram [66] over the entire *Kepler* data set with the primary transits removed from the data. The periodogram over all

of the quarters is plotted in Figure 2.4.

The Lomb-Scargle (LS) periodogram displays a maximum power at a period of 13.02 ± 0.97 days, which is consistent with the more robustly measured rotation period using the auto-correlation technique (12.942 ± 0.018 days) as found by [61]. If you instead run a periodogram on each individual *Kepler* quarter, a range of rotational periods is obtained with the average period of those individual periodograms being 12.93 days with a standard deviation of 0.28 days which is also in agreement with the period found by [61]. The relatively large range of measured rotation periods is likely due to real physical phenomena such as the stochastic emergence of spots at different phases and/or the differential rotation of the star leading to spots that emerge at different latitudes. [67] recently showed that multiple different peaks when examining the LS periodograms for each *Kepler* quarter of an object may be used to put possible constraints on the differential rotation of the object. However, they do assume that the spots on the surface of the object do not evolve within one quarter (~ 90 days), which may not be the case for KOI-340 (see Section 2.4.4 for more details). As such, we leave further exploration of the quarter-to-quarter LS periodogram differences to future work.

A comparison between the measured $v \sin i$ and the $v \sin i$ calculated from the rotation period and stellar radius can be used to constrain the tilt of the rotation axis of the star. The $v \sin i$ was measured by [60] to be 6.9 ± 0.5 km s^{-1}. Adopting the radius, $R_\star = 1.89 \pm 0.05$ R$_\odot$ determined from isochrone fitting in [60] and using the rotation period derived by [61], we calculate the $v \sin i$ to be 7.40 ± 0.03 km s^{-1}. This value is consistent with a tilt of $0°$ toward the observer and implies that the companion star will pass over approximately the same latitudes during every transit. Assuming the companion's orbit is aligned with the star's stellar rotation axis, i.e. $\lambda = 0°$, STSP calculates this latitude as $-19.3°$ based on the measured impact parameter of $b = 0.331$. In the absence of an obliquity measurement, we assume the M dwarf companion's orbit is aligned with the host star so we can determine the latitude and longitude of the active regions location on the surface of the primary star. As shown in Section 2.4.4, we do track spots over multiple orbits meaning the system is likely aligned.

2.3 Modeling Active Regions on KOI-340

We model the long cadence *Kepler* light curves of 38 primary transits of KOI-340 using the modeling program, STarSPot (STSP) [4] to characterize the surface starspot features around the latitude of $-19.3°$. STSP is a C based program that models the surface brightness variations (i.e. starspots) on the primary star's photosphere in a two-body gravitationally bound eclipsing or transiting system.

The parameters for the transit model derived above define the unspotted transit, but almost all of KOI-340's *Kepler* transits contain evidence of stellar surface activity features, namely starspots and plages. Using this model as a starting point, we employ STSP to derive simulated spotted light curves of the primary transit of KOI-340 by adding a fixed number of spots each with a fixed contrast to the surface of the star. The contrast of the active regions is decided by the ratio of the integrated flux for the active region over the integrated flux for the star's effective photosphere relative to a certain bandpass. We use a contrast equal to the average area-weighted contrast for sunspots ($c = 0.3$) for every spot and [4]. We are modeling *Kepler* light curves, so the contrast value we use is for the *Kepler* bandpass. Given the flux of the secondary is around 2 orders of magnitude less than the primary, the effects modeled here are coming from the primary star.

Using an affine-invariant Markov Chain Monte Carlo (MCMC) [39], STSP optimizes the transit model by sampling different radii (R_{spot}/R_*) and positions (latitude and longitude, θ and ϕ respectively) of each spot, ultimately adopting the model that produces the lowest χ^2. We perform an initial MCMC run for every transit by starting 300 chains with one or two spots placed in random initial conditions on the star and allowing the spot configuration to evolve for an initial fixed time of approximately 4000 steps with each chain evolving independently. Then, we choose the chain with the lowest χ^2 to be the best fit STSP model for that run. If the minimum χ^2 solution to this run matches the spot features in the transit with a reduced χ^2 less than 10, we consider this to be the final spot configuration for that transit. If the initial run appears to have the correct number of spots to match all the occultation features but not a sufficiently low reduced χ^2, we continue running the MCMC optimizer for more time, re-starting from the last accepted step for all chains, until it reaches the required minimum χ^2 (i.e. less than 10). We chose to consider our runs complete with a reduced χ^2 of less than 10 as after running the transits for over 40,000 steps the χ^2 values were not decreasing anymore and corresponded to a reduced χ^2 of less than 10.

As an example, consisder *Kepler* Transit 21 centered around time 610.4 Barycentric *Kepler* Julian Date (BKJD, i.e. BJD - 254833). This is the simplest spotted transit for the system, showing only one distinct spot feature during the transit. The initial MCMC optimization run found a single large spot (centered around 610.6 BKJD) almost entirely in the path of the secondary, as seen in Figure 2.5 (bottom). The model light curve shown in red (Figure 2.5, top) results in a reduced $\chi^2 = 4.5$ relative to the *Kepler* data. We decided this fit was sufficient and no attempts with additional spots were necessary. With a best fit $R_{spot}/R_* = 0.16 \pm 0.01$, this spot is $\sim 70\%$ larger than the largest ever sunspot (relative radius of 11% the radius of the Sun) [10].

Typically, the KOI-340 transits have more complex structures than shown with Transit

21. If the initial one- or two-spot run cannot match all the subtle features in the light curve, we add additional spots and apply the MCMC optimizer in 4000 step runs until the best fit STSP model matches the data well and has a reduced χ^2 less than 10. Depending on the complexity and number of spots, each transit typically takes 10 of these STSP runs to satisfy the convergence criterion, making the total steps taken approximately 40,000 steps.

Transit 19 is representative of most KOI-340 transits, with the final STSP modeling results shown in Figure 2.6. For this transit, we initially modeled it using initial conditions in STSP with two spots. However, we quickly found that two spots were not sufficient to fit the complex bump feature (centered around 563.00 BKJD) along with the bumps on ingress and egress (centered around 562.8 BKJD and 563.25 BKJD respectively). Once we increased the number of spots to four, we were able to fit the primary transit very well with a final reduced χ^2 value of 2.2. In this case, the shorter, wider bump (at time 563.0 BKJD) is best fit with two smaller spot groups that are located right next to each other rather than one large spot group. This is in comparison to the sharper, larger bump seen in Transit 21 which was fit very well with only one spot. As seen in Figure 2.6, all of the spot groups modeled with STSP for this transit are well within the path of the companion, and all four of the spots have radii from $R_{spot}/R_* = 0.07 - 0.10$ which are comparable to Solar maximum sunspots (see Section 2.4.2 for more details on typical sunspot sizes) [11].

One of the key features in many KOI-340 transits is spot groups on the ingress and egress of the transit as shown in Transit 19. However, spots on the ingress and egress can lead to very different final spot parameters depending on the duration of the feature. Transit 29 showcases this phenomenon as seen in Figure 2.7. For the spot on the ingress of Transit 29 (centered around 799.6 BKJD), it extends over five cadences (150 minutes total for *Kepler* long cadence data) and is very distinct from the no spot model. Thus, STSP finds the best fit spot to be both large in size and mostly in the path of the secondary ($R_{spot}/R_* = 0.234$). In comparison, the spot on the egress of the transit (centered around 800.0 BKJD) only lasts for three cadences (90 minutes) and is not as distinct from the no spot model in Figure 2.7 (cyan line) leading to a smaller spot that is fully in the path of the secondary ($R_{spot}/R_* = 0.115$). Both of these spots are distinct from the small bump in the middle of the light curve centered around time 799.8 BKJD. Finally, for the small bump in the middle of the transit, STSP finds the best fit to be a smaller spot ($R_{spot}/R_* = 0.089$) fully in the middle of the secondary crossing path as expected. As all of the spots are distinct from each other, it is much easier to determine that there are only three spots in this transit, in contrast to the complex spot structure centered around 563.0 BKJD in Transit 19 (see Figure 2.6). The smaller bump in the middle of the transit is also a good contrast to the sharper, taller bump seen in Transit 21 (centered around 610.4 BKJD, see Figure 2.5), which gave rise to a much

larger spot radius.

There is a known degeneracy between the central latitude and radius of a spot because at the precision and sampling of the *Kepler* data most features that can be fit by a small spot that is fully in the path of the transit chord can be equally well fit by a larger radius spot that is barely grazing the transit (see Figure 5 in [4]). To mitigate this problem, we manually select the best fit results that favor smaller, in-transit spots as opposed to grazing spots, and we provide error bars for the relative radius of the spot, which accounts for these near-equivalent solutions. The error bars are calculated from the MCMC output using the `corner.py` software which calculates the appropriate 2D Gaussian density rather than the regular 1D 1σ error bars [68].

2.4 Results and Discussion

We used `STSP` as described in Section 3.2.1 to model 36 tranists of KOI-340 that show evidence of spot occultations during a transit. Two of the 38 total transits show no signs of surface brightness variations and were not modeled with `STSP` with two additional transits showing very little sign of variation that were modeled using `STSP` giving a 89.4% probability of strong starspot crossing features during a primary transit for KOI-340.

The best fitting transit models for the 36 transits produce 122 total starspots in the path of the planet, each defined by its position on the surface of the star and its size relative to the stellar radius (latitude, longitude and R_{spot}/R_*). It is important to note that the spots identified on KOI-340 are likely to be starspot groups like the active regions on the Sun, rather than individual starspots, given their large sizes.

2.4.1 Spot longitudes and latitudes

In Figures 2.8 and 2.9, we plot the distribution of spot longitudes and latitudes, respectively. The longitude distribution reveals that there are spot groups occurring at every longitude, and spot occultations in nearly every transit, and thus there is no preferred longitude for spots detected at mid-latitudes in the path of the secondary. We also do not find any evidence of two preferred active longitudes that are 180° apart from each other as has been seen in multiple other types of active stars like RS CVn type stars [69], FK-Com type stars [70], young, active Solar analogues [71], and even in the Sun [72]. However, active longitude studies typically involve long term photometric observations which we do not have for KOI-340. In comparison, the histogram of latitudes of the spot groups (see Figure 2.9) illustrates a more defined distribution, as expected because modeling in-transit spots is only sensitive to the portion of the host star that is covered by the path of the transiting object. The center of the

transit path is shown in Figure 2.9 as a solid black line with the full extent of the transit path shown with dashed black lines. 24% (29 of the 122 total spots) of spots have their central latitude outside of the path of the planet (i.e. they don't fall in the dashed line region). We refer to these as grazing spots.

2.4.2 Spot Radii

We next compare our distribution of spot sizes for KOI-340 to a representative distribution of sunspots at Solar maximum and Solar minimum with the same baseline as the *Kepler* mission of 4 years (Figure 2.10). For the Solar maximum distribution, we used a subset of data from 1956-1960 shown in red, and for the Solar minimum distribution, we used a subset of data from 1962-1966 shown in blue [11]. These subsets were chosen because they are periods of time that are solely Solar maximum or minimum.

The distribution of KOI-340's spot size peaks with a value around 7.5% of the star's radius, which is similar to the peak of the Solar maximum distribution. These spots are the most common sized spots on KOI-340 as well as the Sun during Solar maximum. The smallest spot shown in Figure 2.6 during Transit 19 is an example of this typical spot. However, KOI-340 has many more larger spots than the Sun as evidenced by the tail of the distribution that extends out to a relative radius of $\sim 1/3$ the size of the star. KOI-340's median spot radius is $R_{spot}/R_* = 0.1144$ making half of the spots detected on KOI-340 larger than the largest ever sunspot (11% of the Sun, [10]). Despite the degeneracy between spot radius and latitude (described above), only 29 of the very largest spots in the 122 spot distribution are grazing spots that may appear artificially large. Discarding all spots with centers not in the path of the transiting companion, the distribution still extends out to $R_{spot}/R_* = 0.29$ which is 2.6 times the largest ever sunspot. This tail of larger spots could also be due to unresolved spot groups which causes the spot groups to appear larger.

2.4.3 Fractional Area

In addition to spot radii, we also calculate a lower limit on the fraction of the star that is covered by spots at the time of each transit. This quantity is important because it is immune to the spot-radius degeneracy, and it is necessary for transmission spectroscopy analyses when calculating the depth correction to the transit due to starspots. Indeed, [27] showed that for even a total spotted area of 1%, starspots would be the dominant source of uncertainty for a transmission spectrum of an extrasolar planet. [1] showed that for the very active M-dwarf TRAPPIST-1 system, with spot covering fractions around 8%, the resulting stellar contamination affects the transit depths 1-15 times more than planetary atmospheric

features. However, observations of the system have yet to produce evidence for significant transit contamination by dark starspots [73, 74, 75], while bright regions have been proposed to explain the rotational modulation of the host [76, 77].

We calculate the area of each circular spot that falls in the path of the companion and sum over all spots. We then divide the total spotted area in the transit chord by the total area of the hemisphere of the star $(2\pi R_*^2)$. This quantity represents the minimum fractional area of the stellar surface covered by spots because it assumes no other spots exist on the front face of the star. Figure 2.11, compares the lower limits derived for all transits of KOI-340 to the monthly average values for the Solar minimum (blue) and Solar maximum (red) distributions (as defined in above). We use the monthly average because the orbital period of KOI-340 ($\sim$ 23d) allows us to take a snapshot of the stellar surface approximately once a month over the 4-year duration of the *Kepler* survey.

KOI-340's fractional spotted area ranges from 0.4% to 5% of the stellar surface, and is almost always greater than the Sun's. All but one snapshot show a minimum spot covering fraction that is greater than the spot covering fractions over the whole Sun at any point during its cycle. The mean value for the minimum spot covering fraction on KOI-340 is 0.0198 Hemispheres (Hems), which is $\sim$10 times greater than the largest Solar fractional spotted area ever recorded [78] and large enough to create significant uncertainty in any transmission spectra of planets orbiting stars like KOI-340.

In Figure 2.12, we plot the longitude of every spot for a given transit versus the midpoint time of that transit. We have formatted the size of the marker to correspond to the radius of the spot group and colored the points according to relative spot radius. The green boxes surrounding each transit correspond to the total longitude coverage for each transit. In seven cases there are enough consecutive transits that we can combine every other transit in groups of three to create a complete 360 degree view of KOI-340 in longitude space (the transits centered around 400, 450, and 500 BKJD for example). By using these seven total instances, we can compute a lower limit for the fractional area of the entire star in the transit crossing region. In doing so, we get a range of fractional areas for the entire star in the transit crossing path to be 2.1-4.3%. If we assume that KOI-340 were to act similarly to the Sun, then we might expect KOI-340 to have a matching band in the Northern hemisphere of the star that is similarly active to the region of the transit crossing which would give a total fractional spotted area for the entire star of 4.2-8.6%. If we simply scale up the minimum total fractional spotted area for the entire star of 2.1% in the transit crossing path to be the same across the entire star, we get a value of $\sim$14% for an estimate of the total fractional spotted area of KOI-340.

2.4.4 Longitude Evolution

Figure 2.12 is also used to determine how the spots evolve over time. If two spot features are detected at similar longitudes in consecutive transits, this provides evidence that those features are caused by the same spot that has survived for more than the orbital period of the companion (23 days). Of the 122 total spots for KOI-340, there are 54 possible spots that could be seen in the next transit, and in 30 of those instances, a second spot feature is detected at a similar longitude in the following transit. Thus, there is a 55% probability that the spots persist to the consecutive transit meaning there is a 55% chance of the spots living longer than 23 days. In comparison, sunspots typically live for around a day but can live up to months depending on the size with larger sunspots lasting for longer amounts of time [23].

Furthermore, we use Figure 2.12 to estimate the differential rotation at a latitude of $-19.3°$ on KOI-340 by quantifying the progression in longitude of the 30 spots that are observed in consecutive transits. The majority of these spots progress forward in longitude, suggesting that the rotational motion of the latitude where the companion crosses is moving faster than the average rotation period defined by spots at all latitudes [37]. Estimating the differential rotation from the slope of the cyan line provided in Figure 2.12, we get a value of $\Delta\Omega \sim 0.004 \pm 0.001$ rad day^{-1} which is an order of magnitude lower than the Sun's differential rotation value of $\Delta\Omega = 0.055$ rad day^{-1} [48]. Presumably, the rotation period of KOI-340 measured from the periodogram is also generated by some of the same spots as we use here to infer the differential rotation implying the rotation rates should be similar between the two measurements. This is consistent with the small value we measure here for the differential rotation. Thus, this estimate is only a weak lower limit. Also, the long orbital period of 23 days for KOI-340's companion provide a sampling time that is not fine enough for a definitive measurement furthering our assumption this is a weak lower limit. With other stars like GJ 1243 in well-sampled *Kepler* data and with careful STSP modeling of the in-transit variability, there are signs of progression in longitude of the spots leading to an indication of differential rotation on the surface of GJ 1243 [37].

Finally, we also investigated if the radius of the spot changed at all from one transit to the next for the 30 spots that survive consecutive transits and found that the spots do not grow or shrink in any significant way. Unlike sunspots which decay more rapidly over time, the spots on KOI-340 appear to not change in size significantly if they survive for one complete orbital period (23 days).

2.4.5   Modeling of Plage

In one instance during a primary transit, we were able to model a bright stellar surface feature for KOI-340. During this transit, there was a dip significantly below the expected no-spot transit model as seen in Figure 2.13 at around time 373.7 BKJD which indicates the presence of a plage rather than a darker spot as seen in the other transits. We implemented a new feature in STSP to allow for two contrasts to be specified during a modeling run. For the contrast of the bright spot, we chose to use a value of 1.3, that is 30% brighter than the photosphere, as for the dark spots we used a value of c = 0.3 as described in [4]. The modeling of this transit was not unique in any other way, so our best fit model was still required to meet our convergence criteria mentioned in Section 3.2.1. The best fit solution for the plage is a feature with $R_{\text{spot}}/R_* = 0.10$. This plage seems to be closely followed by a larger, grazing spot, and it has been suggested that spots and plages are co-located on active G and K stars [79].

2.4.6   Out-of-transit Starspots

Given that the secondary companion crosses the primary at a latitude of $-19.3°$, the primary transit models that we have modeled and described in Section 3.2.1 only give us information about the surface features in the latitude range of $-27.8°$ to $-10.6°$ which encompasses the secondary's coverage on the host star. In order to study the surface features on the rest of the star, we model both the in- and out-of-transit light curve for one rotation period of KOI-340 centered on each primary transit. We model this entire light curve in STSP by fixing the previously determined in-transit spots and adding on additional spots until the brightness variations for the out-of-transit data are well modeled. As there is no constraint on the latitude of the added spots, the best fit spot positions and sizes from the out-of-transit variability provide degenerate results.

Thus, we choose all chains with χ^2 values within 20% of the global minimum χ^2 to be acceptable solutions. We then calculate the fractional spotted area of KOI-340 for all of the acceptable chains. Finally, we average the fractional spotted area across all acceptable chains to find the best fit fractional spotted area for one full rotation of KOI-340. For this procedure, we start with adding one additional spot and calculating the average fractional spotted area. However, the added spot needs to be large in size in order to match the variability seen in the out-of-transit data, so we repeat the same procedure adding additional spots until the fractional spotted area stops decreasing. Once the fractional spotted area appears to be constant even with an additional spot, we consider the out-of-transit modeling to be complete for that rotation.

Currently, we have modeled all of the full rotations of KOI-340 with STSP with the minimum number of additional spots needed to match the full out-of-transit light curve for that rotation. An example of this full light curve modeling with the in-transit spots held fixed and the minimum number of spots added is shown in Figure 2.14 with this full rotation of the star being centered around what we call Transit 21 (see 3.2.1). Using the total fractional spotted area of the entire star for each full light curve (of which there are 36), we can estimate the possible upper limits of the fractional spotted area for KOI-340. This is shown in Figure 2.15 where we have plotted the fractional spotted area versus the midpoint time of the transit (i.e. the center of the full light curve) with the green upper arrows indicating the minimum spotted area found using only the in-transit spots and the green points with approximate error bars showing the total fractional spotted area of the star using the full light curve with the minimum number of spots added. In Figure 2.15, the Sun's fractional spotted area is plotted as a solid red bar [11] along with HAT-P-11's range of possible fractional spotted area plotted as black dashed lines [4].

However, with adding only the minimum number of additional spots to the light curve, the best fit spots end up being large in size in order to fit the large out-of-transit variability as seen for example in Figure 2.14.

In order to determine a more accurate total fractional spotted area, we add additional spots and run STSP until we find a new best fit model. Then, we recalculate the fractional spotted area for KOI-340. In doing so, we can find the minimum fractional spotted area that still fits the full light curve which would then replace the current values shown as green points in Figure 2.15. We have done this successfully so far for the simplest primary transit (Transit 21) as the total number of spots needed to fit the full light curve ended up only being 8. The upper limit error bars attached to the green points represent the $\sim 10\%$ spread found when we add additional spots to the model for this transit. Figure 2.16 shows the total spotted area versus the total number of spots, and when you add additional spots, the total spotted area decreases and then levels out indicating that we are approaching the minimum total spotted area. With every additional spot that STSP needs to model the complexity of the problem increases by a factor of 3 so the modeling runs end up taking 24-48 hours on average to complete rather than 8 hours for the regular in-transit modeling. Since the STSP modeling runs take days to complete, we leave the completion of the other 35 full light curves to future work.

2.5   Conclusions: KOI-340 in larger context

KOI-340 is a G subgiant star with $T_{\text{eff}} = \sim 5600~K$, $M_\star = 1.21^{+0.04}_{-0.03}~M_\odot$, $R_\star = 1.89 \pm 0.05~R_\odot$ with a rotation period of 12.96 ± 0.97 days and an M-dwarf secondary ($M_\star = 0.214 \pm 0.006~M_\odot$). KOI-340 has a cool temperature for its radius, and while there is no direct mass measurement for this star, [60] estimates the mass from the temperature and radius to be around $1.2~M_\odot$ indicating that KOI-340 is likely in the process of evolving off the main sequence. KOI-340 also has a relatively slow rotation period for its estimated mass (~ 13 days compared to ~ 5 days for main sequence stars [80]) which could be due to angular momentum conservation as the star is getting larger. From the STSP modeling, we have determined that the radii of the in-transit spot groups can be much larger than typical Solar-maximum spots which might not be expected for a star of this mass and rotation rate.

In Figure 2.17, we have plotted a variety of stars with estimated fractional spotted areas derived from other methods using spectroscopic features [12, 13, 14], other stars that have been modeled with STSP [4], and the Sun [11] versus their Rossby number [81]. Their Rossby number was calculated using the equations in [16] which gives an empirical equation for a star's convective turnover time as a function of its color. The points and error bars are colored by their rotational period, and the square symbols denote stars whose filling factor was determined by spectroscopic methods while the circle symbol denotes stars whose fractional spotted area was found through photometric methods like STSP. Figure 2.17 shows that typically the lower the Rossby number the higher the fractional spotted area. This trend makes physical sense as a lower Rossby number indicates a system with fast rotation and/or larger convection zones, which are therefore more likely to be active systems. Therefore, the large spots on KOI-340 compared to the Sun could be due to its faster rotation and increasing convection zone depth as it evolves off the main sequence.

It is also important to note that for KOI-340 we have chosen to use the mean minimum fractional spotted area (2.1%; see Section 2.4.3) even though some of the individual transits can have much higher estimated fractional spotted areas assuming certain conditions. We have chosen to use this conservative lower limit as we are only sensitive to the transit crossing path using our in-transit STSP models though once we have fully investigated the out-of-transit variability for KOI-340 as well we will be more sensitive to the entire star's spotted area. If the entire star was spotted at a similar rate, that gives a value of 14% shown as the extent of the upper error bar for KOI-340. A more accurate measurement of the fractional spotted area will come from fully understanding the out-of-transit variability of KOI-340.

In summary, KOI-340 is an eclipsing binary system consisting of a G subgiant with an M dwarf companion that has starspots two times larger than the majority of sunspots on

average. We used data from the *Kepler* spacecraft to model both starspots and one plage using the starspot modeling program STSP which measures the position and radius of the surface features. We modeled 36 *Kepler* transits and found the minimum fractional spotted area of KOI-340 is 2^{+12}_{-2} % while the spotted area of the Sun is at most 0.2%. The starspots on KOI-340 were found to be present at every longitude with possible signs of differential rotation seen in the evolution of spots along with a 55% of spots longer than 23 days. Thus, KOI-340 is a G subgiant star with an M dwarf companion that has considerable stellar activity covering 2^{+12}_{-2}% of the primary star at a minimum. Future work includes fully understanding and modeling the out-of-transit variability of KOI-340 which will provide constraints on the total spot coverage of KOI-340.

2.6 Acknowledgements

Figure 2.1: Top: Normalized transit light curves of KOI-340 from the *Kepler* DR25 [6] data release are shown as a function of phase. The out-of-transit data is displayed in green, the ingress and egress is in red, and the measurements made when the companion is in-transit (between the second and third contact points) are in blue. The black line model is generated by using the DR25 parameters for KOI-340 with the `batman` software [7]. Bottom: Residual *Kepler* transit light curves of KOI-340 compared to the model generated from the parameters from the DR25 [6] data release versus phase. The out-of-transit data is in green, and the measurements made between the second and third contact points are in blue. The significant increase in in-transit scatter compared to the immediately adjacent out-of-transit data are the signature of the secondary star occulting starspots on the surface of the primary star. We have chosen not to plot the ingress and egress points to highlight the difference between the in-transit and out-of-transit points.
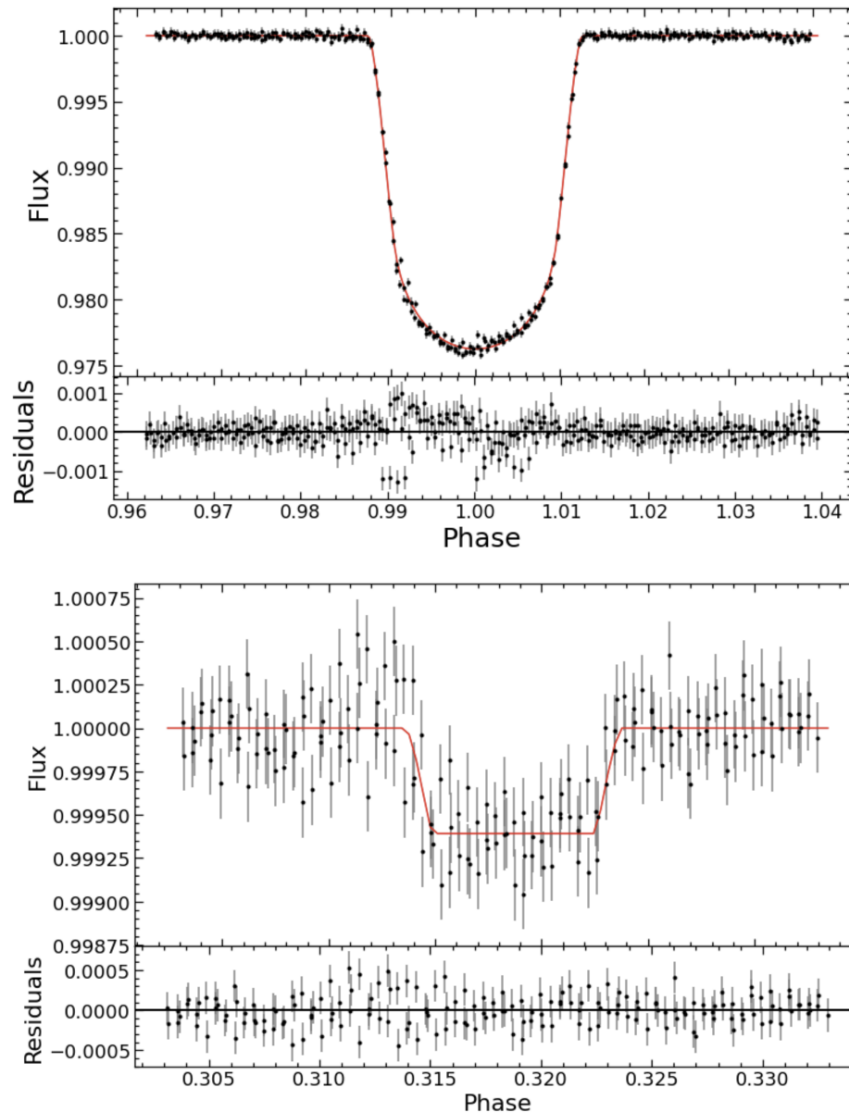
Figure 2.2: Top: Four normalized transit light curves of KOI-340 which show little or no starspot crossing features. The data are phase-folded with the period in Table 2.1 and plotted versus phase. The red line [8] model generated from the MCMC analysis of these primary transits along with the radial velocity measurements and secondary transits from *Kepler*. The depth of the transit derived from only unspotted transits is $\delta = 0.020164 \pm 0.000096$. Bottom: All normalized secondary transits observed in the long cadence *Kepler* data of KOI-340 phase-folded with the ephemeris presented in Table 2.1 and plotted versus phase. The red line model is generated from the MCMC analysis described in Section 3.2. The phase of the secondary transit occurs at 0.319 due to the eccentricity of the system.
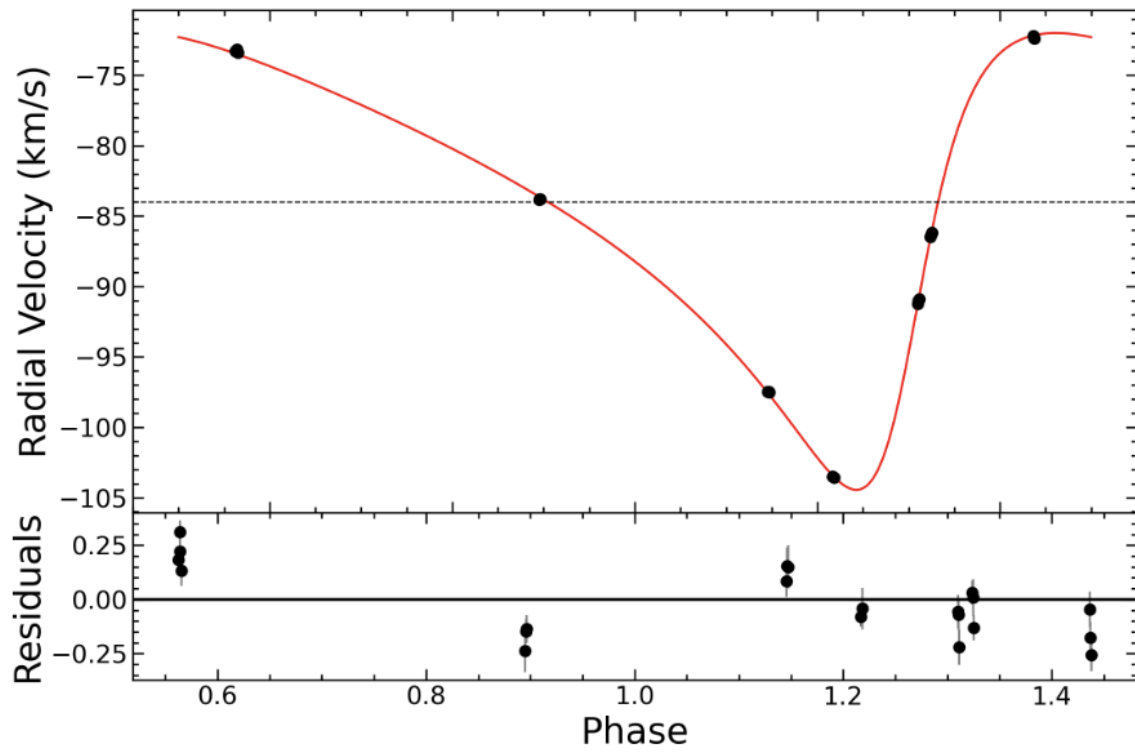
Figure 2.3: Radial velocity points from [9] of KOI-340 phase-folded with the ephemeris presented in Table 2.1 and plotted versus phase. The red line model is generated from the MCMC analysis described in Section 3.2.
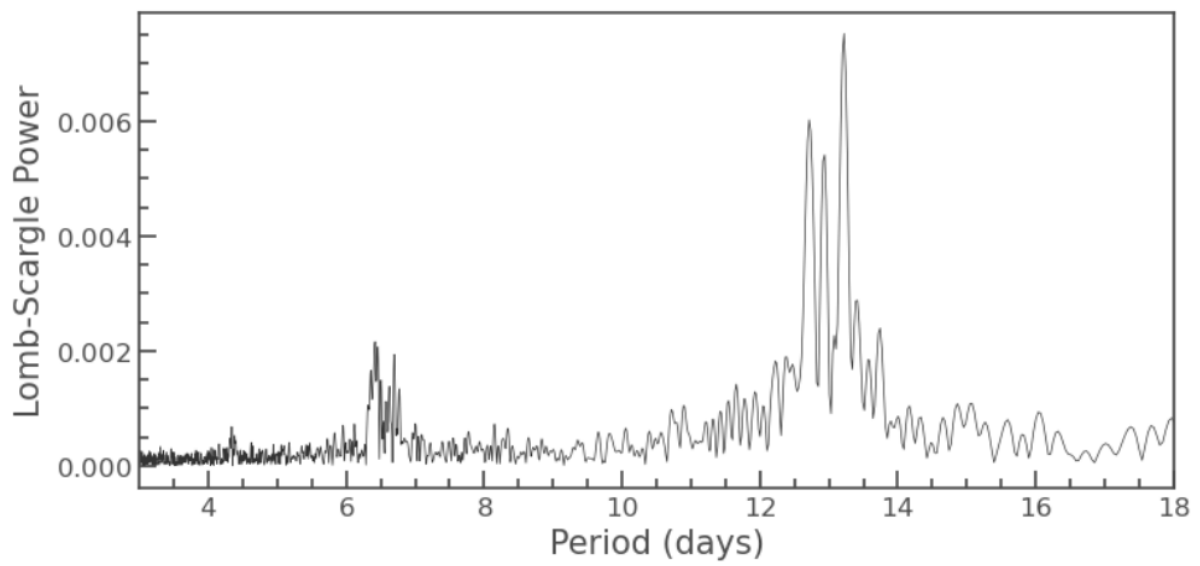
Figure 2.4: The Lomb-Scargle Periodogram over all *Kepler* data with primary transits removed. The period at maximum power suggests a rotational period for KOI-340 of 13.02 ± 0.97 days.
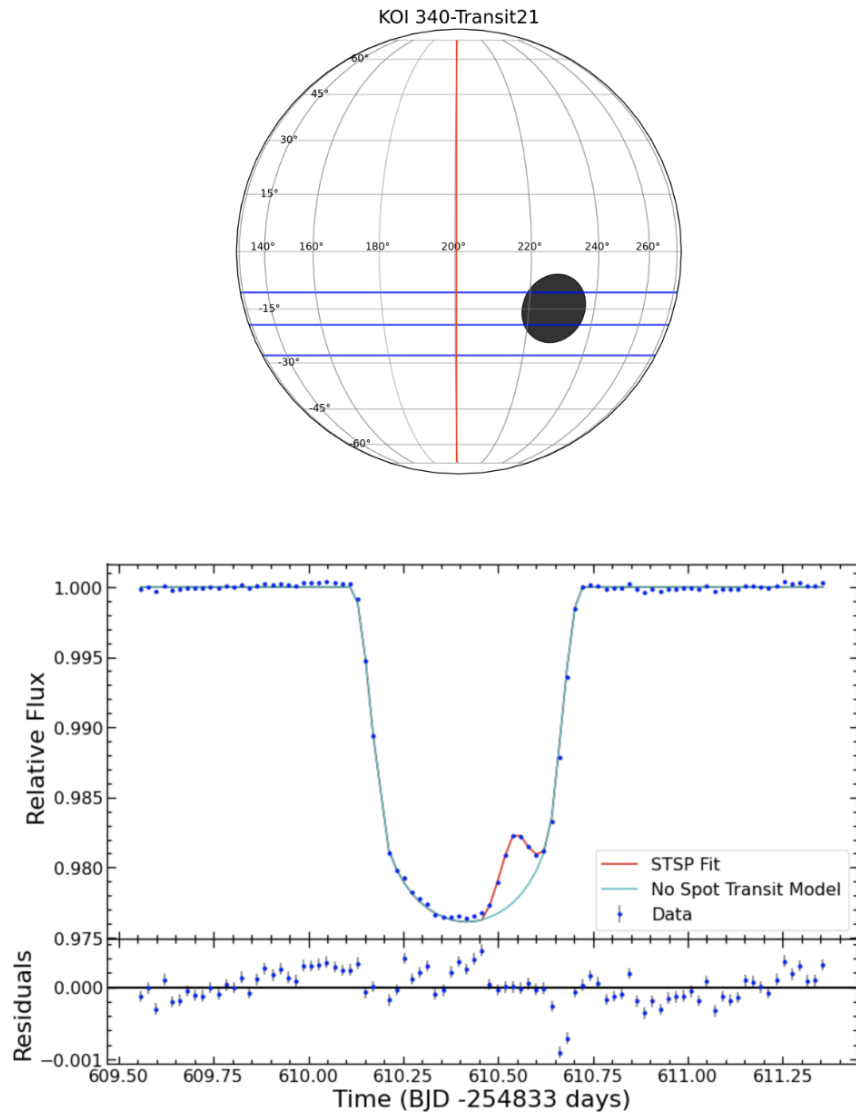
Figure 2.5: Top: Plot of the surface of KOI-340 with the final spot groups shown as black filled circles along with the red line denoting the longitude of the star at mid-transit and with blue lines denoting the full extent of the transit path for the secondary object. Bottom: Light curve for final `STSP` fit (red line) along with the no spot model for KOI-340 (cyan line) for Transit 21. The residuals (model - data) are shown below the light curve with blue point with the error bars shown as light gray lines.
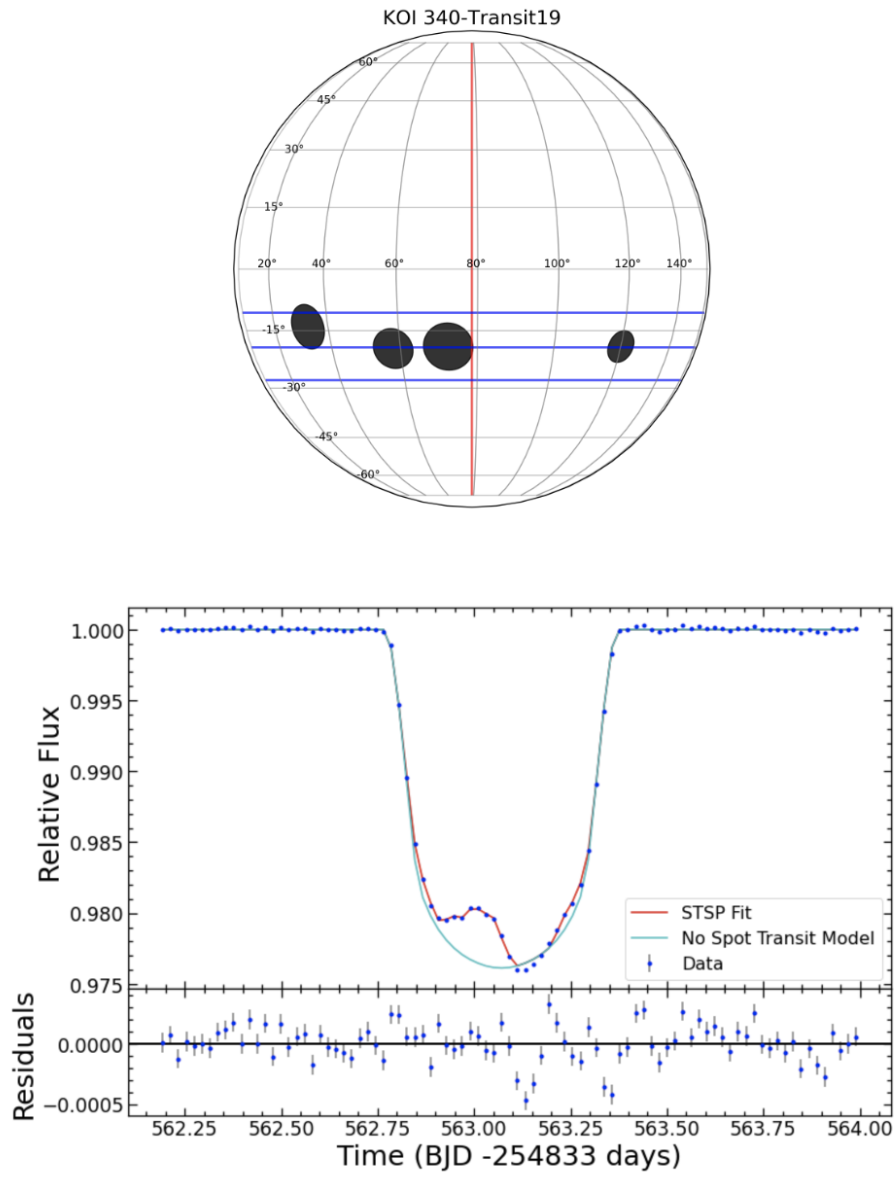
Figure 2.6: Similar plot to Figure 2.5 except for Transit 19.
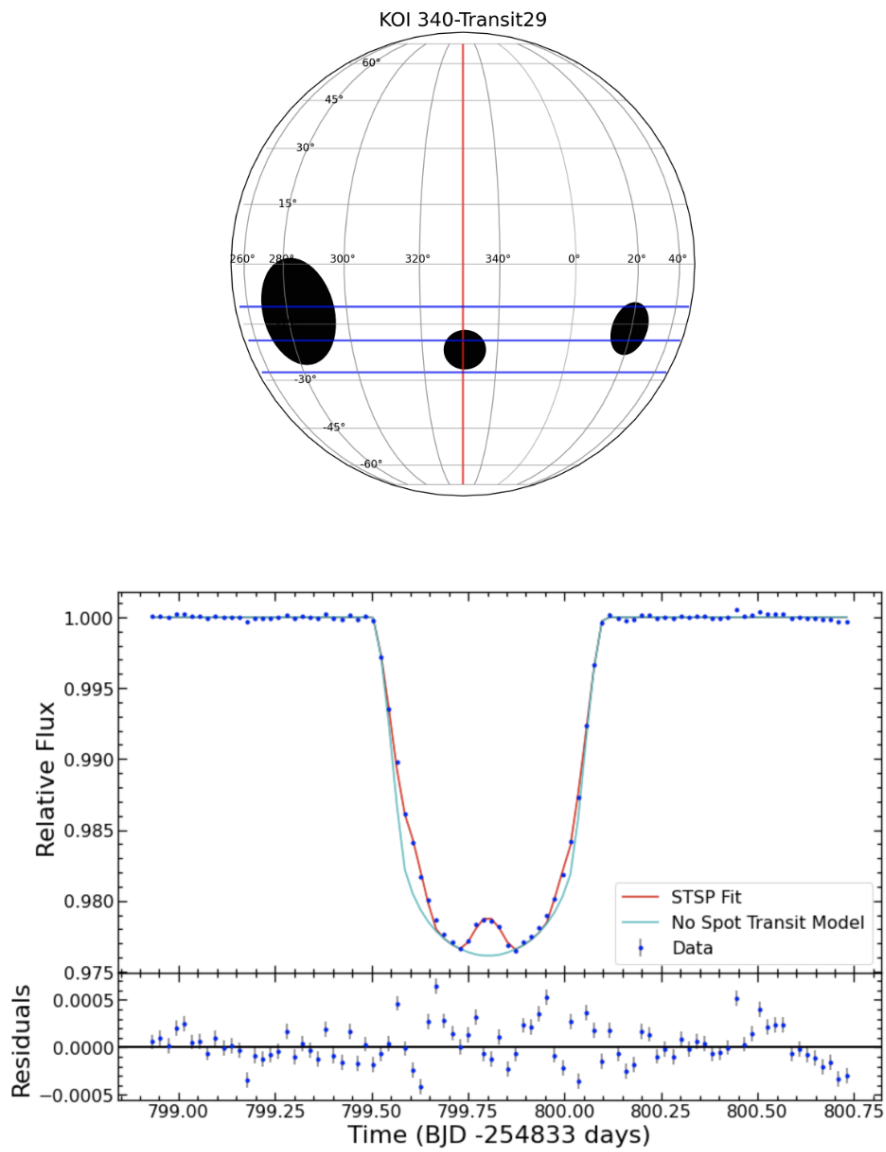
Figure 2.7: Similar plot to both Figure 2.5 and Figure 2.6 except for Transit 29.
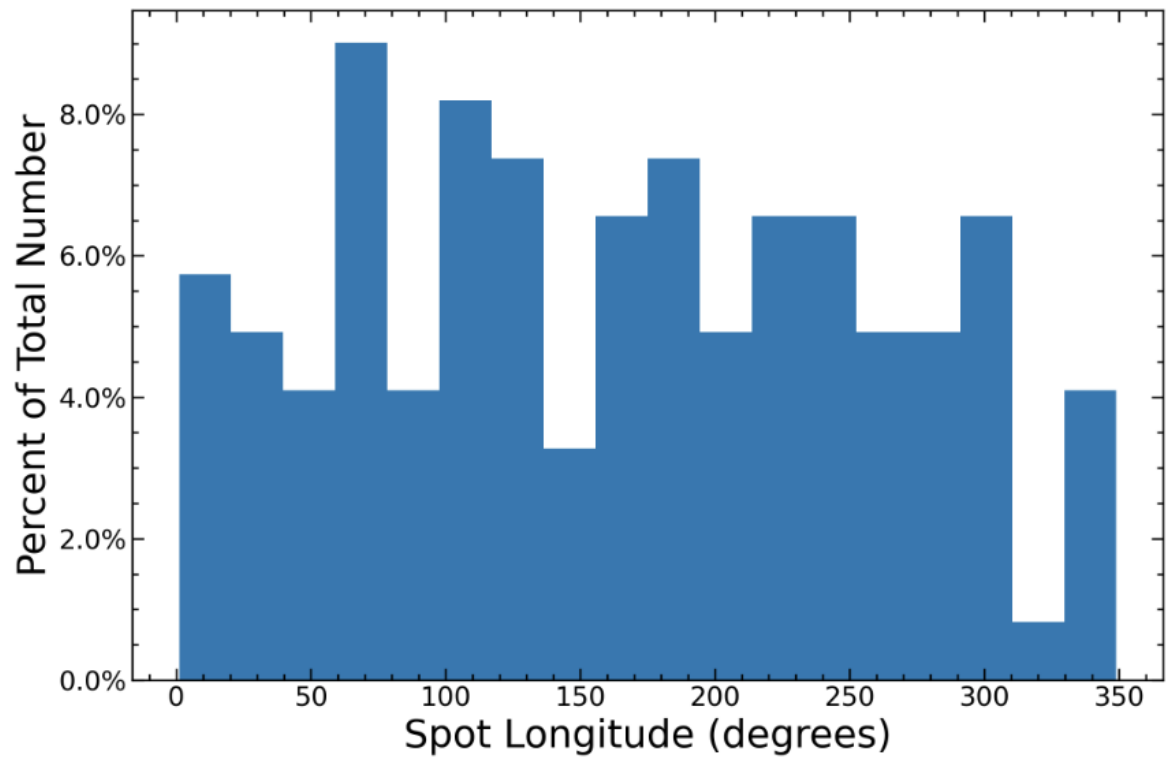
Figure 2.8: Distribution of spot group central longitudes for KOI-340 is shown here in blue. This distribution shows no true peak meaning KOI-340 has spots at every longitude equally. As there are no longitudes that are highly favored, it is unlikely the M dwarf companion is inducing spots on the surface of KOI-340 that are large enough to be detected over the rotation induced spots.
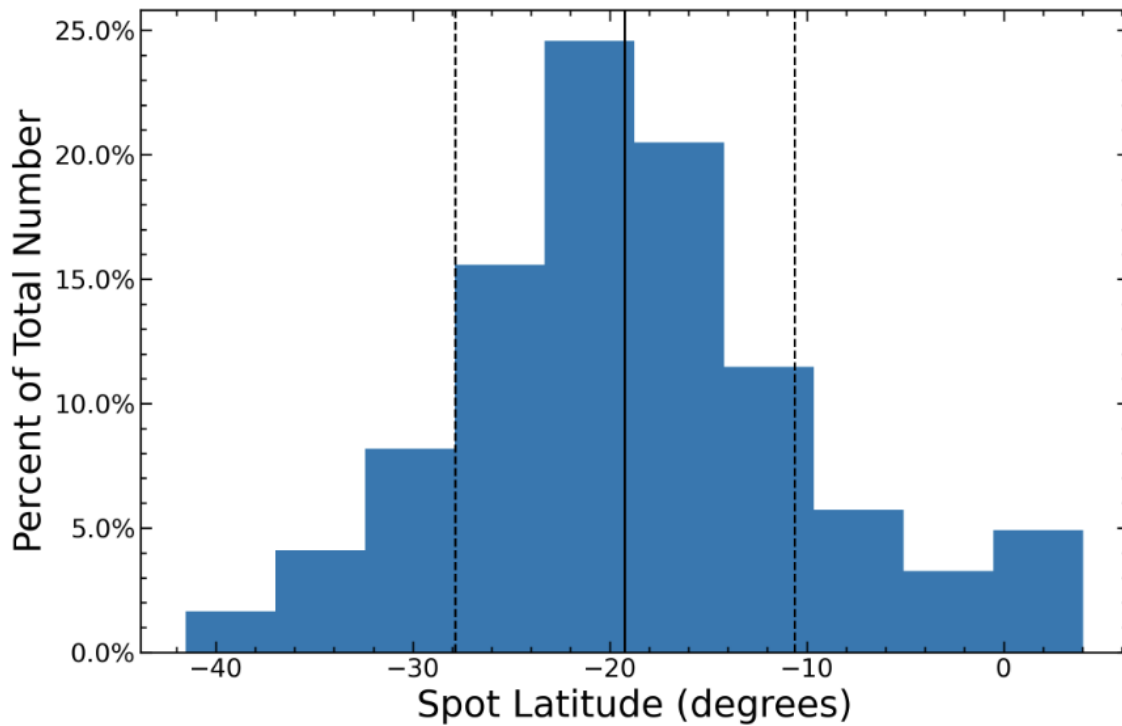
Figure 2.9: Distribution of spot group central latitudes for KOI-340 is shown here in blue. The distribution is centered at $-19.3°$, which coincides with where the M dwarf companion crosses (solid black line). The dashed black lines shows the full extent of the secondary crossing path. 24% of the spots fall outside the dotted lines and are thus grazing spots.
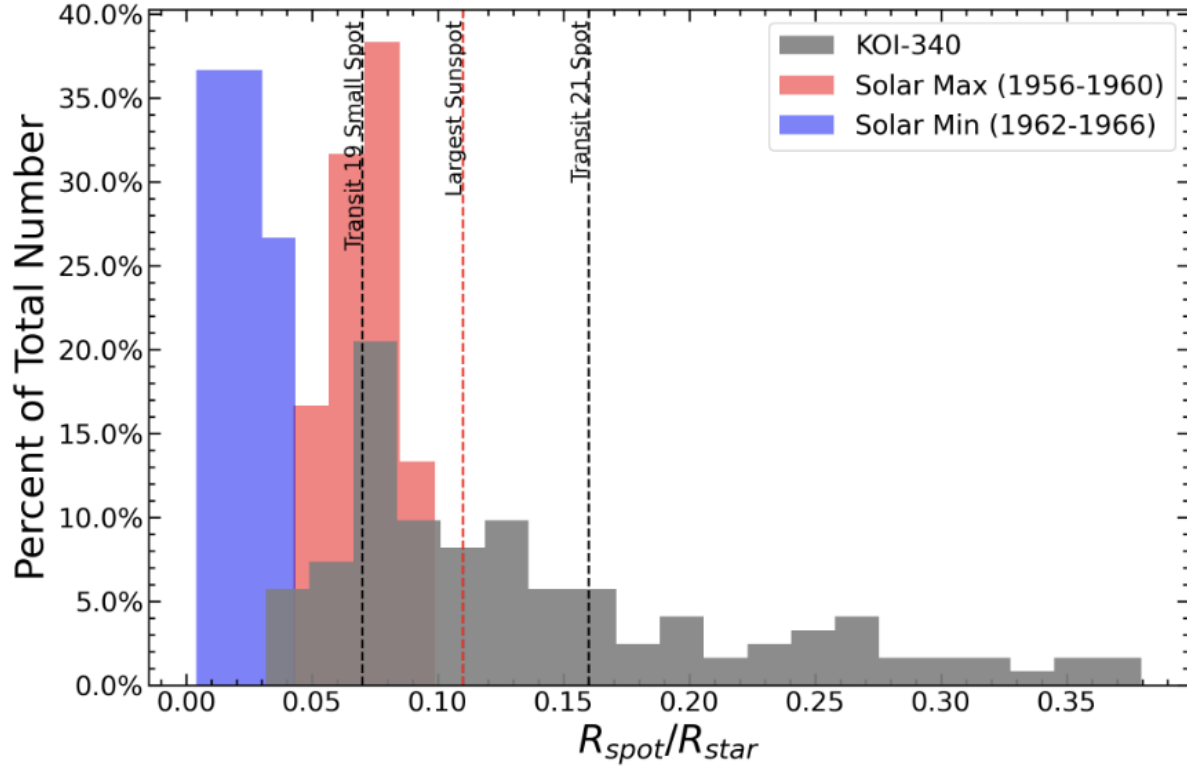
Figure 2.10: KOI-340's spot radius distribution is shown in grey with spot radius distributions for typical Solar maximum and Solar minimum sunspots over same duration as the *Kepler* mission (four years). Here the spot radius is given in relative radius, R_{spot}/R_* with a bin size width of 0.018 for all three distributions. For comparison, the black dotted vertical lines correspond to the smallest spot (centered around 563.25 BKJD) found in Transit 19 and the main spot (centered at 610.4 BKJD) found in Transit 21 (see Figures 2.6 and 2.5), and the red dotted line corresponds to the largest sunspot ever found by [10] converted to relative radius as shown in [4].
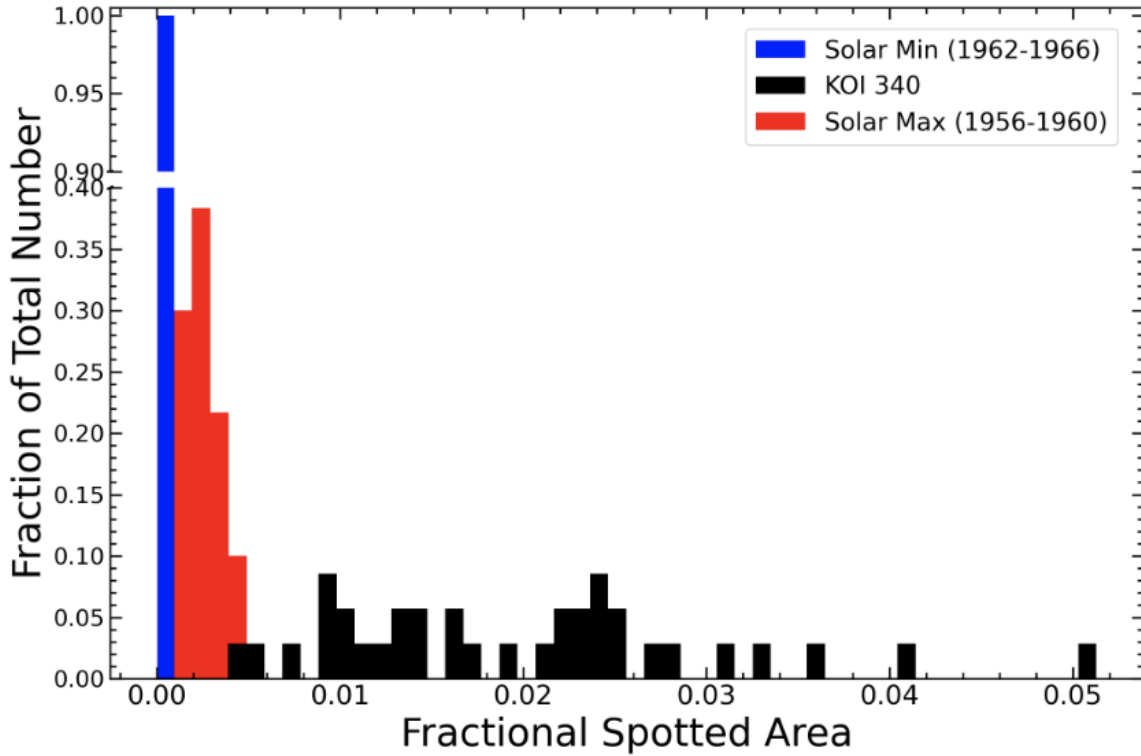
Figure 2.11: Area of transit crossing chord that is spotted assuming there are no spots anywhere else on the front hemisphere of KOI-340 is shown as the black distribution. This distribution is then the minimum fractional spotted area for the front hemisphere of KOI-340 compared to the Solar maximum fractional spotted area (red distribution) and Solar minimum fractional spotted area (blue distribution). The Solar maximum and minimum distributions are the same time frames as shown in Figure 2.10. All three distributions have bin sizes of 0.001 (or 0.1%) fractional spotted area. The y-axis has been broken from 0.4 until 0.9 as the Solar minimum distribution has much smaller fractional spotted areas so all of the values are in one bin.
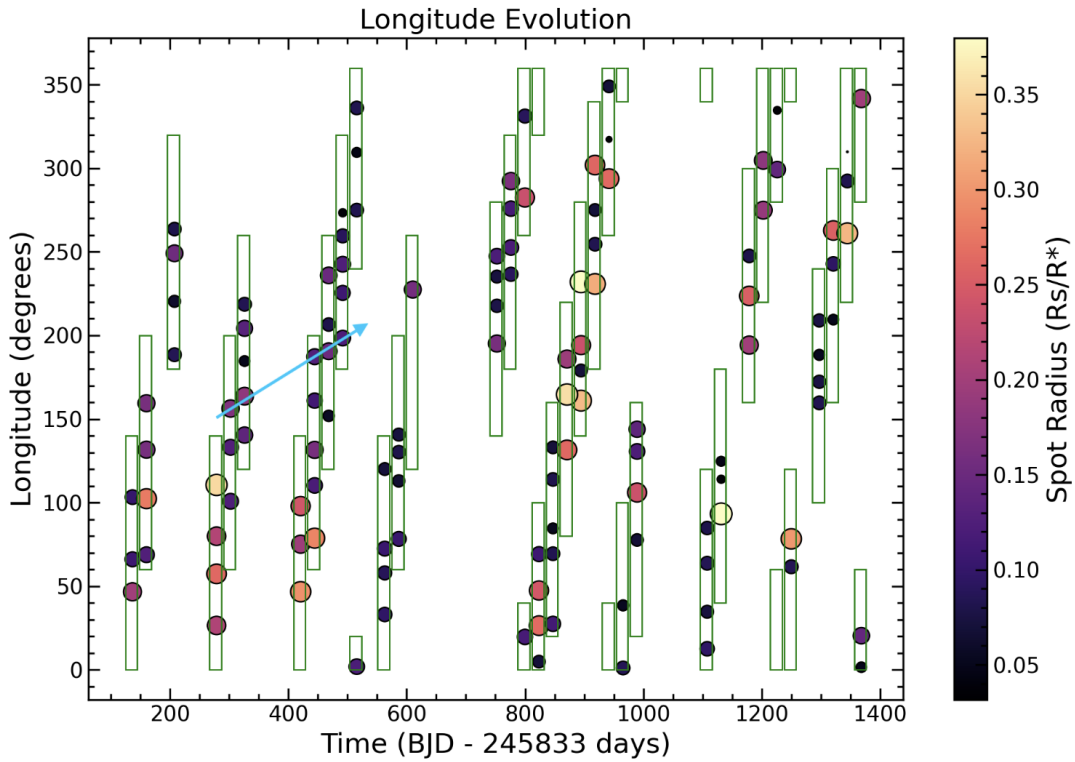
Figure 2.12: Plot of longitude versus time of all 122 spots modeled for KOI-340 with the markers being sized with respect to the relative radius of the spot group and colored with relative radius as well. The green boxes surrounding each transit correspond to the longitude coverage for each transit. When the green boxes overlap with the next transit, we looked for signs of the spots surviving to the next transit in order to search for signs of differential rotation. An example of this is shown with the overplotted cyan arrow which encompasses two such instances of possible signs of spots moving in longitude over time.
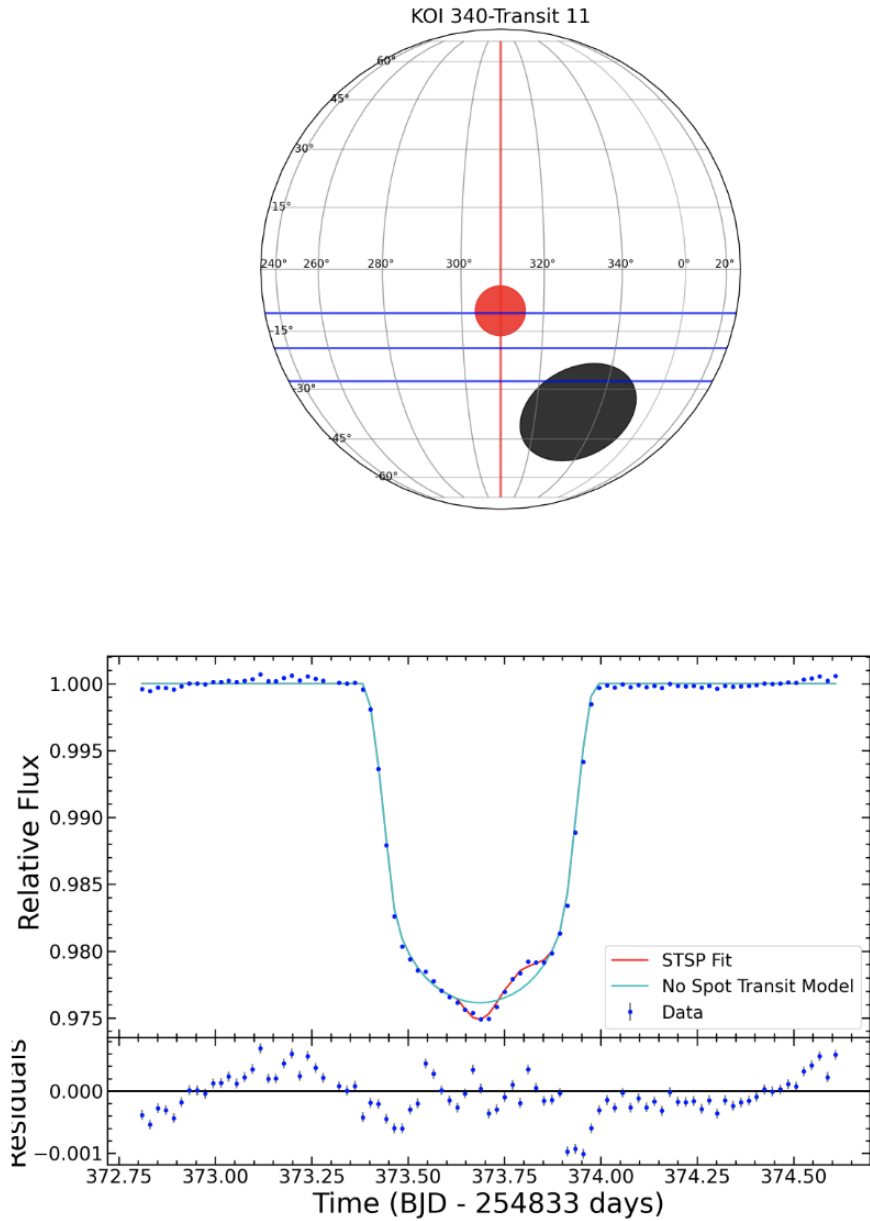
Figure 2.13: Top: Plot of the surface of KOI-340 with the final spot groups shown as black filled circles along with the red line denoting the longitude of the star at mid-transit and with blue lines denoting the full extent of the transit path for the companion. Red circle denotes the bright spot modeled in this transit. Bottom: Light curve for final STSP fit (red line) along with the no spot model for KOI-340 (cyan line) for Transit 11. The residuals (model - data) are shown below the light curve with blue points.
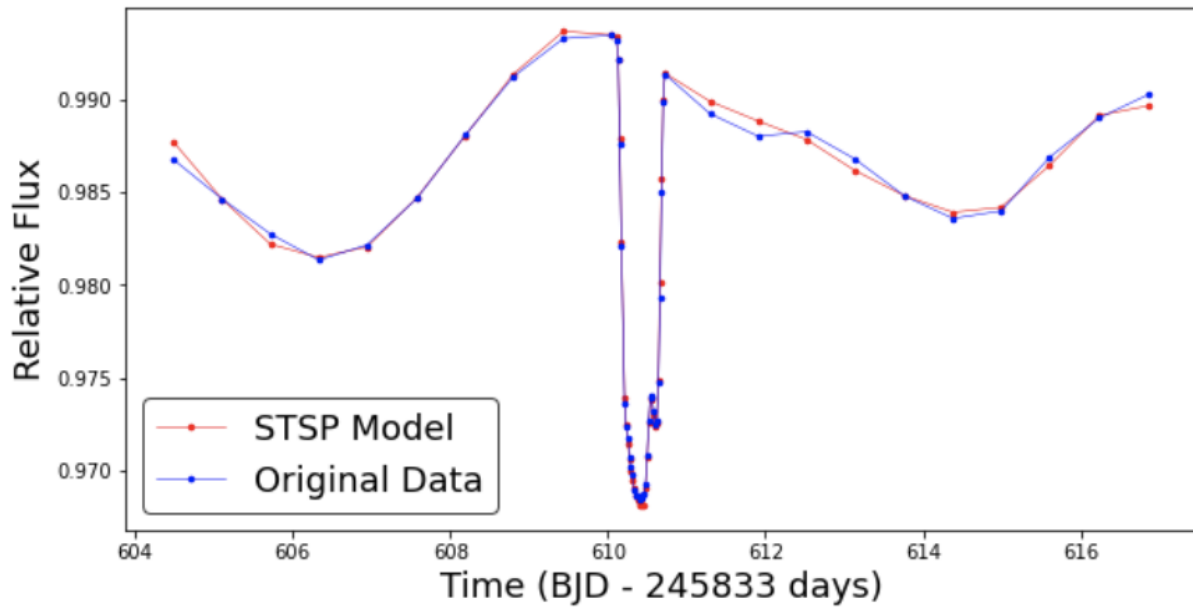
Figure 2.14: Full light curve encompassing one full rotation period (12.96 days) for simplest primary transit model (Transit 21). The original *Kepler* data is shown in blue with the STSP model shown in red. Three spots were needed (at minimum) to model the full light curve in addition to the one fixed in-transit spot.
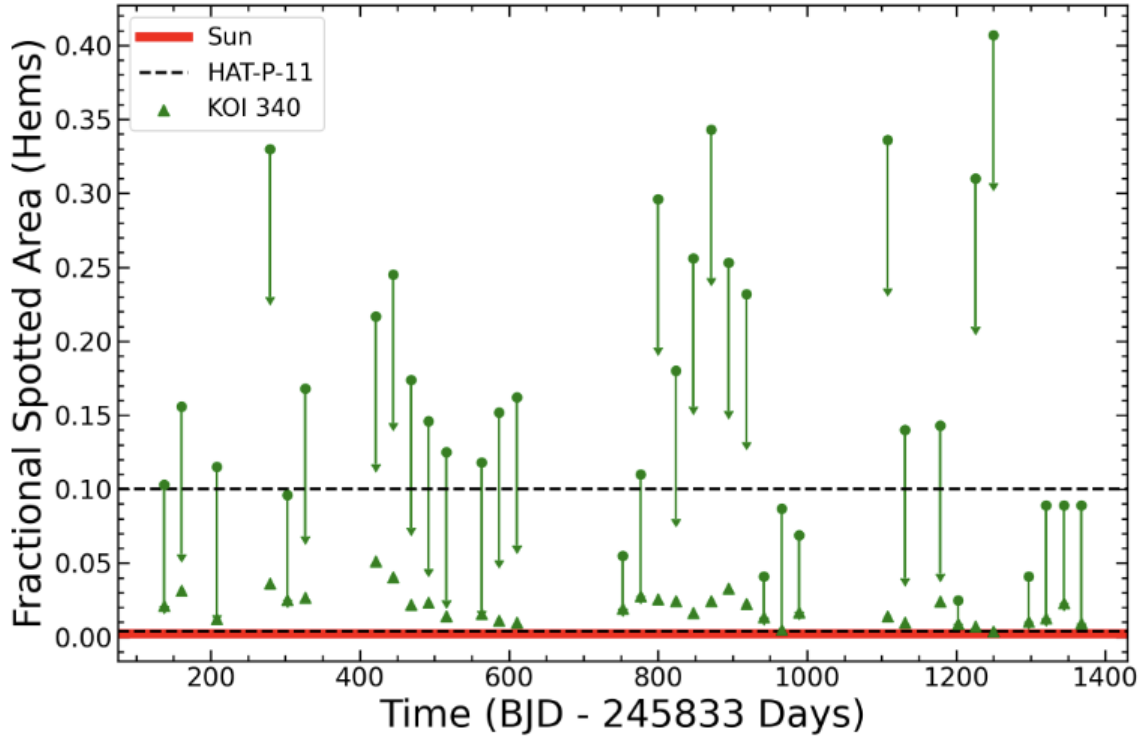
Figure 2.15: Fractional spotted area plotted versus midpoint time of primary transits in BKJD. KOI-340 is shown using green symbols with the Sun's total fractional spotted area coverage given as a solid red bar [11] and HAT-P-11's range of fractional spotted areas given as two black dashed lines [4]. The green upper triangles denote the minimum fractional spotted area for that transit found using the in-transit spots, and the green points are positioned at the total fractional spotted area found using the full out-of-transit light curve modeled using the minimum number of additional spots as described in Section 2.4.6.
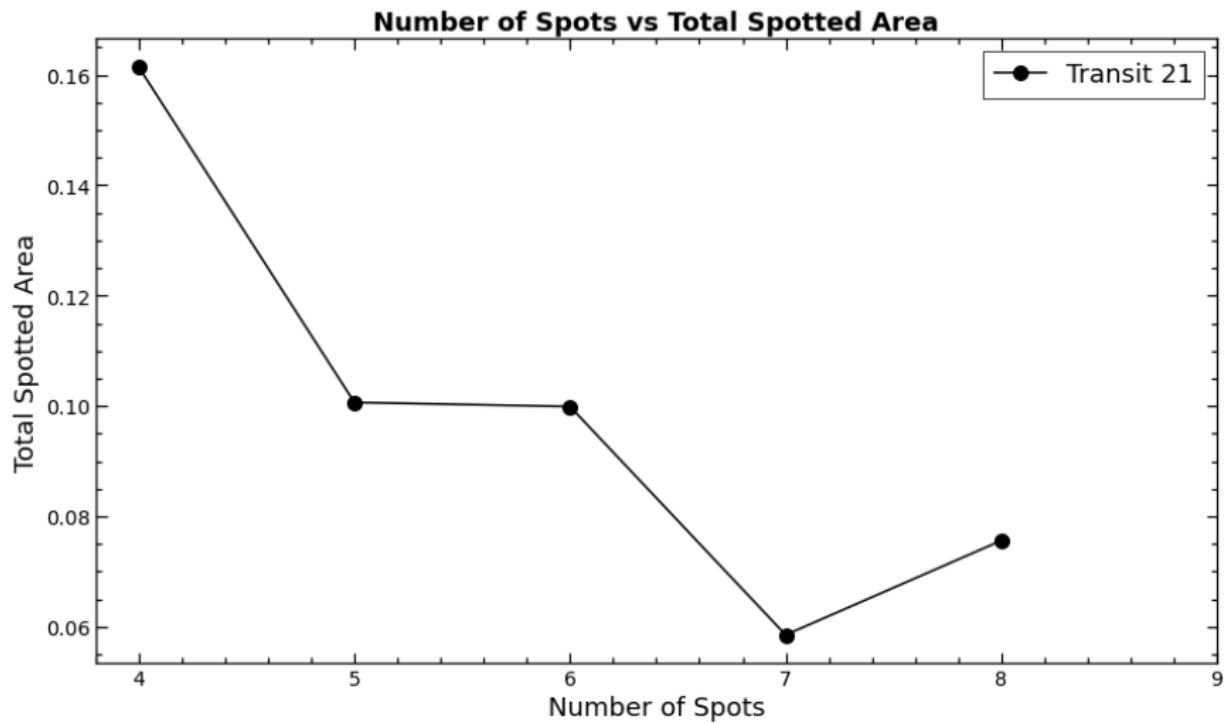
Figure 2.16: Total spotted area for Transit 21's full out-of-transit light curve plotted versus total number of spots needed to fit the data. The in-transit spots are fixed at 1, so in total 7 additional spots were needed until the fractional spotted area started to level out. The minimum number of spots needed to fit the data was 3, so we added more spots on top of those 4 until the spotted area starts to level out meaning we are approaching the minimum total spotted area for the entire star.
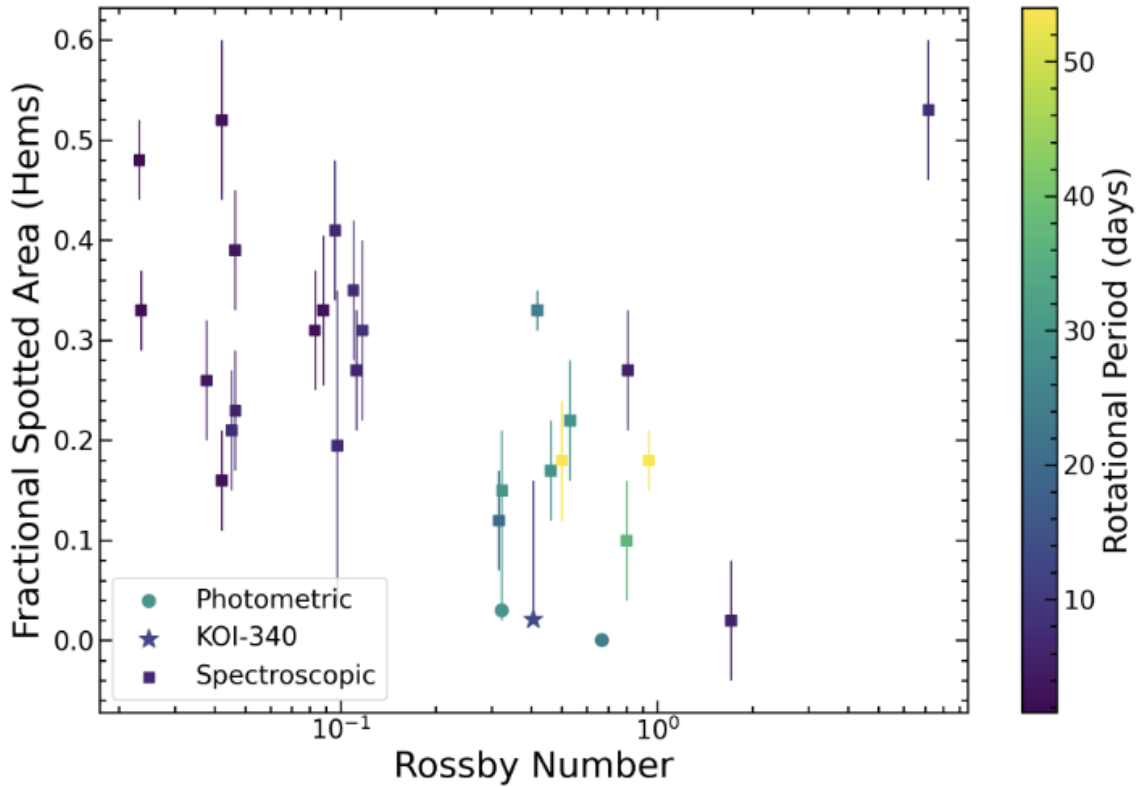
Figure 2.17: Fractional spotted area of stars from [12, 13, 14, 4, 15, 11] versus their Rossby number. The points are colored by their rotational period in days. Rossby numbers were calculated using their convective turnover time in days derived from their (B-V) color as done in [16]. Stars that have their fractional area derived from spectroscopic methods are plotted using square symbols with the other photometric methods denoted by a circle symbol. KOI-340 is denoted with a star symbol around 0.4 in Rossby number with a dark blue color. The Sun is the blue point around 0.65 in Rossby number with no clear error bar, and HAT-P-11 is shown as both a light blue circle and square around 0.3 in Rossby number as it has both photometric and spectroscopic fractional spotted area measurements [4, 15].

Chapter 3

Measuring the Temperature of Starspots Using Multi-filter Photometry

Reproduced from my first author paper accepted to AAS Journals in June 2023. As this paper is undergoing final edits still, I have reproduced the author list here:

- Maria C. Schutte; Homer L. Dodge Department of Physics and Astronomy, University of Oklahoma, 440 W. Brooks Street, Norman, OK 73019, USA

- Leslie Hebb; Department of Physics, Hobart and William Smith Colleges, 20 St. Clair Street, Geneva, NY 14456, USA

- John Wisniewski; George Mason University Department of Physics & Astronomy, 4400 University Drive, MS 3F3, Fairfax, VA 22030, USA

- Caleb I. Canas; NASA Postdoctoral Fellow, NASA Goddard Space Flight Center, 8800 Greenbelt Road, Greenbelt, MD 20771, USA

- Jessica E. Libby-Roberts; Center for Exoplanets and Habitable Worlds, Department of Astronomy & Astrophysics, 525 Davey Laboratory, The Pennsylvania State University, University Park, PA 16802, USA

- Andrea S.J. Lin; Center for Exoplanets and Habitable Worlds, Department of Astronomy & Astrophysics, 525 Davey Laboratory, The Pennsylvania State University, University Park, PA, 16802, USA

- Paul Robertson; Department of Physics and Astronomy, University of California - Irvine, 4129 Frederick Reines Hall, Irvine, CA 92697, USA

- Guomundur Stefansson; NASA Sagan Fellow, Department of Astrophysical Sciences, Princeton University, 4 Ivy Lane, Princeton, NJ 08540, USA

3.1   Introduction

It is well accepted that the Sun's myriad of activity signatures, including Sunspots, Sunspot cycles, flares, and coronal mass ejections are driven by Solar dynamo theory charbonneau2014. Our proximity to the Sun enables us to quantify the complex short and long time-scale evolution of activity phenomena across a multitude of wavelength regimes, providing rich

observational constraints on dynamo theory. Sunspots form in groups and have a non-uniform temperature (e.g. solanki2003). The complex and varied sizes and shapes of Sunspot groups constrains the underlying magnetic activity driving their creation zirin1998.

Starspots, the equivalent of sunspots on the surfaces of other stars, are a cornerstone observable that constrains our understanding of magnetic activity levels, variations, and magnetic cycles of stars other than the Sun. Numerous techniques are capable of identifying and characterizing starspots, such as Doppler imaging vogt1987,barnes2001,barnes2015, spectropolarimetry donati1997, and long-term photometric and spectroscopic observations mcquillan2014,morris2017b,howard2021,anthony2022. Starspots have been studied on a variety of stars, including giants berdyugina1998,oneal2004, subgiants gosnell2022,schutte2022, M dwarfs bergyugina2005,dave2015,robertson2020, K dwarfs morris2017, and young Solar analogues netto2020.

Spot sizes and spot temperatures are two key observational parameters that are useful for characterizing starspot activity. Quantifying these parameters has broad applicability to the interpretation of exoplanet transmission spectroscopy, whereby spot activity is known to contaminate efforts to characterize exoplanetary atmospheric properties alam2018,rackham2018,bruno2018,bruno2020. Even small covering fractions of 1%, starspots would be the largest source of contamination when trying to retrieve an exoplanet's atmosphere from transmission spectroscopy pont2007.

Spectroscopic starspot measurements on giant and subgiant stars are able to measure the darkest portion of the spot because the activity lines appear only at low temperatures, so their starspot temperature measurements are on the order of $\Delta T = 1000\ K$. Additionally, covering fractions (i.e. the total area across the surface of the star covered by spots) on giants and subgiants can be measured as upwards of $\sim 40\%$. However, these methods lend themselves well to statistical studies and empirical relationships between the temperature of a star and the temperature of a starspot as shown in bergyugina2005 and herbst2021. As noted in both papers, these empirical relations should be treated with caution as they fail to reproduce the well known solar spot temperature contrasts. While they should be applicable to all types of stars, it is best to be cautious especially around younger G type stars and older Solar analogues.

Historically, quantifying the temperatures of starspots has been pursued using integrated optical spectroscopic observations of cool stars, for example by leveraging the different temperature sensitivities of TiO bands (i.e. TiO $\delta\ 8860\mathring{A}$) in the red-optical neff1995,oneal1996. TiO only appears at much lower temperatures (e.g. $\Delta T \simeq 1000K$) than the photosphere of G and K type stars oneal2004, making it a particularly good diagnostic of spot temperatures for these stars. With the correct spot covering fraction and a model of an inactive M-dwarf

spectrum for the spots and an inactive stellar temperature spectrum for the star, the active host star's spectrum can be reproduced.

It is more challenging to measure spot temperatures in M dwarfs using TiO lines as activity and the photospheric contributions blend bergyugina2005. Spot temperature measurements typically require estimates to be made about the spot covering fractions at the time of spectroscopic observations, but starspot distributions can change dramatically over time, including over single stellar rotation periods, which can impact efforts to approximate covering fractions. Recently two-temperature spectral deconvolution analyses have constrained spot filling factors by the broad photometric modulations they produce gosnell2022 while using simultaneous spectra to measure the spot temperature.

High cadence, high precision photometric observations of starspot crossing events, whereby a companion transits a starspot or plage feature, enable precise measurements of the covering fraction, size, and number of starspots on the surface of the star wolter2009,morris2017, netto2020,schutte2022,3884. Because there is a degeneracy between the sizes, location, and temperatures features measured via starspot crossing events, this method requires one to make an assumption of the temperature of the starspots. In this paper we explore use of high-precision, multi-filter photometric observations of starspot crossing events to simultaneously determine both temperatures and sizes of individual starspots.

HAT-P-11 is a K4 dwarf star with two planets, a close in Neptune-sized planet that orbits every 4.88 days bakos2010 and gas giant planet that orbits every $\sim$ 9 years yee2018. Only the Neptune-sized planet (HAT-P-11b) is known to transit the star, but the planet's orbital axis is oriented at an oblique angle compared to the star's spin axis. winn2010 found the sky-projected angle between the spin axis and orbital plane to be $\lambda = 106^{+26°}_{-10}$ from the observations of the Rossiter-McLaughlin effect. HAT-P-11 exhibits high level of activity, with 95% of HAT-P-11b's *Kepler* transits exhibiting starspot crossing events morris2017. Modeling these starspot crossing events led morris2017 to determine that HAT-P-11's starspots were similar in physical size to Solar maximum sunspots but had covering fractions nearly two orders of magnitude higher than the Sun.

One of the major assumptions used to model HAT-P-11's starspots was the spot contrast, i.e. the ratio of the integrated flux of the spot compared to the star's unspotted photosphere. morris2017 used the area-weighted contrast of sunspots (c = 0.3) which blends the sunspot umbra and penumbra temperatures with their appropriate areas. In this paper, we will describe our technique to simultaneously spot sizes and temperatures on HAT-P-11, using simultaneous multi-band transit photometry obtained with LCOGT's MuSCAT3 instrument on the 2.0-meter telescope at Haleakala Observatory.
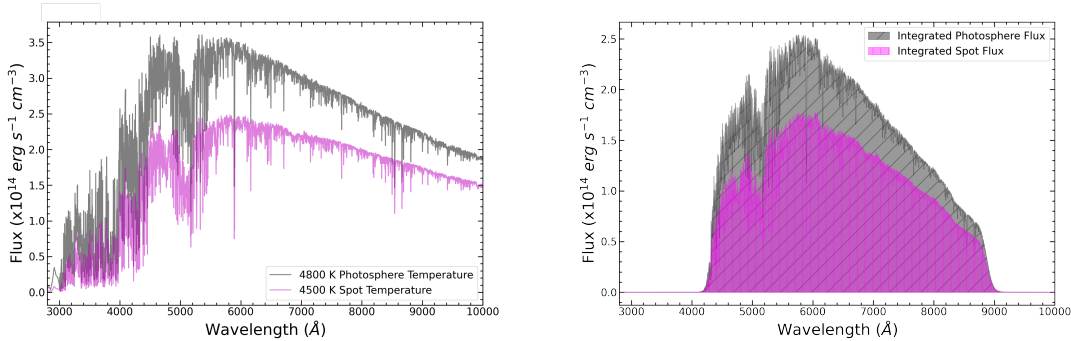
Figure 3.1: **Left:** HAT-P-11's stellar photosphere spectrum with $T_{\rm eff} = 4800\ K$ and $\log g = 4.5$ in grey. Spectrum for spot temperature of 4500 K and $\log g = 4.5$ is shown in magenta. Spectra were obtained using the `expecto` python package, which provides a PHOENIX model spectrum for the closest grid point for an input effective temperature and surface gravity for solar metallicity stars. **Right:** The fluxes over which the spectra were integrated for the *Kepler* filter for the photosphere and spot are shown in filled in hatches of grey and magenta respectively. Once integrated over, the hatched regions correspond to the I_{spot} (magenta) and I_{phot} (grey) in Equation (1) which becomes a contrast of 0.31.

3.2 Methods and Analysis

3.2.1 Modeling Active Regions on HAT-P-11

morris2017 used the program STarSPot[1] (`STSP`) to model the starspot crossing events in *Kepler* observations of HAT-P-11. `STSP`'s functionality has been described and applied to model starspot characteristics in other cool star systems dave2015, morris2017,wisniewski2019,schutte2022,3884. `STSP` generates synthetic light curves for a star using a pre-defined number of static, non-overlapping spots or spot complexes, and computes spot properties from a χ^2 comparison between observed and synthetic fluxes using an affine-invariant Markov Chain Monte Carlo (MCMC) based on foreman2013.

3.2.2 Synthetic Spectra and Theoretical Contrast

The contrast of a starspot is approximated as:

$$c = 1 - I_{spot}/I_{phot} \tag{3.1}$$

where I_{spot} is the integrated flux of the spot in a given wavelength range and I_{phot} is the integrated flux of the photosphere in the same wavelength range solanki2003. Previously

---

[1]The code for STarSPot can be found here: https://github.com/lesliehebb/STSP.

when modeling the active regions of HAT-P-11, morris2017 adopted the area weighted mean sunspot contrast of 0.3, as this contrast was found to best fit the data when they tested a range of contrasts ($c = 0.15$-0.8). The area-weighted contrast takes into account the difference in contrast and area between a sunspot's umbral and penumbral regions with the umbra being much darker but also much smaller. morris2017 used a mean umbral contrast of 0.65 and mean penumbral contrast of 0.2 with the penumbra having an area around four times larger than the umbra solanki2003, which provides an area-weighted sunspot contrast of 0.3. Then, after testing the contrast of 0.3 along with contrasts of 0.15, 0.6 and 0.8, morris2017 found that 95% of spots in the data were fit with the area-weighted sunspot contrast.

In order to theoretically determine the spot contrast needed for a filter, a synthetic spectrum is needed for both the photosphere's temperature and for the spot's temperature, with the surface gravity assumed to be the same across the entire region of the star. We used the python package `expecto` which retrieves PHOENIX phoenix synthetic model stellar spectra for the closest grid point to the input photosphere's temperature and surface gravity (i.e., the effective temperature is rounded to the closest 100 K temperature and the surface gravity is rounded to the nearest half), though it only allows for solar metallicity spectra.[2]. Figure 4.13 shows the PHOENIX synthetic spectrum for HAT-P-11's stellar photosphere.

After obtaining synthetic spectra for the photospheric temperature and a range of spot temperatures, we multiplied each spectrum with the filter response curve for each bandpass of interest. The filter response curves were obtained using the SVO filter profile service rodrigo2012,rodrigo2020. For our purposes, we used the following filters: SDSS g', r', i', and z' sdss; *Kepler* kepler; TESS tess; and OAO Zs muscat3. Once we multiplied each spectra for all of the filters, we finally integrated over the wavelength region of the filter for both the stellar photosphere and the starspot temperature.

For HAT-P-11, we used a stellar photosphere temperature of 4780 K (rounded to 4800 K) and a surface gravity of 4.59 bakos2010 (rounded to 4.5). We used a range of active region temperatures starting at 3700 K and increasing by 100 K until we reached 4700 K. The calculated contrasts for each spot temperature and filter are shown in Figure 3.2 with contrast values plotted at their central wavelength. When looking at the *Kepler* filter, the closest spot temperature that matches the data is 4500 K (black star indicates this point), which corresponds to a contrast value of 0.31. The metallicity of a star will also affect the theoretical stellar spectrum, so we explored using a more metal rich theoretical stellar spectrum to better match HAT-P-11's metallicity of [Fe/H] = +0.31. Using SVO's theoretical stellar spectra service, we obtained a BT-Settl synthetic spectrum for HAT-P-11's metallicity, surface gravity, and all photosphere and spot temperatures. With the different metallicity

---

[2]https://expecto.readthedocs.io/en/latest/index.html

spectra, we performed the exact same procedure as just described and found the contrast values themselves are changed on the order of 0.01%, so for HAT-P-11, the metallicity does not affect the contrast values significantly, though this could impact other stars of even higher or lower metallicity more substantially.

3.3 LCO MuSCAT3 Observations

3.3.1 MuSCAT3 Simultaneous Multi-filter Photometry

Using the theoretical contrast values for a variety of spot temperatures for HAT-P-11, the next step is to compare those contrast values using data from multiple filters including the *Kepler* bandpass morris2017 used in modeling the *Kepler* transits. However, to ensure that we are comparing the same active region occultation in each filter, simultaneous multi-filter photometry is needed. One such example of this type of instrument is LCO's MuSCAT3 instrument on the 2.0-meter FTN telescope at Haleakala Observatory muscat3. MuSCAT3 allows for simultaneous multi-band photometry in four filters: SDSS g', r', and i' and OAO Zs. Unique to MuSCAT3 are the available engineered diffusers for each of the four filters. These types of diffusers increase the precision of ground-based photometry of transiting systems to the level of space-based data stefansson2017. For a bright target like HAT-P-11, the diffusers allow for the precision needed to potentially observe a starspot occultation. We were awarded time with this instrument to observe two nights to increase our chances of observing a starspot crossing event. We observed one full transit of HAT-P-11b on June 29th, 2021.

HAT-P-11

On June 29th, 2021, we obtained a full transit of HAT-P-11b using the MuSCAT3 instrument. With magnitudes around 9 in all four filters (SDSS g', r', and i' and OAO Zs), we opted to use available diffusers for each filter as the diffusers reduce the scintillation noise. Due to the nature of the instrument, the light from the star is split into four, so the amount of light in each filter is reduced compared to a single filter CCD. Because of this fact, the exposure times used were 40 seconds in the r' and i' filters and 70 seconds in the g' and Zs filters. These long exposures lead to peak counts of 65,000-100,000 ADU, which is well below the saturation limit for each CCD ($> 100,000$ ADU). These data were automatically processed using the LCO BANZAI pipeline muscat3. We then ran each individual filter through the multi-aperture photometry process using AstroImageJ collins2017. The precision for this transit was excellent with all filters having <1 mmag precision. There is one section of all

four light curves that is slightly worse at the very start of the observation, which is attributed to partly cloudy weather at that time. Even after removing the poor section at the beginning of the night, it does not appear that there was a visible active region occultation at any point in the transit.

In order to further constrain the limits on a spot crossing event in the transit, we binned the data to 200 seconds for the SDSS r' and i' filters and 210 seconds for the SDSS g' and Zs filters and plotted all of the filters at once in Figure 3.3. We also plotted the residuals of the the binned data with respect to the no spot transit model for each filter with each filter having different four-parameter limb darkening coefficients but otherwise consistent transit model parameters claret. For Figure 3.3, we chose to show one example no spot transit model in cyan for the SDSS r' transit. From the residuals, we see no evidence of a color-dependent spot crossing event during this transit, though there is a bump around mid-transit present only in the Zs filter which is further discussed in Section 3.3.2. Even with the excellent precision data (less than 1 mmag in every filter's unbinned data), there is a possibility that there was a spot in the path of the planet during this transit, but the spot was too small to detect.

3.3.2 Simulated Light Curves

Since we did not observe a starspot crossing occultation in our MuSCAT3 transit of HAT-P-11b, we instead looked to *Kepler* transits of the planet to test our theoretical contrast values for various filters. First, we chose a transit of HAT-P-11b that had one unusually large starspot and one smaller, more typical size starspot for HAT-P-11 (see Figure 3.4). Considering the starspots for this transit have already been modeled by morris2017 using STSP, we know the radii and locations for the two spots as shown in Figure 3.4. Using this information and our theoretical contrast values, we can model how the spot occultation changes with different contrast values using STSP. We can then use this data to estimate what we should have been able to observe with MuSCAT3 data if there were similar size spots in the transit we obtained.

First, we must assume a spot temperature in order to know which contrast values to use for the four MuSCAT3 filters. If we were to use the empirical equations from herbst2021 to estimate the temperature of the active regions of HAT-P-11, the spot temperature would be around 3700-3800 K (a difference of $\sim$ 1000 K from the photosphere). However, as seen in Figure 3.5, the STSP models for all of the filters including the *Kepler* bandpass result in starspot crossing events that are too high and do not match the data well as these methods determine the temperature for the darkest starspot regions rather than the average temperature. If we instead find the spot temperature that best matches the *Kepler* data, the

spot temperature would be 4500 K as seen in Figure 3.6, which also shows that the `STSP` models are much closer to the correct height. As a spot temperature of 4500 K matches the data the best, we will use that spot temperature for the rest of the paper. Though a 4500 K spot temperature best matches the data, there is no way to confirm with only one filter, and if the spot radii and positions changed slightly, the best fit spot temperature could change.

Even though we did not observe a starspot crossing during our HAT-P-11 MuSCAT3 transit, we were still able to use the excellent data collected to estimate what we could have observed. In order to simulate what the spots might look like for MuSCAT3, we took the data collected for each filter and subtracted the no spot transit model to get an accurate noise profile for the each filter with the same cadence as the observed data. Note there is a feature in the Zs band data around the transit midpoint that is attributed to noise as this feature is not present in any other filter, which is what would be expected for a starspot crossing event. Then, we added on our corresponding `STSP` model for a 4500 K starspot for each filter in order to simulate what the spots seen in this transit of HAT-P-11 would look like for the observed noise levels from our MuSCAT3 transit. Our simulated light curves for each filter can be seen on the right hand side of Figure 3.7 as the grey points with error bars. The real data from the LCO MuSCAT3 transit can be seen in the left hand side of Figure 3.7 for comparison. As there was a significant bump due to noise in the Zs band around the same location as one of the injected spots, there is a larger than expected first bump in the Zs simulated data due to the real noise of the Zs transit (bottom row of Figure 3.7). There is also an portion of the large bump feature in the SDSS r' simulated data (second row in Figure 3.7) that has higher than expected points due to real noise in the LCO data.

3.4   Results and Discussion

We will now treat our simulated HAT-P-11 data as the true data we received from MuSCAT3. Thus, we took the grey data points from Figure 3.7 and modeled them in `STSP` with the known spot parameters. Keeping the spot parameters the same for all four filters, the only independent variable to change is the contrast for each filter. We modeled eleven spot temperatures for each filter (3700 - 4700 K). Then, we compared all the spot temperature curves to the simulated data and calculated the χ^2 for each temperature. The comparison between the binned simulated data (pink points) and three different spot temperature models (4300 K, 4500 K, and 4700 K) are shown in Figure 3.8. For all four filters, the calculated χ^2 for each spot temperature model compared to the unbinned simulated data is the lowest for the 4500 K model. However, there is some uncertainty in the spot temperature such that the 4400 and 4600 K models have χ^2 values that fall within the $\Delta \chi^2$ of the 4500 K model. Thus,

the determined spot temperature for HAT-P-11's starspots would be 4500 ± 100 K.

Since the simulated data that we are modeling was created using the real noise for each filter, it is necessary to discuss each filter individually. For all of the four filters, there is a portion of the observation at the very beginning that is not fit well due to partly cloudy conditions during the observation. For the SDSS g' filter (top left panel of Figure 3.8), there is a dip in the real LCO data around 0.925 (2459395 BJD days) that leads to a dip in the binned simulated data (pink points). Additionally, the SDSS g' real LCO data has a starspot-like feature around 0.96 (2459395 BJD days) that doesn't appear in any of the other filters and is within the noise level of the transit, so it is likely noise and not a real starspot crossing event. This feature does coincide with the second injected starspot, which creates a larger than expected feature that could match a cooler spot temperature model, like the blue 4300 K spot model in Figure 3.8. Thus, if we only had the SDSS g' filter data, a cooler spot temperature might be measured, though the overall lowest χ^2 model is still 4500 K.

The SDSS r' filter (top right panel of Figure 3.8) has one unique aspect in that there was one section of higher noise around 0.955 (2459395 BJD days) in the real LCO noise. This noise again coincides with the start of the second injected starspot causing a higher than expected point in the binned simulated data in Figure 3.8 (pink points). However, even with this added noise, the lowest χ^2 spot temperature model is 4500 K as the χ^2 is calculated with respect to the unbinned simulated data compared to the spot temperature models. There is also a lower than expected portion in the simulated data around 0.97 (2459395 BJD days) that is caused by real noise in the LCO data. The SDSS i' filter (bottom left panel of Figure 3.8) shows a similar story to the SDSS r' band, but for the i', the noise is more pronounced starting around 0.93 (2459395 BJD days), which leads to higher than expected bumps in the binned simulated data for both injected starspots. Again, the lowest χ^2 spot temperature model is 4500 K when comparing the models to the unbinned simulated data.

Lastly, the Zs band (bottom right panel of Figure 3.8) has a unique feature around 0.92-0.94 (2459395 BJD days) in the unbinned simulated data. This creates a feature that has a higher amplitude than expected after we injected the smaller starspot into the real LCO noise. This noise is likely real noise (i.e. not a starspot crossing event) that is more pronounced due to this filter being very near-infrared and having the lowest efficiency of all the filters. Because this noise feature is so large, the first smaller feature is only fit with very cool spot temperatures (> 3900 K). The second larger injected starspot is fit very well with the 4500 K spot temperature model, and as this feature has less noise in the real LCO data, it is a better feature for comparison. Thus, the best spot temperature model, both by eye and by χ^2, when only considering the second feature is the 4500 K spot model.

Previously, starspot temperatures have been measured using spectroscopic techniques (see

bergyugina2005 and references therein). This technique has been applied to many different types of stars, and though it has been mostly G and K stars, it has not been used to measure the starspot temperature of HAT-P-11. morris2019 used a spot temperature difference of $\Delta T_{\rm eff} = 250\ K$ in their modeling of spectra obtained with the ARC 3.5-meter telescope at Apache Point Observatory, but that spot temperature was assumed in order to measure the spot covering fraction. morris2019 indicates that their method would not be able to accurately determine the spot covering fraction (or spot temperature if you assumed the spot covering fraction instead) because their method is not sensitive to spot covering fractions of less than 20%, and HAT-P-11's maximum spot covering fraction is around 14% morris2017.

3.4.1 Limitations of Method

For this technique to be very successful, there are a few key factors that must be considered. One is that we need high-precision and high-cadence photometry in order to possibly catch a starspot crossing event. Fortunately, we can achieve very high ($<$ 1 mmag) precision from ground based facilities that have diffuser-assisted imaging available. High-precision transit photometry is also available through current and past space-based missions like *Kepler*, K2, TESS, and CHEOPS cheops, but this technique does require observations of the same starspot in at least two filters to confirm rather than estimate the spot temperature, which those missions do not have. This leads to the last key factor which is target selection limitations. Since we are currently limited to ground-based high-precision photometry, there are only so many known systems with starspot crossing events that are bright enough to be observed from the ground. However, for those objects, there is no guarantee that a starspot crossing event that can be seen from the ground (i.e. a sufficiently large starspot like the big one in the simulated HAT-P-11 light curves) will occur during the observed transit. Additionally, it may be possible to observe the same starspot region with both TESS and CHEOPS, which would open the target list to many more options.

The limitations of this method were shown quite clearly in this paper, as HAT-P-11 is an ideal target for diffuser-assisted ground based observations due to its brightness. HAT-P-11 also has very well characterized stellar surface features and is known to host starspot crossing events in 95% of its *Kepler* transits. Additionally, our LCO MuSCAT3 transits had $<$1 mmag precision in every filter. However, most of the starspots on HAT-P-11 are sized more similarly to the smaller bump in Figure 3.4. As is seen in Figure 3.8, the smaller of the two bumps can only be clearly seen in the binned SDSS g' data. Even with the exquisite precision from the LCO data, it would only be possible to catch a large starspot crossing in multiple filters for HAT-P-11 and likely other targets as well.

3.4.2 Future Work

With the JWST jwst and upcoming Pandora SmallSat quintana2021 missions, there will soon be an influx of transmission spectroscopy done on exoplanet atmospheres around a wide range of host stars. Thus, it is becoming increasingly more important to be able to characterize and model stellar surface features on stars with a wide range of temperatures and rotation periods. In the modeling of starspots and faculae, the temperature of the active region is necessary in order to accurately determine the size of the region. With our introduced method of theoretically determining the contrast of the starspots for a range of spot temperatures, it is possible to determine within 100 K the temperature of the spots with only one transit in at least two filters, assuming there is a starspot crossing event observed during the transit. If there is a persistent starspot that is observed in multiple transits and with different filters, then this method could also be successful in determining the spot temperature, though any observational difference (e.g. weather or seeing shifts during the transit) could influence the observed spot occultation as well (see 3884 for example). In either case, this method is not observationally expensive as only one or two transits for each object is required.

Even with only single band photometry, it would be possible if there are simultaneous spectra taken of the object to measure the spot temperature. This could be done using a combination of modeling the spots using the photometry, either with in-transit spot occultations or out-of-transit photometric modeling (see wisniewski2019 for reference) which provide a simultaneous measurement of the spot covering fraction. With this simultaneous spot covering fraction measurement, then the concurrent spectra can be modelled using a two temperature spectral decomposition framework. This type of light curve modeling combined with spectral decomposition modeling has been done by gosnell2022 on a subgiant star with a large covering fraction of 32%, although their work was done for non-simultaneous photometric and spectroscopic data. However, with a mission like the upcoming Pandora SmallSat mission quintana2021, it will be possible to perform this type of method with simultaneous single-band photometry and near-IR spectra.

3.5 Conclusions

Starspot properties, such as their temperature, are important components to understanding both stellar magnetic dynamo theory and exoplanetary transmission spectroscopy. Historically, starspot temperatures have been measured using spectroscopic techniques that leverage different molecular bands that appear only at certain temperatures, but these methods work best for G and K stars with high starspot covering fractions (see bergyugina2005,morris2019 and references therein). For HAT-P-11 which has a maximum covering fraction of 14% or for

lower temperature stars like M dwarfs, these spectroscopic methods are not ideal. Thus, we have instead leveraged a starspot crossing during a transit to devise a method to measure the spot temperature using high-precision photometry. Using high precision, multi-filter photometry, we have demonstrated the ability to determine the spot temperature to within 100 K if there is a starspot occultation event using a HAT-P-11b transit obtained using the MuSCAT3 instrument on LCO's 2.0-meter FTN telescope. This method can be used for any two filters with different enough contrasts, though SDSS g' and SDSS i' created the largest signal difference with the highest cadence in our work and for our object. Future missions such as Pandora will provide simultaneous photometric and spectroscopic data during transiting events, which will allow for even more measurements of spot temperatures and covering fractions.

3.6   Acknowledgements

Table 3.1: Polynomial Coefficients

Filter	a	b	c	d
SDSS g'	1.846e-10	1.715e-06	-5.339e-03	6.514
SDSS r'	2.932e-11	-6.964e-07	3.568e-03	-4.329
SDSS i'	-2.979e-11	1.357e-07	-1.750e-04	1.003
SDSS z'	-1.426e-11	1.708e-09	2.249e-04	4.526e-01
Zs	-5.947e-11	5.331e-07	-1.878e-03	3.297
TESS	-1.414e-11	-7.307e-08	7.371e-04	-2.964e-01
Kepler	-4.579e-11	1.909e-07	1.298e-04	3.452e-02

3.7 Appendix

3.7.1 Polynomial Fits to Contrast Curves

In addition to calculating the contrast for every spot temperature in every filter as described in Section 3.3, we have fit a polynomial to the contrast values shown in Figure 3.2. For our polynomial fitting, we are interested in the ability to input any spot temperature and calculate a contrast for the chosen filter for HAT-P-11. Thus, we fit the polynomial to our calculated contrast data versus spot temperature rather than wavelength as shown in Figure 3.9. We have shown the contrast versus spot temperature for the following filters as data points and dashed lines: SDSS g' (blue), SDSS r' (magenta), SDSS i' (red), SDSS z' (cyan), TESS (orange), *Kepler* (green), and OAO Zs (black) with the example polynomial fits shown for the SDSS r' and SDSS i' as solid colored lines. All the polynomial fits have been done using third order polynomials of the form given in Equation (2) where x stands for spot temperature, $[a, b, c, d]$ are the polynomial coefficients, and $p(x)$ provides the contrast for that spot temperature. The polynomial coefficients for each filter are given in Table 3.1. These polynomial curves will thus allow for the ability to choose any spot temperature (x) in any of the listed filters and calculate the contrast for a star with the same effective photosphere temperature and surface gravity as HAT-P-11 (T_{eff}= 4800 K and $\log g$= 4.5).

$$p(x) = ax^3 + bx^2 + cx + d \tag{3.2}$$
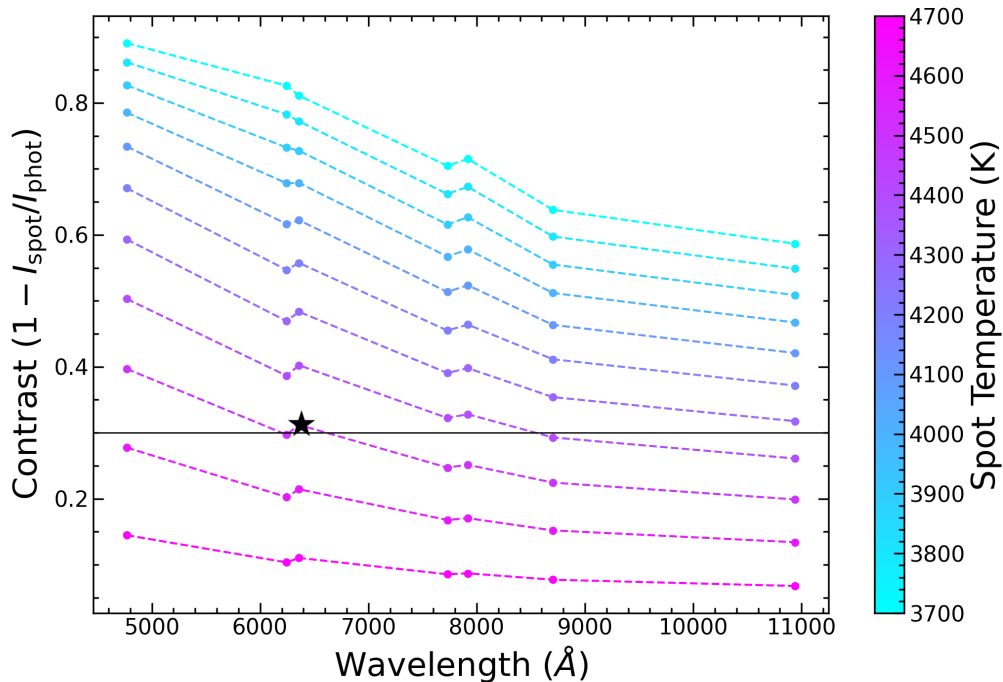
Figure 3.2: Theoretical contrast values for HAT-P-11 assuming $T_{eff} = 4800\ K$ and $\log g = 4.5$. A range of spot temperatures from 3700-4700 K in 100 K steps were used to calculate the contrast of the starspot for a range of filters. The contrast values are plotted as points at the filter's central wavelength, though the contrast applies to the entire bandpass. In order of central wavelength, the filters used were: SDSS g', SDSS r', *Kepler*, SDSS i', TESS, OAO Zs, and SDSS z'. The solid black line at 0.3 corresponds to the area-weighted sunspot contrast assumed in morris2017 for their starspot modeling. The lines are colored by their spot temperature with the coolest spots in cyan. The black star corresponds to the contrast value for magenta spot spectrum shown in Figure 4.13.
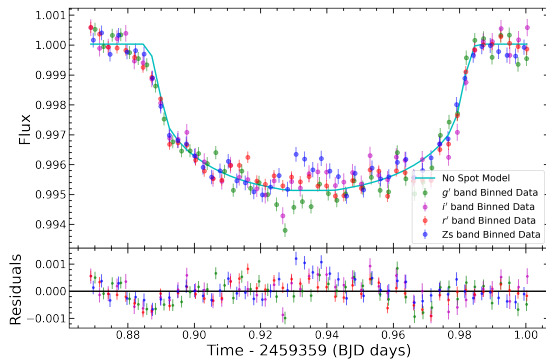
Figure 3.3: Data from LCO MuSCAT3 from HAT-P-11b transit on June 29th, 2021 binned to 200 seconds for SDSS r' (red) and SDSS i' (magenta) and 210 seconds for SDSS g' (green) and Zs (blue) with all filters plotted on top of each other. The bottom panel shows the residuals of the no spot model for that filter minus the binned data points $cyan line here shows example no spot model for SDSSr')$.
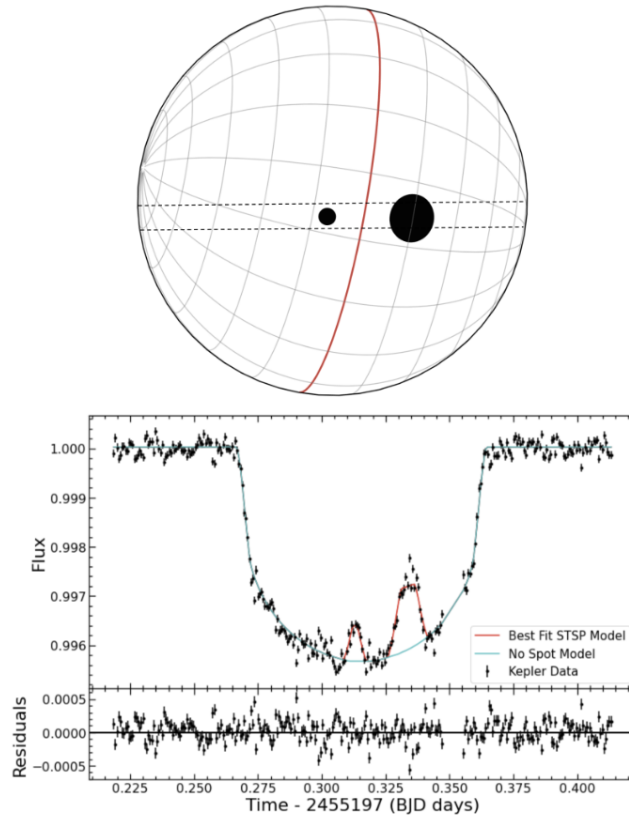
Figure 3.4: **Top:** Plot of the surface of HAT-P-11 with the final spot groups shown as black filled circles along with the red line denoting the equator of the star and with dashed lines denoting the full extent of the transit path for the secondary object (given $\lambda = 106^{+26^\circ}_{-10}$). **Bottom:** Light curve for final STSP fit (red line) along with the no spot model for HAT-P-11 (cyan line) for chosen transit. The residuals (model - data) are shown below the light curve with black points.
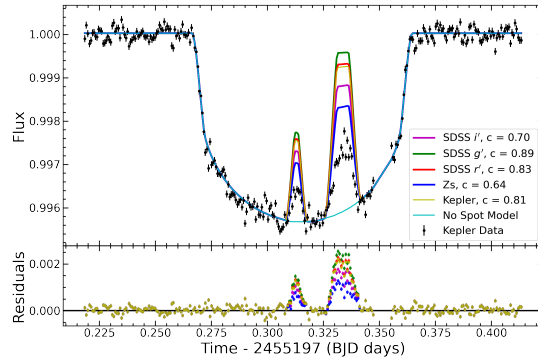
Figure 3.5: Starspot models using theoretical contrast curves assuming spot temperature of 3700 K for SDSS g' (green line), SDSS r' (red line), SDSS i' (magenta line), and Zs (blue line) filters compared to *Kepler* data (black points) and the no spot transit model (cyan line). This spot temperature assumes the spot temperature difference versus photosphere temperature model from herbst2021. This spot temperature produces too dark spots (bumps are too big) to fit the data.
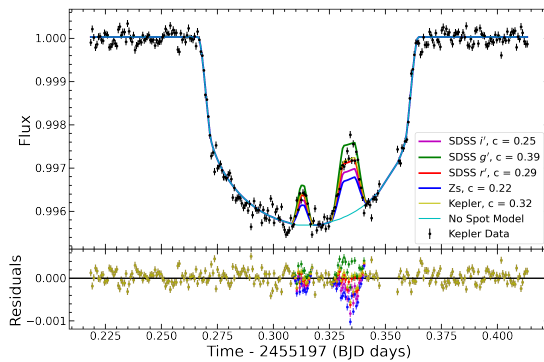
Figure 3.6: Starspot models using theoretical contrast curves assuming spot temperature of 4500 K for SDSS g' (green line), SDSS r' (red line), SDSS i' (magenta line), *Kepler* (yellow line) and Zs (blue line) filters compared to *Kepler* data (black points) and the no spot transit model (cyan line). This spot temperature fits the *Kepler* data best and corresponds to a contrast of 0.31 in the *Kepler* band, similar to the value of 0.3 assumed in morris2017.
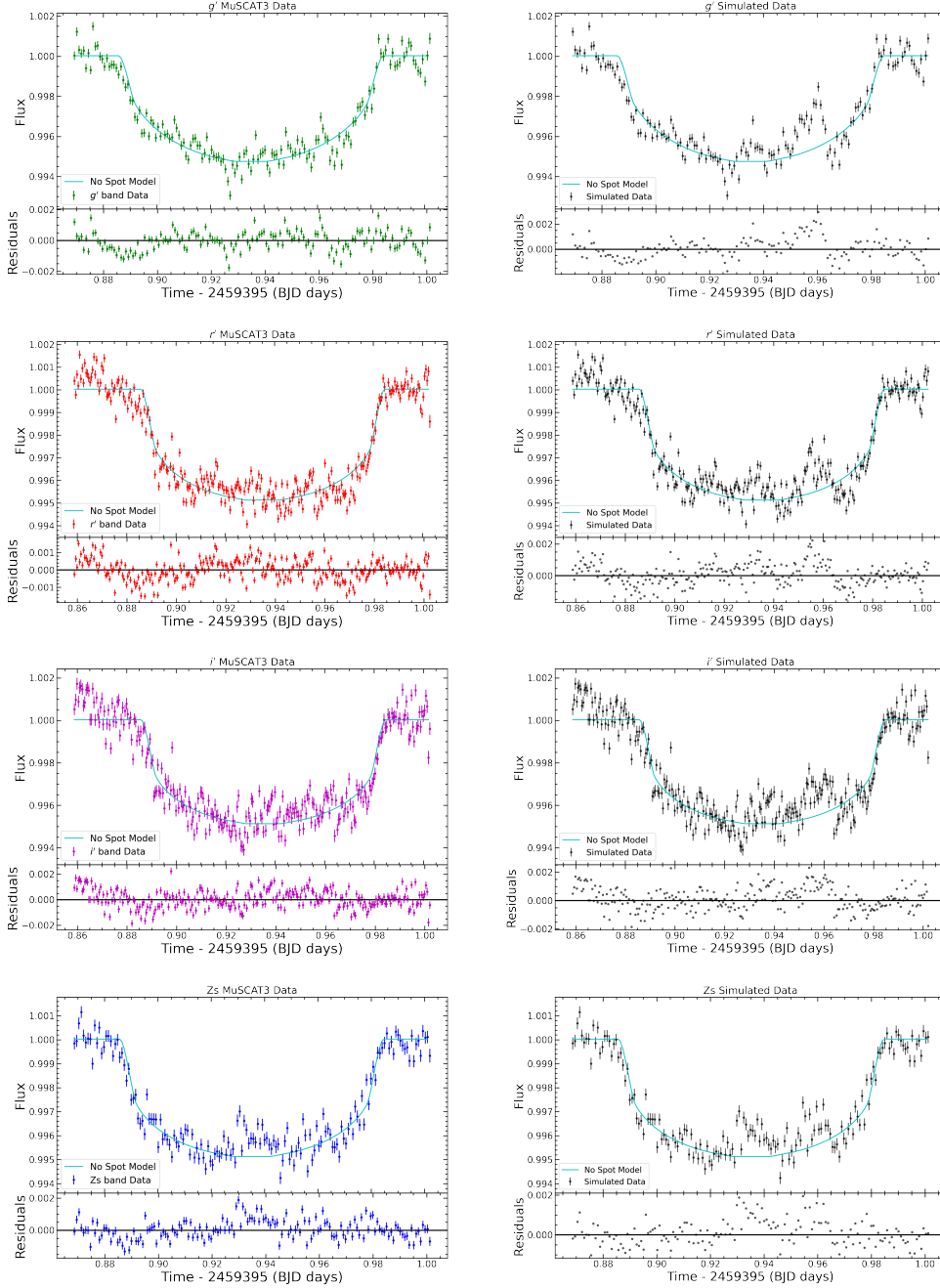
Figure 3.7: **Left:** Data collected by MuSCAT3 instrument for HAT-P-11 b transit obtained on June 29th, 2021. The g' band data are shown in the top panel with a precision of 0.58 mmag with an exposure time of 70 s. The r' band data are shown below the g' with a precision of 0.57 mmag with an exposure time of 40 s. The i' band data are shown next with a precision of 0.62 mmag with an exposure time of 40 s. Lastly, the Zs band data are shown in the bottom panel with a precision of 0.54 mmag with an exposure time of 70 s. **Right:** Simulated light curves of LCO data in g', r', i' and Zs bands from top to bottom panels respectively assuming the star was spotted as in the *Kepler* light curve in Figure 3.4. Black points correspond to simulated data with appropriate error bars. The no spot transit model for each filter is shown as a cyan line with the residuals (no spot model - simulated data) shown as black dots in bottom panel of each figure.
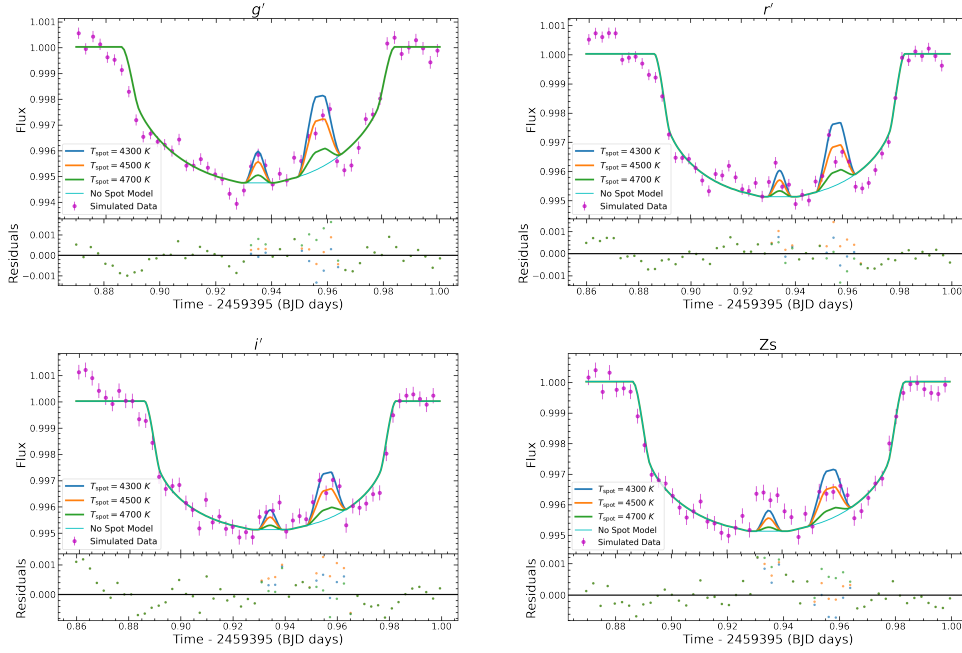
Figure 3.8: Simulated light curves of binned LCO data in g', r', i' and Zs bands (top left, top right, bottom left, and bottom right respectively) compared to three STSP models corresponding to $T_{\text{eff}\,spot} = 4300$ K (blue line), 4500 K (orange line), and 4700 K (green line) with residuals of model - data shown for all three cases in bottom panel. In all cases the χ^2 of the STSP model compared to the simulated data is lowest for $T_{\text{eff}} = 4500$ K, though the two closest spot temperature models (4400 and 4600 K) fit within the $\Delta \chi^2$ of the 4500 K STSP model.
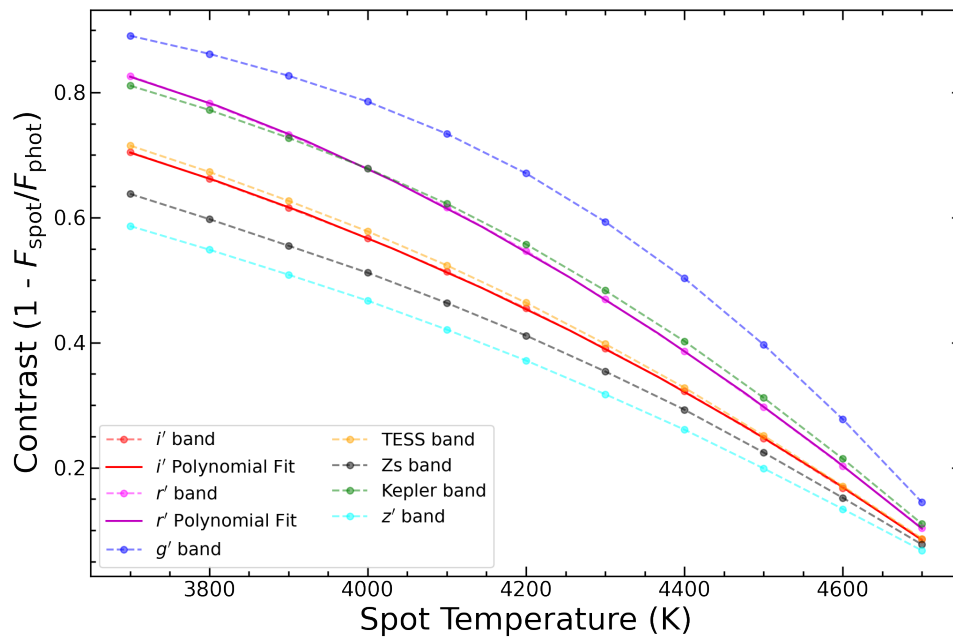
Figure 3.9: Data for calculated HAT-P-11 contrast versus spot temperature for the following filters are shown as data points with dashed lines: SDSS g' (blue), SDSS r' (magenta), SDSS i' (red), SDSS z' (cyan), TESS (orange), *Kepler* (green), and OAO Zs (black). Two polynomial fits are shown for the SDSS r' and SDSS i' as solid colored lines.

Chapter 4

Modeling Surface Features on an M dwarf

This chapter is reproduced from Libby-Roberts, Schutte et al. (2023) accepted on April 11th, 2023.[1] The entire paper is reproduced here, but I led the starspot modeling and analysis sections with the planet characterization lead by the first author Libby-Roberts. I included the entire paper for completeness and so all relevant background information was available.

4.1 Introduction

Giant planets larger than 6 $R_\oplus$ are notably infrequent around FGK-dwarf stars compared to smaller sub-Neptunes and super-Earths [82]. Giant planets orbiting M dwarfs are even rarer with < 15 discovered to date (e.g., [83, 84, 85, 86]). This sparsity was predicted by [87] who postulated the smaller protoplanetary disks should make it near-impossible for cores to accrete and experience runaway growth within the disks' lifetimes. *TESS* [88], however, continues to discover new giant planets orbiting M dwarfs. All previously discovered giant planets orbit early- and mid-M dwarfs with stellar masses > 0.35 $M_\odot$ [89].

TOI-3884b is the first transiting super-Neptune discovered orbiting a M4 Dwarf with a stellar mass of 0.30 $M_\odot$. Its planetary nature was originally validated by [19], who obtained several ground-based transits with ExTrA [90] and LCOGT [91] as well as two radial velocity (RV) points with ESPRESSO [92]. Interestingly, TOI-3884b possesses a persistent signature in every transit indicative of a star spot crossing event. Given the lack of notable out-of-transit variability, [19] suggest the spot is a long-lived pole-spot.

Pole-spots are a common feature on young M dwarfs like TOI-3884. These spots can persist beyond 6-12 months (e.g., [93, 94]). In-transit spot crossing events provide an interesting probe for monitoring spot evolution [95, 96]. As the planet passes over a cooler and darker spot, the amount of flux blocked by the planet decreases yielding a bump in the transit light curve (e.g., [5, 4, 96]. For TOI-3884b, [19] used the duration and wavelength-dependent amplitude of this feature to approximate the spot temperature and area. Assuming a polar location, they also estimated the orbital obliquity concluding that TOI-3884b must be misaligned relative to its star's spin-orbit axis.

The TOI-3884 system is a promising target for future JWST observations. TOI-3884b possesses the highest transmission spectroscopy signal-to-noise ratio per transit for a planet with an equilibrium temperature < 500 K making it a favorable planet for atmospheric

---
[1]https://ui.adsabs.harvard.edu/abs/2023AJ....165..249L/abstract

characterization. With the assured spot crossing, the transit of TOI-3884b may also provide a direct measure of the spot's impact on the atmospheric transmission spectrum of the planet [97].

In this paper, we present an in-depth analysis of the TOI-3884 system. We describe our observations in Section 4.2 which we use to derive updated stellar and planetary parameters in Section 4.3. We perform a detailed analysis of the stellar spots in Section 4.4. Section 4.5 discusses these results, as well as places TOI-3884b in context to the growing M dwarf giant planet population. We conclude in Section 4.6.

4.2 Observations and Data Reduction

4.2.1 TESS

TOI-3884 (TIC 86263325; $T_{mag} = 12.91$; $J_{mag} = 11.13$)[2] was flagged as an object of interest host in the *TESS* Sector 22 (2020 February 19 – 2020 March 17) long cadence (30-minute) data by the TESS Quick Look Pipeline (QLP) [98] during the *Faint-Star Search* [99]. The transit shape was noted to show an unusual shape by the TESS Follow-up Observing Program (TFOP)[3]. TOI-3884 was again observed by *TESS* in Sector 46 (2021 December 04 – 2021 December 30) and Sector 49 (2022 March 01 – 2022 March 25) with 2-minute exposures.

We use the `lightkurve` package [100] to download all three sectors assuming a 'harder' quality flag, removing all NaNs and initial outliers from the Pre-search Data Conditioning Simple Aperture Photometry (PDCSAP) [101, 102]. Folding the 2-minute short cadence light curves in both Sectors 46 and 49 on the expected 4.56 day period for TOI-3884b clearly shows an unusual transit shape (Figure 4.2) – an ingress, a bump that spans half the transit, and then the continuation of a normal transit shape through egress. This bump is also present in Sector 22 though the long 30-minute cadence is too sparse to resolve any structure in-transit.

4.2.2 Ground-Based Transit Photometric Follow-up

We observe seven photometric transits/partial-transits of TOI-3884b using three separate ground-based facilities using Bessell I, SDSS i′, and SDSS r′ filters. We highlight each set of observations below and plot each individual transit, along with the folded TESS transits for Sectors 22, 46, and 49 in Figure 4.2.

---

[2]https://exofop.ipac.caltech.edu
[3]https://tess.mit.edu/followup/
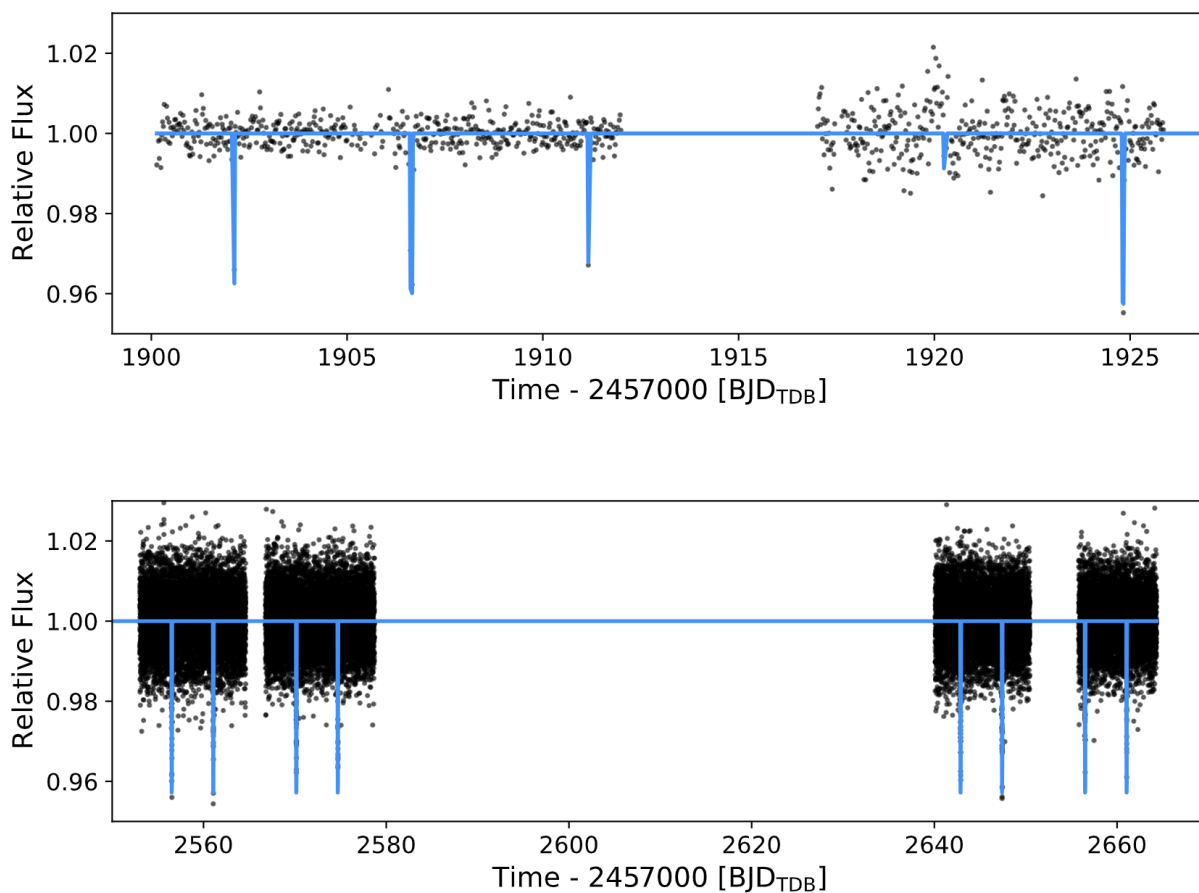
Figure 4.1: **Top:** *TESS* Sector 22 long-cadence light curve with the TOI-3884b transits denoted in blue. Differing transit depths is an artifact of the 30-minute cadence. **Bottom:** Short 2-minute cadence of the *TESS* Sectors 46 and 49 with the transit model in blue. Both sets of light curves use the PDCSAP flux without additional out-of-transit GP detrending required.
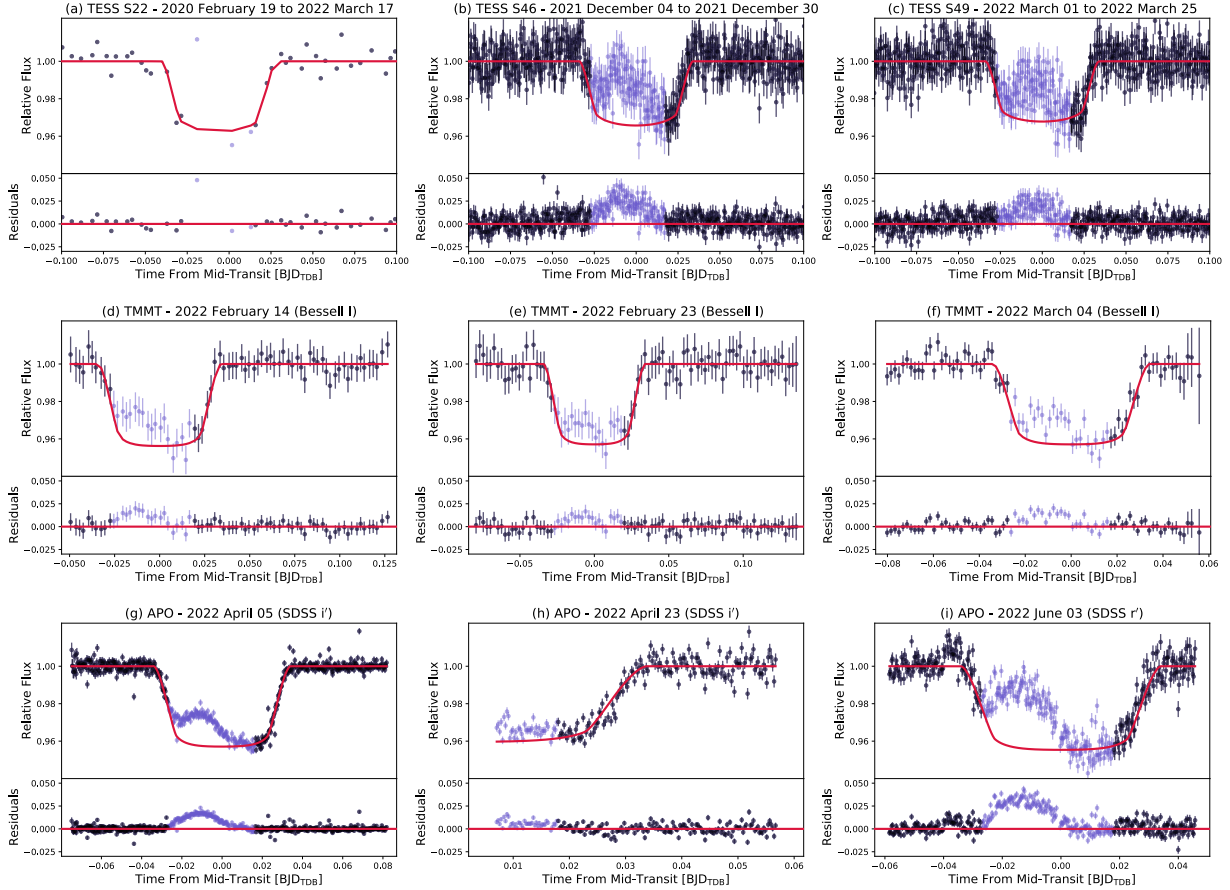
Figure 4.2: Light curves for individual ground-based observations and the phase-folded *TESS* Sectors 22, 46, and 49. Light blue points were masked in order to fit the transit shape during our analysis and the best-fit non-spotted transit model is plotted in red with the appropriate dilution terms included for the *TESS* sectors (0.98, 0.86, 0.84 respectively). Residuals for the respective transit models are plotted in the bottom panel for each light curve.

4.2.3   0.3 m TMMT

We observed three separate transits of TOI-3884b (2022 February 14, 2022 February 23, 2022 March 4 UT) using the 0.3 m Three-hundred MilliMeter Telescope (TMMT) [103] at Las Campanas Observatory in Chile. Each night used the Bessell I filter with 180 second exposures. Every observation included the entire transit though pre- and post-transit baselines did not span the same length of time. Images collected during each night were then reduced following the procedure highlighted in [103].

We perform aperture photometry on the reduced TMMT images using `AstroImageJ` [104]. We assume a photometric aperture radius of 10 pixels (11.9 arcseconds) around the target and 14 reference stars while the median background value was derived from an annulus with inner and outer radii of 15 pixels (17.9 arcseconds) and 25 pixels (29.5 arcseconds) respectively before being subtracted. We divided the target star's flux by the combined flux from the reference stars and derived the flux uncertainties from a combination of stellar, background, and dark current photon noise plus the expected read noise of the instrument. We detrend the light curves by dividing out a linear out-of-transit best-fit model. A similar bump in the transit light curve was present in all three observations.

4.2.4   3.5 m ARC Telescope

We observed two transits of TOI-3884b on 2022 April 05 and 2022 June 03 and a partial transit on 2022 April 23 with the ARC 3.5 m Telescope at the Apache Point Observatory (APO) in New Mexico. For all three nights we used the optical CCD Camera ARCTIC equipped with an engineered diffuser [105]. As discussed in [105], the diffuser enables near photon/scintillation-limited precision light curves by spreading the stellar PSF into a stable top-hat profile without the need to defocus the telescope.

The observations for each night applied the same instrument set-up: quad and fast read-out mode, 4×4 pixel binning, and 20-second exposures. Biases and dome flats were collected either before or after each observing run. ARCTIC does not experience significant dark current for exposures < 60 seconds and was not accounted for in our reduction.

On 2022 April 05 we observed the full transit using the SDSS i′ filter with good weather and photometric skies. We also used the SDSS i′ filter for the 2022 April 23 transit, though poor weather caused us to miss the first half of the transit and led to significant scatter in the data. To check for chromaticity both in the bump and in the overall transit depth, we observed TOI-3884b on 2022 June 03 using the SDSS r′ filter. We experienced non-photometric skies due to dusty conditions.

We reduce each observation with bias subtraction before dividing by a nightly median

combined normalized flat field. Aperture photometry was again applied using `AstroImageJ` assuming an aperture size of 20 pixels (9.1 arcseconds), 5 reference stars, and background annulus of 25 (11.4 arcseconds) and 30 (14.7 arcseconds) pixels for inner and outer radii. Similar to TMMT, we detrend the data by dividing out a linear model calculated from the out-of-transit points. On 2022 June 03, we observed a slight increase in flux prior to transit beyond the linear model which we attributed to a potential micro-flare.

4.2.5   0.6 m RBO

We observed the 2022 June 03 transit ingress using the Bessell I filter with the 0.6 m telescope at the Red Buttes Observatory (RBO) in Wyoming, though weather created significant scatter in the transit. While we opted not to include this transit in the analysis, we observed the same slight increase in flux prior to transit as the 2022 June 03 transit obtained with APO. This confirmed the feature is astrophysical and not instrumental or weather-related.

4.2.6   NESSI High Contrast Imaging

We exclude potential background sources that may impact the overall transit signal (depth or shape) using the NN-EXPLORE Exoplanet Stellar Speckle Imager (NESSI) [106] on the WIYN 3.5 m telescope at Kitt Peak National Observatory (KPNO) in Arizona[4]. We took a 9-minute sequence of 40 ms exposures using NESSI's z' filter on 2022 April 18. These images were then combined and processed following the methods highlighted in [107].

We plot the final contrast curve and speckle image in Figure 4.3. We detect no nearby sources with a $\Delta z'$ magnitude brighter than 3.8 from 0.2 out to 0.8 arcseconds and magnitudes brighter than 5 from 0.8 out to 1.2 arcseconds. We compliment this with archival Gaia DR3 Data [108] which finds no nearby sources within 20 arcseconds. Gaia also assigns TOI-3884 a Renormalized Unit Weight Error (RUWE) equal to 1.25 which is consistent with a single star [109, 110]. TOI-3884 is a single star in a fairly sparse region of the night sky.

4.2.7   HPF Radial Velocity Follow-Up

We performed an intensive RV follow-up of TOI-3884 using Habitable-zone Planet Finder [111, 112] starting on 2021 December 01. HPF is a high resolution (R ∼55,000) near-infrared (810 − 1280 nm), fiber-fed [113], stabilized [114] precision RV spectrograph, on the 10 m Hobby-Eberly Telescope in Texas [115]. Over the next 5 months, we observed TOI-3884 27

---

[4]The WIYN Observatory is a joint facility of the NSF's National Optical-Infrared Astronomy Research Laboratory, Indiana University, the University of Wisconsin-Madison, Pennsylvania State University, the University of Missouri, the University of California-Irvine, and Purdue University.
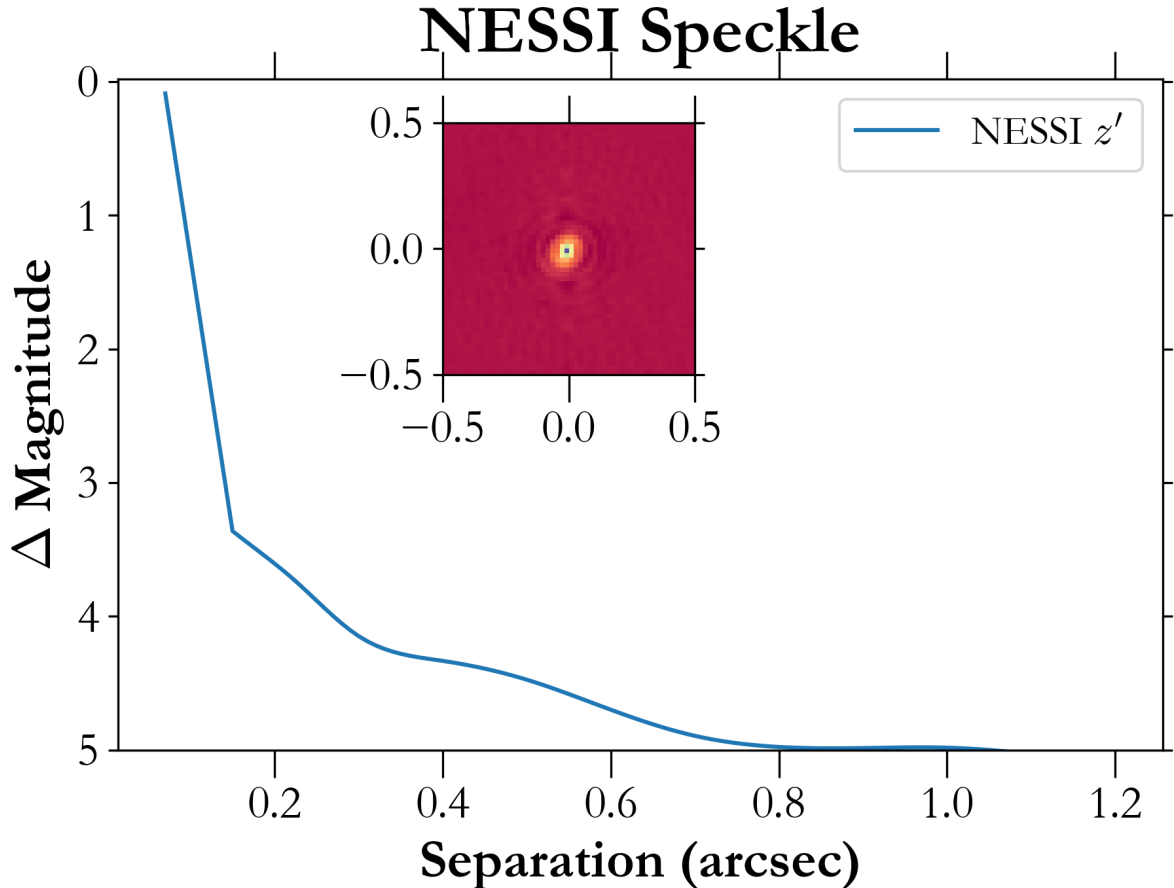
Figure 4.3: NESSI 5σ contrast curve of TOI-3884 with the z' filter. The inserted image is the final speckle image which shows no nearby sources with Δmag > 3.5 outside 0.2 arcsec

nights with each night obtaining two 945-second exposure measurements. Each spectrum was analyzed using the `HxRGproc` package which corrects for bias, non-linearities, cosmic rays, and then calculates the flux and variance of the individual spectra as described in [116]. We use `barycorrpy` [117] to perform the barycentric correction on the individual spectra, which is the Python implementation of the algorithms from [118]. A wavelength solution was created by interpolating the wavelength over all other exposures in the same night of each observation, which was then applied to the respective TOI-3884 spectra.

We removed all nights (8 total) which possessed unbinned S/N ratios less than 50% of the expected S/N of 74 at 1.04 μm calculated from the HPF Exposure Time Calculator[5]. These S/N ratios ranged between 21 to 31. An inspection of these low S/N observations determined they were all obtained during less than optimal sky conditions (variable seeing

---

[5]https://psuastro.github.io/HPF/Exposure-Times

> 2 arcseconds, background i′-band magnitude was brighter than 16.5, transparency was <
75% and/or bad weather or clouds were noted in the night logs). Every other observation
possessed a S/N > 43 and met our required observing conditions for transparency, seeing,
and good weather conditions. We also removed the spectra from 2022 April 5 as these were
observed during the transit spanning the large bump. As the planet is crossing an active
region of the star, this may introduce potential contamination in the RV signal. This left 36
unbinned spectra taken over the course of 18 nights (Figures 4.4 and 4.5).

We applied a template-matching method [119] using the SERVAL pipeline [120] modified
for HPF [121]. A master template was created by combining all spectra and masking tellurics
and sky-emission lines. This template was then shifted to match each individual spectrum by
minimizing the χ^2 statistic before converting this shift into velocity space. We binned the
two nightly individual RVs reported from SERVAL using a weighted-average based on their
respective S/N ratios. The final binned RVs used for our analysis are listed in Table 4.2.7
and are plotted in Figure 4.5.
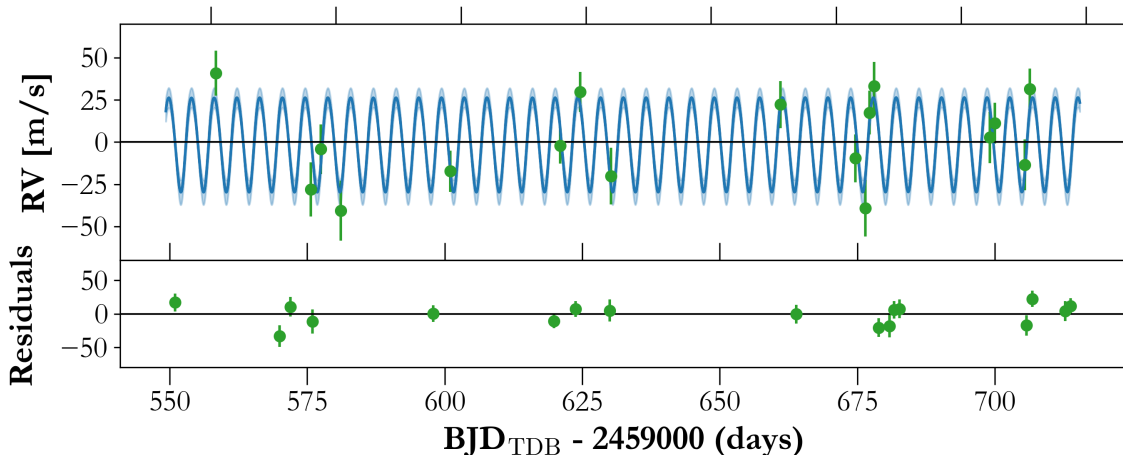
Figure 4.4: The full HPF RV time series with the best-fit model plotted in blue,
with the 1-σ quantile included as a lighter shade.

4.3 Analysis

4.3.1 Stellar Properties

We derived the spectroscopic stellar parameters: effective temperature (T_{eff}), metallicity
([Fe/H]), and log g of TOI-3884 by applying the template matching methodology on the HPF
spectra as outlined in [121]. Using the `HPF-SpecMatch` package [121], we apply the spectral
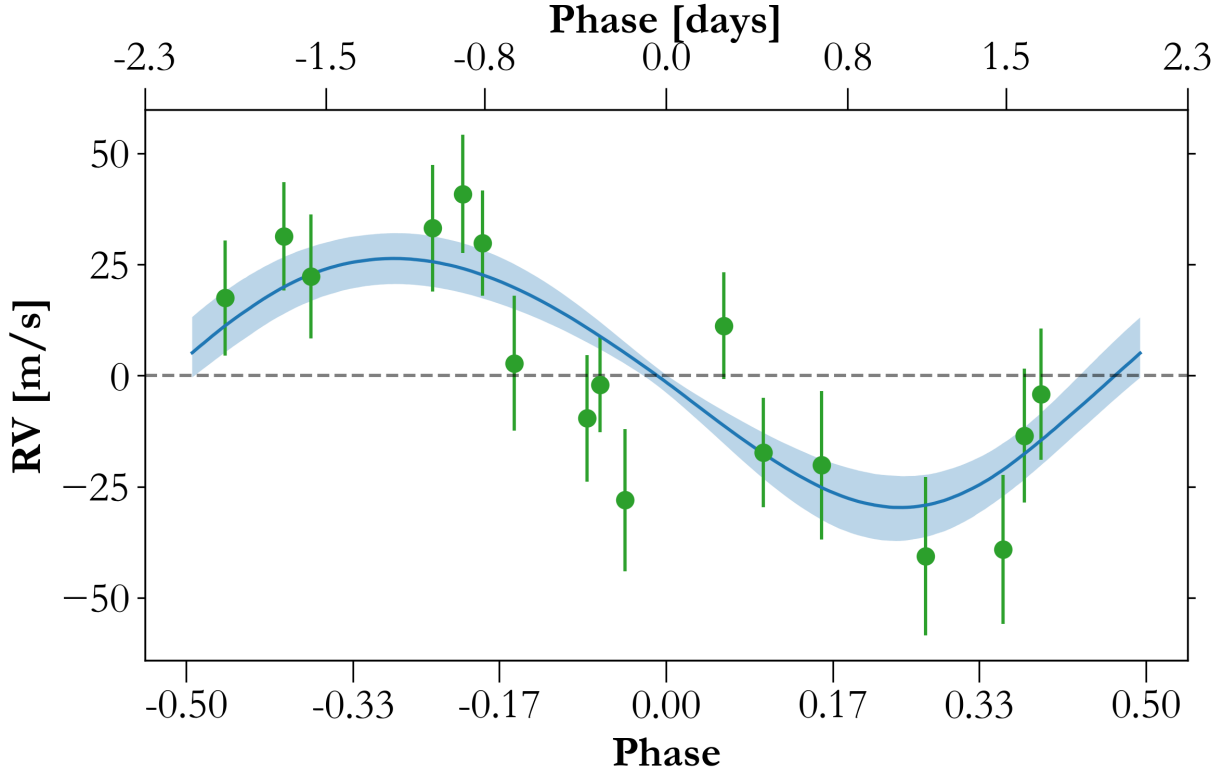
Figure 4.5: The HPF RVs phased to the best-fit period of TOI-3884b. Best-fit model and the 1-σ quantile are plotted in blue. Mid-transit occurs at phase 0.

matching technique to the HPF Order 5 spectra (853 − 864 nm) which has little to no telluric contamination. We list the spectroscopically derived stellar parameters for TOI-3884 from this analysis in Table 4.3.1.

With the `isochrones` package [122], we create an SED fit using the combination of the derived stellar spectroscopic values, the g, r, i, z, and y magnitudes reported from Pan-STARRS1 [123][124], the W1, W2, and W3 WISE-band magnitudes [125], the J, H, and K magnitudes reported by 2MASS [126], and the parallax from Gaia DR3 [108]. We utilize Gaussian priors for all parameters except for a flat prior on the A_V extinction and flat-log age prior up to 2 Gyr (see Section 4.3.1). We utilize the relations in [127], calculated for the Gaia reported distance of 43 pc, to place an upper A_V extinction limit of 0.1. We determine a stellar mass and radius of 0.298 ± 0.018 $M_\odot$ and 0.302 ± 0.012 $R_\oplus$ respectively (stellar density: 15.26 ± 2.04 g/cm^3) for TOI-3884. We verify these values by repeating the same fits using the `ExoFASTv2` package [128], deriving masses and radii within 1σ. We verify this stellar density using the high-precision 2022 April 05 APO transit where we obtain a best-fit density of 15.43 ± 0.39 g/cm^3 (assuming a circular orbit).

Table 4.1: The ∼30 minute binned HPF RVs of TOI-3884. Low S/N points removed from the analysis are not included.

BJD_{TDB} (d)	RV (m/s)	σ (m/s)
2459550.99616	25	13
2459569.95174	-44	16
2459571.94743	-20	15
2459575.93822	-56	18
2459597.88347	-33	12
2459619.82335	-18	11
2459623.80447	14	12
2459629.97493	-36	17
2459663.88252	7	14
2459678.84026	-25	14
2459680.83590	-55	17
2459681.65219	2	13
2459682.64507	18	14
2459705.76008	-13	15
2459706.76349	-4	12
2459712.74903	-29	15
2459713.74422	16	12

Using ESPRESSO, [19] suggests that TOI-3884 is a slowly rotating star with a slow $v \sin i$ of 1.1 km/s. They note this slow rotation suggests an inactive star – in contrast with the large spot crossing event. We use our HPF spectra in an attempt to verify the slow rotator scenario by constraining the rotational broadening of TOI-3884 using two separate methods. First during the spectral-matching process, HPF-SpecMatch performs an optimization for the optimal rotational broadening [129]. This results in a $v \sin i = 3.6 \pm 0.9$ km/s. Second, we compare the widths of CCFs of TOI-3884 to the CCF widths of artificially broadened slowly rotating reference star of a similar spectral type. The HPF-SpecMatch analysis highlights Ross 128 as an excellent spectral match to TOI-3884b with a $T_{eff} = 3192 \pm 60$ K [130], which matches well with the effective temperature of TOI-3884 of $T_{eff} = 3180 \pm 80$ K (Table 4.3.1). Further, [131] demonstrate that Ross 128 is an inactive slowly rotating M dwarf with a long rotation period of > 100 days, suggesting minimal rotational broadening.

Figure 4.6 compares the CCFs of TOI-3884 to the CCFs of Ross 128 from 6 HPF orders clean of tellurics, suggesting that a $v \sin i > 3$km/s is warranted, and we derive a $v \sin i = 3.2 \pm 0.9$ km/s estimate from the average and the standard deviation values from
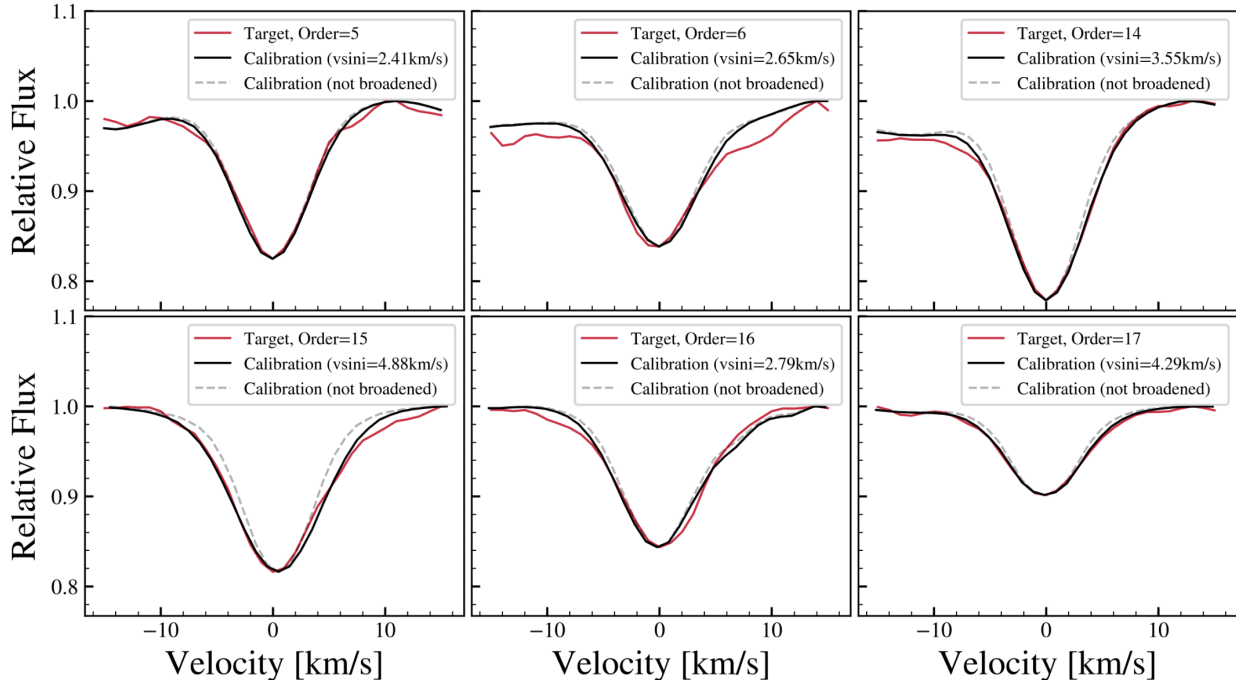
Figure 4.6: Comparing the width of the CCFs of TOI-3884 (red curves) in 6 different orders in HPF in 6 different panels to the CCFs of slowly rotating calibration star, Ross 128. The grey-dashed lines show the unbroadened calibration star, and the black lines show the calibration star artificially broadened to the best fit value. The TOI-3884 spectra show evidence for rotational broadening.

the 6 HPF orders, respectively. We note that in trying to use other slowly rotating stars of similar spectral types results in similar $v\sin i$ values. We elect to formally adapt the $v\sin i$ value derived from `HPF-SpecMatch`, as through its χ^2 minimization process of the full spectra it can better account for differences in normalization offsets that could lead to differences in the CCFs. We were unsuccessful to resolve the slower 1.1 km/s $v\sin i$ as originally published for this star.

The relatively rapid $v\sin i$ from this work suggests TOI-3884 should be active and relatively young (<1 Gyr) [132]. We support this conclusion with the LAMOST spectra which covers Hα. LAMOST reports an Hα equivalent width (EW) of -3.86 $\pm$ 0.02 Å in emission. From Equation 1 in [133], an inactive star with TOI-3884's properties should have an Hα EW of 0.18 Å in absorption. *TESS* observes three large flaring events in the two short cadence sectors, and the HPF spectra also show clear Ca IR triplet (Ca IRT) excess in emission.

We apply `pyHammer` [134] to the archival Large Sky Area Multi-Object Fiber Spectroscopic Telescope [135, 136] spectra assuming the metallicity derived from the HPF spectra. Using a template-matching routine of empirical M dwarf spectra, we determine the best-fit spectral

type to be either an M4 or M5 dwarf. We adopt M4 as the spectral type for this work.

Significant spot coverage can affect the measured photospheric temperature of the star and influence the SED derived stellar mass/radius. However, we detect no significant deviation from a single star SED fit to the observed magnitudes using `ExoFASTv2`. Moreover, we calculate a spot covering fraction of 15% with a spot temperature of 2900 K will impact the actually stellar temperature by 50–100 K for TOI-3884. This is within the T_{eff} uncertainty reported by `HPF-SpecMatch`. Therefore, the derived stellar parameters in Table 4.3.1 are minimally affected by the large spot (see Section 4.4).

4.3.2   Joint Analysis of Transit and Radial Velocity Observations

We perform a joint-analysis of the transit and radial velocity (RV) observations to measure TOI-3884b's mass and radius. However, the lack of a pristine non-spot crossing transit light curve of TOI-3884b creates a challenge for transit analysis. We create an individualized starspot-mask based on visual inspection to each ground-based transit and to the three folded *TESS* sectors. We then fit a transit model to the unmasked points. We calculate a χ_r^2 of the residuals along with a by-eye examination. Points that still demonstrate bump-structure are masked and we repeat the procedure until we minimized the χ_r^2. Masked duration and location vary slightly between data sets though all fell between 39 minutes prior to mid-transit (T_0) to 25 minutes post T_0; i.e, ∼60% of the transit duration. Figure 4.2 plots the ground-based and folded *TESS* light curves with the masked points denoted in blue.

We perform a joint fit with `exoplanet` [139] using both the masked *TESS* and ground-based transits and the HPF RVs. We fit for a single transit ephemeris, period, impact parameter, a/R_s, and transit depth using the combination of the three masked *TESS* sectors, three TMMT transits, and three APO observations. We include a dilution term to the transit depth for each of the three *TESS* sectors fixed on the ARCTIC SDSS i′ transit. `exoplanet` uses the built-in `starry` [140] package to model the quadratic limb darkening parameters. As each instrument uses a different broadband filter, we fit for quadratic limb darkening terms specific to the various wavelength coverage (*TESS* bandpass, Bessell I, SDSS i′, and SDSS r′). Last, we included a jitter term added in quadrature to the flux errors and a flux offset to each transit observation. Neither the *TESS* out-of-transit baseline (PDCSAP) nor the ground-based observations required additional detrending. We plot our best-fit transit model in red for each transit in Figure 4.2.

We assume a Keplerian model for the RVs allowing eccentricity and the argument of periastron (ω) to float as well as the RV semi-amplitude. Similar to the photometric transits, we include a jitter and RV offset terms as well as a general trend line. Including a GP had no effect on the RV results thus do not include an activity dependent GP for the RV orbit.

Table 4.2: Summary of stellar parameters for TOI-3884.

Parameter	Description	Value	Reference
	Main identifiers:		
TOI	TESS Object of Interest	3884	TESS mission
TIC	TESS Input Catalogue	86263325	Stassun[137]
2MASS	$\cdots$	J12061746+1230249	2MASS[126]
Gaia DR3	$\cdots$	3919169687804622336	Gaia DR3[108]
	Equatorial Coordinates, Proper Motion and Spectral Type:		
α_{J2016}	Right Ascension (RA)	181.571808	Gaia DR3[108]
δ_{J2016}	Declination (Dec)	+12.507030	Gaia DR3[108]
μ_α	Proper motion (RA, mas/yr)	-186.042409	Gaia DR3[108]
μ_δ	Proper motion (Dec, mas/yr)	26.387835	Gaia DR3[108]
d	Distance in pc	43.1	Gaia DR3[108]
$A_{V,max}$	Maximum visual extinction	0.04	Green[127],
	Optical and near-infrared magnitudes:		
B	Johnson B mag	17.46 ± 0.23	APASS [138]
V	Johnson V mag	15.74 ± 0.01	APASS [138]
g'	Sloan g' mag	16.62 ± 0.09	Pan-STARRS1[124]
r'	Sloan r' mag	15.17 ± 0.06	Pan-STARRS1[124]
i'	Sloan i' mag	13.58 ± 0.06	Pan-STARRS1[124]
T	TESS magnitude	10.792	Stassun[137]
J	J mag	11.13 ± 0.02	2MASS[126]
H	H mag	10.55 ± 0.02	2MASS[126]
K_s	K_s mag	10.24 ± 0.02	2MASS[126]
$W1$	WISE1 mag	10.16 ± 0.02	WISE[125]
$W2$	WISE2 mag	9.99 ± 0.02	WISE[125]
$W3$	WISE3 mag	9.76 ± 0.05	WISE[125]
	`SpecMatch` Spectroscopic Parameters:		
T_{eff}	Effective temperature in K	3180 ± 88	This work
[Fe/H]	Metallicity in dex	0.04 ± 0.12	This work
$\log(g)$	Surface gravity in cgs units	4.97 ± 0.05	This work
	Model-Dependent Stellar SED and Isochrone Fit Parameters:		
T_{eff}	Effective temperature in K	3270 ± 46	This work
[Fe/H]	Metallicity in dex	0.16 ± 0.04	This work
$\log(g)$	Surface gravity in cgs units	4.95 ± 0.02	This work
M_s	Mass in $M_\odot$	0.298 ± 0.018	This work
R_s	Radius in $R_\odot$	0.302 ± 0.012	This work
L_s	Luminosity in $L_\odot$	$\pm$	This work
ρ_s	Density in g/cm^3	15.26 ± 2.04	This work
Age	Age in Gyrs	<1 Gyr	This work
A_v	Visual extinction in mag	$\pm$	This work
	Other Stellar Parameters:		
$v \sin i_s$	Rotational velocity in km/s	3.59 ± 0.92	This work
$P_{rot}(i_s = 90°)$	Non-tilted maximum rotational period in days	4.22 ± 1.09	This work
ΔRV	"Absolute" radial velocity in km/s	3.16 ± 2.89	Gaia DR3[108]
U, V, W	Galactic velocities in km/s	$\pm$	This work

84

Table 4.3: Derived Parameters for TOI-3884b

Parameter	Units	Value[a]
Main identifiers:		
Orbital Period . . . . P (days)		4.5445828 ± 0.0000098
Eccentricity . . . . e		$0.06^{+0.06}_{-0.04}$
Argument of Periastron . . . ω (radians) .		$-1.96^{+4.28}_{-0.04}$
Semi-amplitude Velocity . . K ()		$28.03^{+6.06}_{-6.23}$
RV Trend . . . . dv/dt (yr^{-1})		$0.58^{+4.78}_{-4.92}$
RV Jitter . . . . σ_{HPF} ()		$7.86^{+5.68}_{-5.11}$
Transit Parameters:		
Transit Midpoint . . . . T_C (BJD$_{\mathrm{TDB}}$)		$2459556.51669 \pm 0.00025$
Scaled Radius . . . . R_p/R_s		0.197 ± 0.002
Scaled Semi-major Axis . . . a/R_s		$25.90^{+0.96}_{-0.71}$
Orbital Inclination . . . . i (degrees) . . .		$89.81^{+0.13}_{-0.18}$
Impact Parameter . . . . b		$0.089^{+0.082}_{-0.061}$
Transit Duration . . . . T_{14} (days) . . .		$0.0666^{+0.0019}_{-0.0024}$
Dilution[b] . . . . $D_{\mathrm{TESS\ S22}}$ . . .		0.98 ± 0.12
	$D_{\mathrm{TESS\ S46}}$ . . .	0.86 ± 0.03
	$D_{\mathrm{TESS\ S49}}$ . . .	0.84 ± 0.03
Planetary Parameters:		
Mass . . . . M_p (M$_\oplus$)		$32.59^{+7.31}_{-7.38}$
Radius . . . . R_p (R$_\oplus$)		6.43 ± 0.20
Density . . . . ρ_p ()		$0.67^{+0.18}_{-0.16}$
Semi-major Axis . . . . a (AU)		0.0361 ± 0.0008
Planetary Insolation	S (S$_\oplus$)	6.29 ± 0.84
Equilibrium Temperature[c]	T_{eq} (K)	441 ± 15

[a] The reported values refer to the 16-50-84% percentile of the posteriors. [b] Dilution due to presence of background stars in TESS aperture, not accounted for. [c] We assume the planet to be a black body with zero albedo and perfect energy redistribution to estimate the equilibrium temperature.

We determine TOI-3884b is a super-Neptune with a mass of $32.59^{+7.31}_{-7.38}$ M$_\oplus$ and radius of 6.43 ± 0.20 R$_\oplus$. Figure 4.5 plots the best-fit RV model along with the 1σ contours. We report the best-fit properties from this joint analysis as well as the final planetary properties for TOI-3884b in Table 4.3.2. We note that the derived mass of TOI-3884b is based on the model's assumption that the planet is the main source of the RV variation. Periodograms of the Ca IRT, differential line widths, and chromatic index show no peaks with False Alarm Probabilities $< 10\%$ at the planet's period (nor any other period) indicating that the RV signal is not dominated by stellar activity.

4.4 Starspot Analysis

We now focus on analyzing the ubiquitous spot feature that is present in all the transit light curves shown in Figure 4.2. In-transit flux increases like this one are commonly observed in planetary transits, when the planet passes in front of a localized region of reduced flux on the surface of the star (i.e. a starspot) [141, 95, 4, 96]. Precise knowledge of the planet's orbital properties in combination with the stellar rotation and tilt can provide specific positional information about the spots in the path of the planet as shown in [4, 96]. Conversely, observations of multiple in-transit spot occultations combined with inferences about the spot properties can provide information about the obliquity of the planet, as found in [95]. It is important to note that while we refer to the spots as "spots" what we are most likely modeling are entire spot complexes.

TOI-3884 shows a prominent star spot crossing feature in every high cadence transit between December 2021 and June 2022, and a single point flux increase in-transit in the long-cadence *TESS* light curve from Spring 2020. While spot occultations are often detected in multiple, different transits of the same star, TOI-3884 is unique in that the feature persists at the same orbital phase in the first half of the transit for at least two years. The similarity of the amplitude, duration, and shape of the features combined with its persistence suggests that we are observing the same long-lived spot in all the light curves.

There is a very limited parameter space of stellar rotation and stellar inclination that would result in the same spot being detected at the same orbital phase over the 6-month duration of the observations, given the well-defined orbital period of the planet. If the star is spinning upright (i.e. the stellar inclination is 0°), the persistent spot could only occur if the star was rotating so slowly that the spot appeared fixed in place (which is incredibly unlikely over two years of monitoring), or if the orbital period of the planet was an exact integer multiple of the star's rotation period so that each time the planet transited, a spot feature was back in the same location relative to the observer. The only other scenario which would result in the fixed phase of the star spot feature is one in which the star is tilted away from the line of sight and the large persistent spot is fixed at or near the pole so that it doesn't move relative to the observer even as the star rotates. Based on the measured $v \sin i$, we rule-out the slow rotating scenario. However, we explore the other two possibilities: i) a non-tilted star with synchronous rotation and ii) a tilted star system with a non-zero obliquity.

4.4.1 Starspot Model of a Non-Tilted Star with Synchronous Rotation

We apply the program STarSPot (STSP) [4, 96] to the high-precision 2022 April 05 APO observation with the procedure outlined in [96]. STSP is specifically designed to model the light curves of transiting systems in which star spots and/or faculae create localized surface brightness variations on the host star. Using an affine-invariant Markov Chain Monte Carlo (MCMC) [4] optimizer, a single run of STSP samples different radii (R_{spot}/R_s), latitudes, and longitudes (θ and ϕ respectively) for every spot, but applies a fixed spot contrast (defined by its temperature and the filter of the observed transit) in order to break the known degeneracies between these properties.

For TOI-3884, we assume a photospheric temperature of 3200 K derived from the HPF spectroscopic parameters and perform STSP runs with the following set of spot temperatures: 2600, 2700, 2800, 2900, 3000, and 3100 K. We calculate the contrasts defined by these temperatures by first interpolating PHOENIX synthetic [142] spectra at both the stellar and spot temperatures. We then integrate over the specific filter response curve of the observed light curve and sum the integrated flux in that filter. Finally, we calculate the contrast for each spot temperature by dividing the integrated spot flux by the integrated photospheric flux (Schutte et al. In Prep).

We first consider the star-planet orientation in which the spin-axis of the star is in the plane of the sky and aligned with the orbital axis of the planet. In this case, the measured $v \sin i$ provides a rotation period of $P_{rot} = 4.22 \pm 1.09$ d, which is consistent with the orbital period ($P_{orb} = 4.54$ d). Adopting a rotation period for the star of $P_{rot} = 4.54$ d that is synchronous with the orbital period and applying the STSP program to the APO i$'$ band transit, we quickly find that a single circular starspot is insufficient to describe the structure of the feature, but a three spot model, with one large spot surrounded by two smaller spots produces the lowest χ^2, regardless of spot contrast. Even after forcing the model to have two medium-sized spots in the place of the large central spot, the optimization preferred one large pole-spot combined with the two smaller nearby spots.

The best-fit three spot model is shown in Figure 4.7, consisting of one large central spot ($R_{spot}/R_s = 0.44$) surrounded by two smaller spots ($R_{spot}/R_s = 0.10$ and 0.07 respectively). This model has a reduced χ^2 of 2.14 and corresponds to a spot temperature of 2900 K (contrast = 0.5). In comparison, the best fit one and two-spot models have reduced χ^2 values of 2.25 and 2.16 respectively. If we compare the AIC$_c$ [143] values between the one, two, and three spot models (-9.24, -6.12, and -2.86 respectively), the AIC$_c$ favors the one-spot model as it has the least amount of fitting parameters. It is important to note that both the one and two-spot models do not fit the data points as well by eye (the one spot model is

shown in Figure 4.7). Therefore, even though the AIC_c favors the simplest one spot model, the χ^2 statistic prefers the three-spot model. Additionally, the spot feature is asymmetric, which is hard to fit with fixed circles as is required by STSP, but if we instead have two spots close together, this can replicate an asymmetric feature, which further adds to the three spot model being the best-fit model. Spot temperatures of 2700 and 2800 K produce equally good solutions (reduced χ^2 values of 2.19 and 2.17 respectively which fall within $\sigma_{\chi^2} = 34$) with similar spot configurations. While the reduced χ^2 values are larger than one, the data are ground-based data with likely underestimated error bars. Hotter spot temperatures (3000 and 3100 K) cannot reproduce the amplitude of the feature and are therefore not possible solutions regardless of the spot configuration. The coolest spot temperature of 2600 K produces a similar spot configuration, but the reduced χ^2 falls just outside of the above variance. Given the discrete 100 K sampling of our models, we find the temperature of the large spot to be between 2700 to 2900 K, with a preference for the hotter 2900 K spot. From these fits we constrain the radius of the large spot to be $\text{R}_{\text{spot}}/\text{R}_s = 0.44 \pm 0.08$.

This scenario produces a very large (radius of $\sim 44\%$ the star's radius) star spot which will produce significant photometric out of transit variability of $> 1\%$ if that is the only large feature on the star. Interestingly, we do not detect any clear photometric modulations in the two short-cadence TESS sectors nor in the publicly available ground-based monitoring with Zwicky Transient Facility (ZTF) [144], All-Sky Automated Survey for Supernovae (ASAS-SN)[145], and the Asteroid Terrestrial-impact Last Alert System (ATLAS) [146]. Figure 4.8 shows *TESS* Sector 46 data as an example with Sector 49 showing the same pattern. To explore this scenario fully, we model the full light curve for both *TESS* Sector 46 and 49 with the in-transit star spots fixed but with an additional three spots allowed to vary. We found that in order to decrease the out of transit variability enough to be less than the noise level ($< 0.5\%$) of the *TESS* light curves, there must be additional spots such that as the star rotates there is always a near equal fraction of spotted area (20%) rotating out of view as is rotating into view. Thus, it is possible the photometric spot modulation of TOI-3884 is simply hidden within the noise assuming the spots are configured such that they are uniformly spread across the surface of the star and cover a large fraction of the star.

This leads to the concern that the RV-observed 4.56 d signal is partially due to the stellar rotation and not the planet. However, none of the HPF activity indicators show any periodic signal which would be characteristic for large spots [94].

While observations cannot formally exclude this scenario, the requirements are contrived: TOI-3884 must have a rotation exactly equal to its planet, possess a spotted surface such that the photometric variability is $< 0.5\%$ over the two *TESS* sectors, maintain the same starspot with very little evolution across in the transit chord while keeping the rest of the

transit chord nearly spot-free. We therefore disfavor this hypothesis.

4.4.2 Model of Tilted Star System with Non-Zero Obliquity

Tilting the star such that the spot does not rotate in and out of view would minimize the out-of-transit variability [147]. In this scenario, TOI-3884's large spot must be located on or near the pole of the star with the star's spin axis inclined (i_s) such that the pole of the star is pointed towards the observer. In order for the spot feature to occur at the same phase in the first half of the transit, the spin axis of the star and the planet's orbital axis must be misaligned (i.e. $\lambda \neq 0$) . Because STSP assumes the planet's position and the star's tilt are well known, it is not designed to derive the optimal stellar inclination and λ. However, the fixed phase of the spot feature allows us to constrain the tilt of the star's spin axis and λ. For example, if the pole of the star is pointed exactly towards the observer (stellar inclination of $0°$), the bump would occur in exactly the middle of the transit regardless of λ. Conversely, a tilt that is too close to the plane of the sky (i.e. inclination $> 60°$) produce spot crossings during ingress of the transit. Thus, we first performed a comprehensive search of every stellar inclination value from $60°$ down to exactly pole on in increments of $5°$. From our search, we found that the only possible if i_s was $25° \pm 5°$. After determining the best stellar inclination for the star, we then performed a series of simulations which varied λ from $0°$ to $180°$ in increments of $10°$. From our search, we determined that $\lambda = 75° \pm 10°$ provided the best fit to the APO SDSS i′ light curve. It is important to note the provided uncertainties were derived from an exploration of the possible stellar inclinations that fit the data, and then, the uncertainties for λ assume the stellar inclination is constant. Since these parameters are actually entwined, a more formal determination of the error bars is left to future work.

Once we determined the stellar spin axis and λ for the misaligned scenario, we modeled the star spots in the same way as before with STSP where the radii and locations of the spots are allowed to vary. For this scenario, we assume the same number of spots and spot temperature as found for the best-fit aligned model (three spots with temperatures of 2900 K) as it is likely the spot temperature and number of spots is the same no matter the tilt of the star. We found the best fit stellar surface features for this scenario to be one large spot ($R_{spot}/R_s = 0.29$) that is slightly off-center to the pole with two smaller spots on either side ($R_{spot}/R_s = 0.16$ and 0.09 respectively). This spot configuration is shown in Figure 4.9 and has a final reduced χ^2 of 2.6. We also fit this scenario with one large spot instead of three spots, though the reduced χ^2 of this model was 3.96. Similar to the results with the non-tilted star, the AIC_c value for the one-spot model is lower than the three spot model (-10.38 and -3.04 respectively) due to the difference in parameters. The one-spot model does not fit the data well by eye, and again the χ^2 statistic favors the three spot model. Therefore,

Table 4.4: Parameters Derived from Pole-spot Model

Spot Temperature Range	[2700, 2900] K
Spot Radii (R_{spot}/R_s)	0.29, 0.16, 0.09
Stellar Inclination (i_s)[a]	$25 \pm 5°$
Sky-Projected Obliquity (λ)[a]	$75 \pm 10°$

[a] Uncertainties derived independently of one another.

we opt for the three spot model.

Finally, we calculate the out of transit variability for the *TESS* short cadence data and find it produces variability well below the *TESS* noise level with no additional large spots needed (see Figure 4.8). Table 4.4 reports the best-fit values from this analysis.

We use `SOAPv2` [148] to test the impact of a pole-spot on the RVs. A pole-spot under this scenario will inject a $\sim$10 m/s signal, which is 30% of the RV semi-amplitude. However, `SOAPv2` assumes an optical bandpass as it was designed specifically for the HARPS wavelength range (380 – 700 nm). Stellar activity decreases at longer wavelengths where the contrast between the spot and photosphere temperatures decreases [149]. As HPF operates at near-infrared wavelengths, we expect the overall impact of the spot to be suppressed by $\sim 2\times$ [149, 94]. Thus, the pole-spot's impact with this configuration is < 5 m/s – within the 1σ semi-amplitude uncertainty of 28.0 ± 6.3 m/s.

4.4.3 Evidence for Spot-Complex Evolution

We extend our spot model derived from the SDSS i′ transit to the APO SDSS r′ and *TESS* short cadence observations. We calculate new contrast values for the *TESS* and SDSS r′ band filters for a spot temperature of 2900 K. Using the exact spot-complex configuration for the misaligned system, we model the r′ band and TESS short cadence transits using `STSP`. The results showed that the same spot configuration could not fit either the *TESS* or APO r′ band transits.

A close inspection of individual *TESS* transits suggest *slight* changes in spot amplitude, duration, and location (though it always starts during ingress). However, the lack of precision within the individual *TESS* transits makes it near-impossible to map spot evolution of subsequent transits.

For the APO SDSS r′ transit, we chose to assume the same number of spots and spot temperature while allowing the location and spot radii to vary. We discover that the polar spot remains approximately the same radius but shifts slightly while the other two spots slightly increase in area (blue spots in Figure 4.10). Thus, while the general location of the features near the pole are consistent across six months, the individual star spots are most likely evolving from one transit to the next. This tentative evidence for small-scale spot

changes suggests caution when directly comparing transits observed at different times. If we instead allow the spot temperature to change rather than the spot location and radii, we find that the required contrast to fit the APO SDSS r′ transit is nearly perfectly dark (c = 0.90) if we assume the same spot configuration as found in Figure 4.9. Since the spot contrast required to fit the SDSS r′ transit is unreasonably dark, it is more likely there is small-scale spot evolution between transits.

4.5 Discussion

4.5.1 Comparison to Previous Work

While our qualitative conclusions generally agree with those from [19], there are notable exceptions.

Stellar Rotation Period: We determine a stellar $v \sin i$ of 3.59 ± 0.92 km/s for TOI-3884 in contrast to [19] who find a $v \sin i$ of 1.1 km/s. We arrive at the more rapid rotational value both via `HPF-SpecMatch` and CCF methods. We also attempted to duplicate their method by using a template star near-identical to their comparison star, LHS 1140[6] which is slightly cooler and lower mass than TOI-3884. However, we still obtain a $v \sin i$ of 3.5 km/s. Using the LAMOST-derived Hα EW, models from [133] constrain TOI-3884's rotation period < 10 days – faster than a $v \sin i$ of 1.1 km/s.

Planetary Mass: [19] derive a planetary mass of $16.5^{+3.5}_{-1.8}$ M$_\oplus$ using two RV ESPRESSO points. This is a 2.2σ discrepancy from our higher mass measured with HPF. We attempt to jointly fit both the HPF and ESPRESSO RV points, however, our model requires a 14 m/s jitter term added to the ESPRESSO RVs. ESPRESSO's bandpass of 380 – 780 nm is more susceptible to stellar activity [149]. `SOAPv2` approximates our pole-spot model should introduce a $\sim$10 m/s signal into optical ESPRESSO RVs – similar to the required jitter of our model. With 17 near-IR HPF RVs, we robustly measure a 4σ planetary mass; a measurement which should possess less stellar contamination.

Planetary Radius and Transit Depth Chromaticity: We measure a larger planet of 6.43 ± 0.20 R$_\oplus$ compared to [19] who report two different radii: 6.31 ± 0.28 R$_\oplus$ from GP fitting and 6.00 ± 0.18 R$_\oplus$ from `starry`. When investigating this discrepancy, we discovered that their transits [19] demonstrate significant chromatic variability even outside of the modeled pole-spot. Chromatic transits can either be explained via a background eclipsing binary [150], or unocculted stellar activity [97]. As we rule-out nearby companions, we explore the impact of stellar activity on our transit depth.

---

[6]LHS 1140's declination is inaccessible to the HET.

We fit a transit model to the two masked APO SDSS i′ and SDSS r′ transits holding a/R_s, impact parameter, transit ephemeris, and transit depth $(R_p/R_s)^2$ constant across both transits. We check for chromaticity in the masked APO transit depths between the SDSS i′ and SDSS r′ observations which could indicate a contaminating background source. Using the two masked transits we fit a transit using `exoplanet` [139] holding a/R_s, impact parameter, transit ephemeris, and a dilution term multiplied to the SDSS r′ transit depth. Assuming no chromaticity, the dilution term is equal to one. We determine a dilution term of 1.01 ± 0.02. There is no significant transit depth difference between these two wavelength bandpasses. However, both these depths are slightly shallower than the bluer g' transit in [19] and deeper than the IR ExTRA observation. Differing spot contrasts compared to the hotter photosphere creates deeper transits at bluer wavelengths [97]. We approximate by eye the depths of their individual transits. We fit both our and their wavelength-dependent depths using a simple unocculted star spot model from [97]:

$$D_{\mathrm{obs}} = \frac{D}{1 - f_{\mathrm{sp}}(1 - \frac{F_{\lambda,sp}}{F_{\lambda,ph}})} \qquad (4.1)$$

where D_{obs} is the wavelength-dependent observed transit depth, D is the true transit depth, f_{sp} is the spot coverage fraction, and F_λ is the wavelength-dependent flux of the spot (sp) and photosphere (ph) respectively. The unocculted spot model fits the four transit depths assuming a spot temperature of 2900 K, total unocculted spot coverage of 16%, and a true planet radius of ∼6.2 $R_\oplus$. We do not include uncertainties in these numbers as the [19] transit depths and uncertainties are relied on by-eye approximations. However, this model demonstrates that the chromatic transit depth is explained by unocculted stellar activity which slightly impacts the measured radius of the planet (∼1σ discrepancy from our radius).

Stellar Inclination and Spot Properties: We fit a spot model based on the values reported in [19] to the SDSS i′ transit, determining a best-fit χ_r^2 of 6.09. Assuming the spot is evolving over time, it is possible that the spot evolved between the two observations. However, their spot model generates significant (∼1%) out of transit variability that is not observed in the TESS nor ground-based photometry. Accounting for the lack of baseline variability enabled us to constrain the stellar inclination to $25 \pm 5°$ which in turn impacted our overall best-fit spot model.

4.5.2 Comparison of TOI-3884b in M Dwarf Planetary Parameter-Space

Super-Neptunes (4 $R_\oplus < R_p < 8$ $R_\oplus$) represent a transitional population of planets between the rocky terrestrial planets and Jovian gas giants. TOI-3884b adds to the growing sample of

well-characterized (with precise 3σ masses and radii) super-Neptunes orbiting M dwarfs. In particular, 4.11a shows TOI-3884b's position in a planetary mass-radius plane with respect to other M dwarfs (T_{eff}< 4000 K) planets with known ($> 3\sigma$) masses and radii. Figure 4.11b plots the same sample as a function of stellar effective temperature.

The formation of Jovian planets around M dwarfs should be inhibited by the longer orbital time scales with respect to the disk lifetimes [87, 151]. This is corroborated by empirical data from RV surveys [152, 153, 154, 155]. However, [87] predict that M dwarfs should host an abundance of Neptunes that fail to accrete a massive enough core ($\sim 10~M_\oplus$) [156] in a timely manner to initiate runaway gaseous accretion. Using models from [157] and propagating the uncertainties in planetary parameters using the Monte-Carlo method, we predict TOI-3884b's core mass to be about $21 \pm 4~M_\oplus$. It should therefore have experienced some runaway gaseous accretion. The fact that TOI-3884b did not accrete a Jovian-mass atmosphere suggests that its core was slow to form, or there was a lack of nearby gas/material for rapid accretion or both.

4.5.3   Atmosphere of TOI-3884b

While the spot portion of the transit may complicate the analysis, TOI-3884b has the highest transmission spectroscopic metric (TSM) [158] of any known planet with an equilibrium temperature < 500 K (TSM: 230 – Figure 4.12). Owing to its bright host star and large transit depth, this planet also has one of the highest metrics of any known non-Hot Jupiter planet. At 430 K, TOI-3884b's atmosphere likely contains methane as the carbon-dominant molecule along with water and some ammonia – assuming equilibrium chemistry [159, 160, 161, 162]. Deriving the overall abundances of these molecules would provide an approximate C/N/O ratio, a useful measurement for constraining where this planet originally formed in its disk [163, 164, 165]. [166] demonstrate the connection between C/O ratios and various molecular snow-lines. [167] expand on this study by noting that nitrogen provides information surrounding the disk's overall metallicity, as it is unaffected by the condensation of molecules such as water, carbon dioxide, and methane. Only the ammonia snow-line at $\sim$100 K and N_2 snow-line at $\sim$78 K significantly affects its overall ratio in the disk. TOI-3884b is therefore an extremely promising target to observationally test the link between nitrogen abundance and formation location.

Due to the combination of its cool equilibrium temperature along with experiencing UV-radiation from its active M dwarf host, TOI-3884b's atmosphere is likely comprised of photochemically created hazes such as tholins (e.g., [168]) or even soot [169]. Photochemically created hazes (e.g., [170]), and aerosols in general, are common in exoplanetary atmospheres with several studies linking their presence to temperature [171, 172, 173]. Assuming the trend

highlighted in [173] holds, we would expect TOI-3884b to possess a fairly hazy transmission spectrum in the near-infrared. However, [174] show that hazes should become translucent at longer wavelengths assuming the overall particle sizes are small. Thus, extending out to >3 μm should enable atmospheric characterization of TOI-3884b regardless of its expected hazy atmosphere.

We generate the expected transmission spectrum of TOI-3884b using `ExoTransmit` [160] assuming a 100× Solar metallicity atmosphere with no aerosols, aerosols at pressures of 100 μbars and aerosols at pressures of 10μbars (Figure 4.13). For these simulations we assume a gray-opacity aerosol layer which is wavelength independent. Using the cloud-free model, we used PandExo [175] to simulate two transit observations with *JWST* NIRSpec-Prism. We find that we should easily retrieve methane and water in both the cloud-free and 100 μbars cases. At 10 μbars we will still observe methane absorption features with tentative detection of water. It should be noted however, that these simulations assume a typical transit shape which allows for easily derived uncontaminated transit depths. Assuming the bump-feature in TOI-3884b's transit remains long-lived, it is possible that the uncertainties presented in Figure 4.13, are underestimated and stellar contamination will also need to be included in modeling the observed transmission spectrum.

4.5.4 Orbital Alignment of TOI-3884b

Assuming the pole-spot hypothesis, TOI-3884b possesses a misaligned orbit with an obliquity of 75 ± 10°. TOI-3884b therefore joins the growing population of misaligned warm-Neptunes (R >4 $R_{\oplus}$), which includes the two M dwarf Neptunes: GJ 3470b [176] and GJ 436b [177].

Neither Gaia nor the HPF RV residuals detect evidence of any outer massive companion in the TOI-3884 which could have been responsible for TOI-3884b's misaligned orbit [178]. Of the four misaligned Neptunes orbiting K and M dwarfs, two (HAT-P-11b and WASP-107b)] [179, 180] have a confirmed outer companion while [176] does not exclude the existence of an outer planet in the GJ 3470 system. Giants around M dwarfs are uncommon; it is unlikely that TOI-3884 hosts an additional gas giant responsible for the misalignment of TOI-3884b. However, our RV observations are limited to < 6 months. Continued radial velocity monitoring is required to detect longer period massive planets in this system.

4.6 Conclusion

We confirm the planetary nature of TOI-3884b, a super-Neptune crossing a persistent spot during transit. This spot-crossing event is chromatic, and we conclude this bump is created by a large star spot which appears at the same location in every transit spanning over a year

of monitoring. We present two hypotheses: 1) TOI-3884's rotation is exactly equal to its planet's orbital period of 4.56 d, or 2) TOI-3884 rotational axis is tilted along our line of sight and TOI-3884b crosses a polar spot. Given the lack of significant photometric or spectroscopic variability in the RVs, TESS light curves, and ground-based monitoring spanning over six months, we strongly prefer the second pole-spot hypothesis. In this scenario, TOI-3884's spin-axis is inclined along our line-of-sight. TOI-3884b therefore possesses a misaligned orbit that is nearly polar to its star. TOI-3884b joins the population of misaligned warm-Neptunes around low-mass stars [181].

We also discover signs of spot evolution between the different transits. While the in-transit bump appears at a similar position, its overall structure changes on measurable timescales. The TOI-3884 system presents a rare opportunity to monitor pole-spot evolution on an active mid-M dwarf.

4.7 Acknowledgements

---

[7]https://www.cosmos.esa.int/gaia
[8]https://www.cosmos.esa.int/web/gaia/dpac/consortium

Figure 4.7: **Top:** Projected starspots on TOI-3884's stellar surface for an aligned system using the APO i' filter transit observed on 2022 April 05 assuming a spot temperature of 2900 K and a photospheric temperature of 3200 K (spot contrast of 0.5) for the three spot model (red) and one spot model (blue). The planet's crossing path is defined by the blue dotted lines with the central dotted line corresponding to the equator of planet and the outer dotted lines denoting the full extent of the planet, and the central latitude of the transit is marked with a red vertical line. The large red spot in the middle has a relative radius $R_{spot} = 0.44$ R_s with the two smaller red spots having radii $R_{spot} = 0.10$ and 0.07 R_s respectively. The large blue spot has a relative radius $R_{spot} = 0.63$ R_s and is mostly out of the transit chord. The fractional spotted area for the three spot model in the transit chord for these stellar surface features (assuming there are no spots anywhere else on the star) is 11%. **Middle:** Best fit three spot model for aligned system shown in red line compared to the best fit one spot model in blue line and the no star spot transit model in cyan with the APO 20s i' band data as black points with error bars. **Bottom:** Residuals from the three spot best-fit starspot model (red) and one spot best-fit model (blue).

98
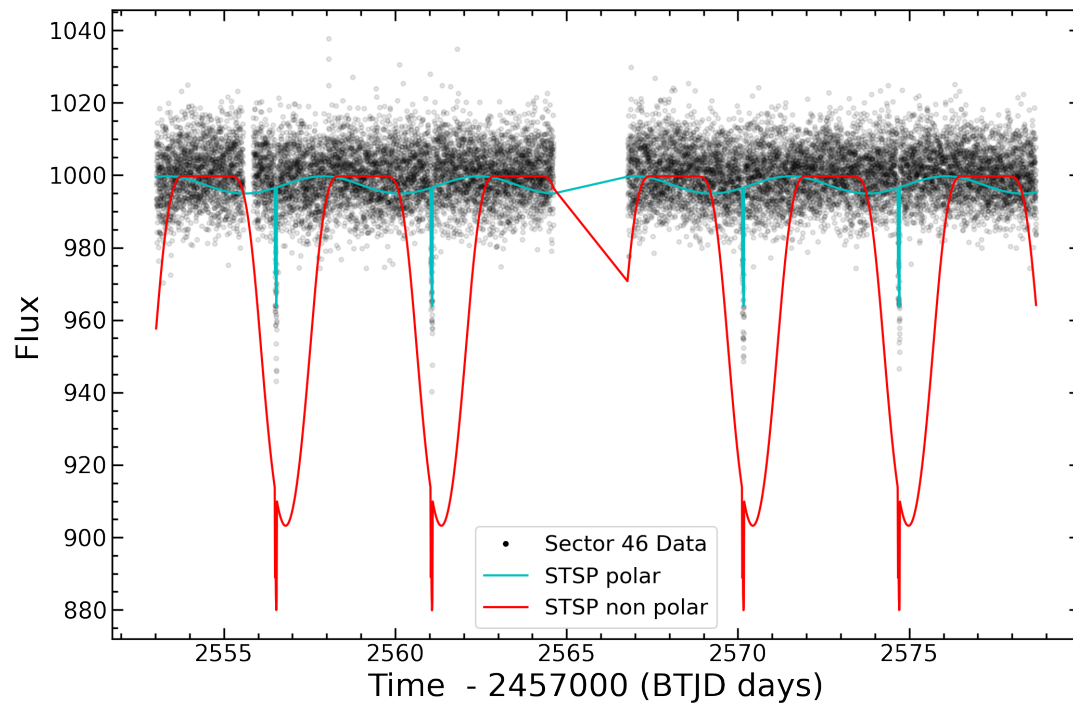
Figure 4.8: TESS Sector 46 short cadence (2 minute) data shown in black points with aligned starspot model (red line) and polar starspot model (cyan line). The same pattern can be seen in TESS Sector 49 short cadence data though it is not reproduced here.
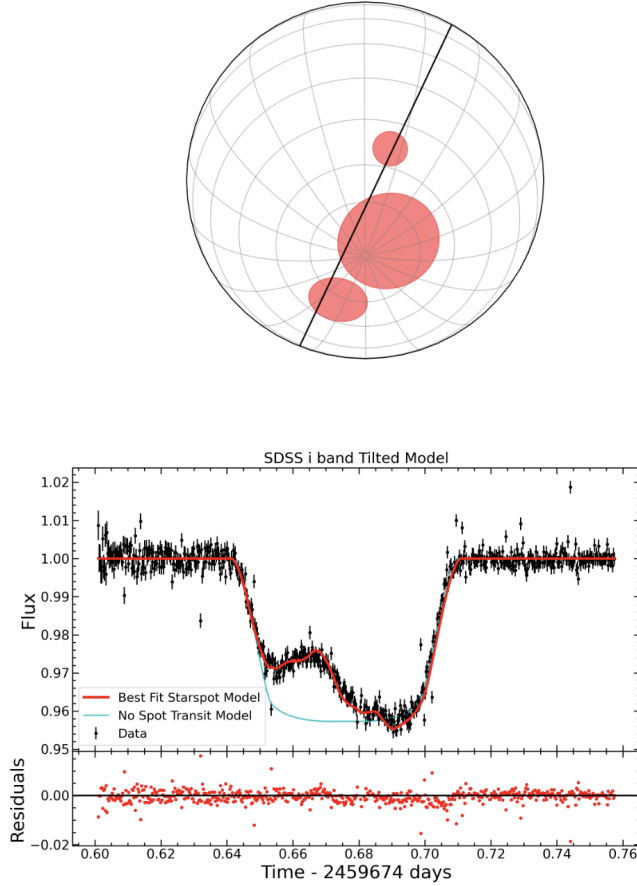
Figure 4.9: **Top:** Projected star spots on TOI-3884's stellar surface for a polar star spot with a stellar spin axis tilt of $-65°$ and $\lambda = 75°$ using the APO SDSS i' filter transit observed on 2022 April 05 assuming a spot temperature of 2900 K and a photospheric temperature of 3200 K (spot contrast of 0.5). The large spot in the middle has a relative radius $R_{spot}/R_s = 0.29$ with the two smaller spots having radii $R_{spot}/R_s = 0.16$ and 0.09 respectively. The fractional spotted area in the transit chord for these stellar surface features assuming there are no spots anywhere else on the star is 3%. The black line shows the path of the equator of the planet as it crosses the star. **Bottom:** Best fit starspot model for the oblique (not aligned) system shown in red line compared to the no starspot transit model in cyan with the APO 20s i' band data as black points with error bars.
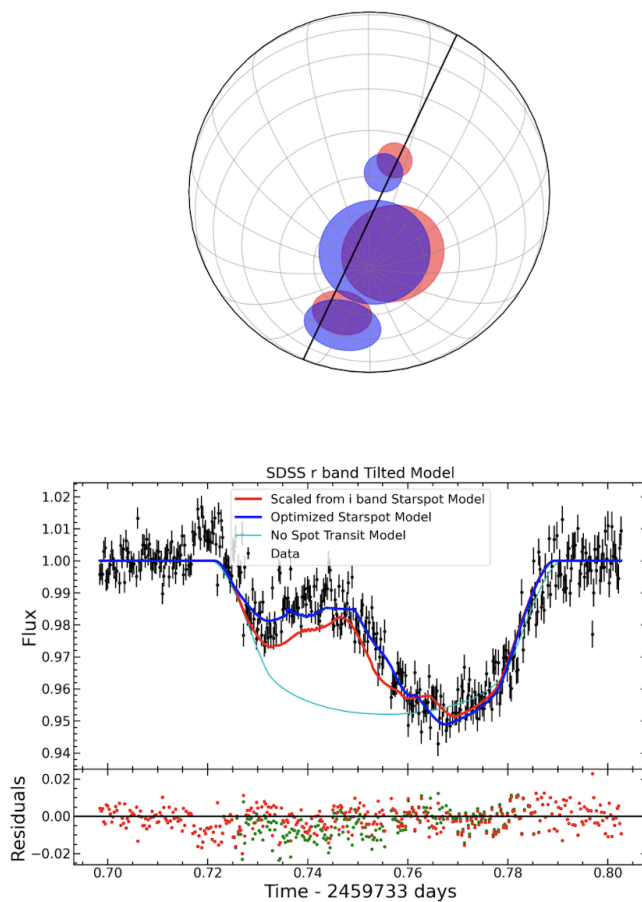
Figure 4.10: **Top:** Projected star spots on TOI-3884's stellar surface for a polar star spot with a stellar spin axis tilt of $-65°$ and $\lambda = 75°$ using the APO SDSS r' filter transit observed on 2022 June 03 assuming a spot temperature of 2900 K and a photospheric temperature of 3200 K (spot contrast of 0.7 for r' band). The large blue spot in the middle has a relative radius $R_{\mathrm{spot}}/R_s = 0.31$ with the two smaller blue spots having radii $R_{\mathrm{spot}}/R_s = 0.22$ and 0.11 respectively with the red starspots corresponding to the same starspots shown in Figure 4.9. The fractional spotted area in the transit chord for the blue stellar surface features assuming there are no spots anywhere else on the star is 4%. **Middle:** Best fit starspot model for the oblique (not aligned) system shown in blue line compared to the no starspot transit model in cyan with the APO r' band data as black points with error bars. The red line is the STSP model created by extending the SDSS i' polar spot model to the SDSS r' contrast. **Bottom:** Residuals from the best-fit star spot model (blue points) and scaled from SDSS i' polar spot model (red points).

a) Planet radius as a function of mass

b) Planet mass as a function of T_{eff}
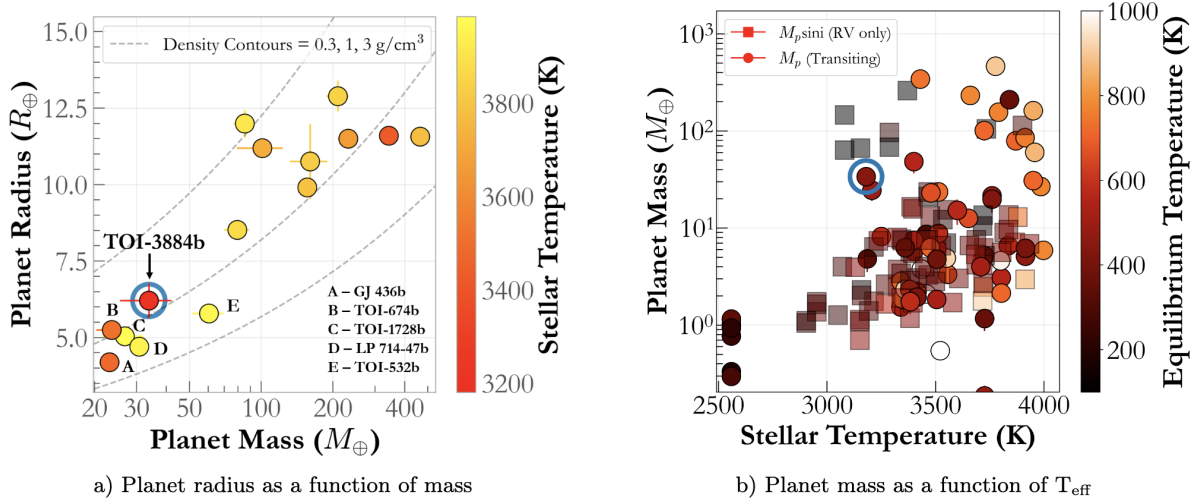
Figure 4.11: Sample of transiting M dwarf planets that have precise mass measurements ($> 3\sigma$). **a)** Mass-Radius plane showing the small sample (~ 15) of giant planets ($R_p > 4\ R_\oplus$) orbiting M dwarfs ($T_{eff} < 4000$ K), color coded by T_{eff}. **b)** The masses for all M dwarf planets as a function of T_{eff}, showing how TOI-3884b stands out in terms of its stellar host. Transiting planets are shown as circles, whereas RV only (m $\sin i$) detections are in squares. The clump of planets at ~ 2600 K represent the TRAPPIST-1 system [17].
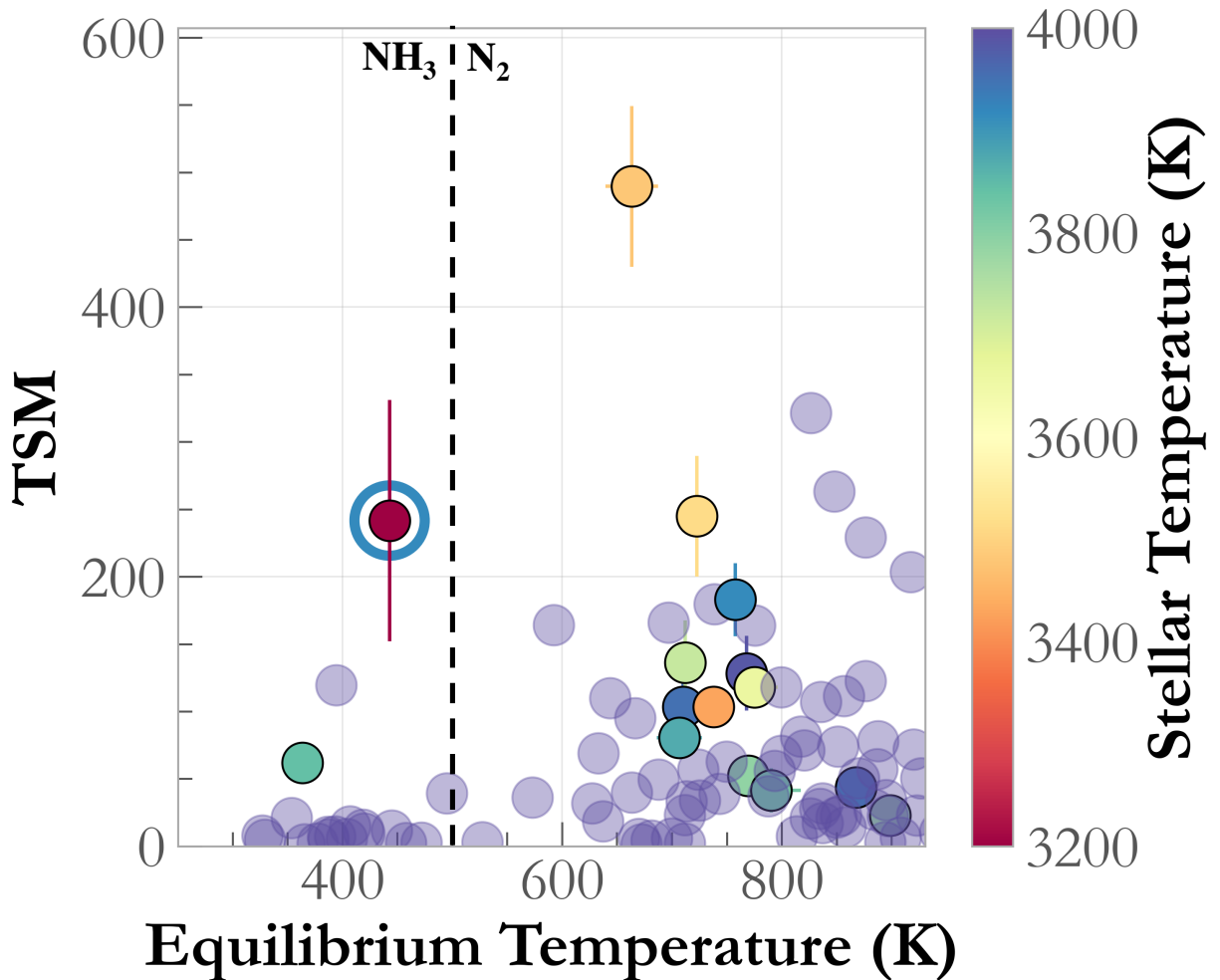
Figure 4.12: Transmission Spectroscopy Metric (TSM) as a function of planetary equilibrium temperature for all planets with a known ($>3\sigma$) mass and Teq cooler than 1000 K. Points are colored based on their host star's effective temperature with planets around M dwarfs denoted with solid coloring. The approximate temperature when ammonia appears in a planet's atmosphere (assuming equilibrium chemistry) is denoted with the black dashed line. TOI-3884b (blue circle) possesses one of the highest TSMs of any non-Hot-Jupiter and the highest TSM for planets < 500 K.
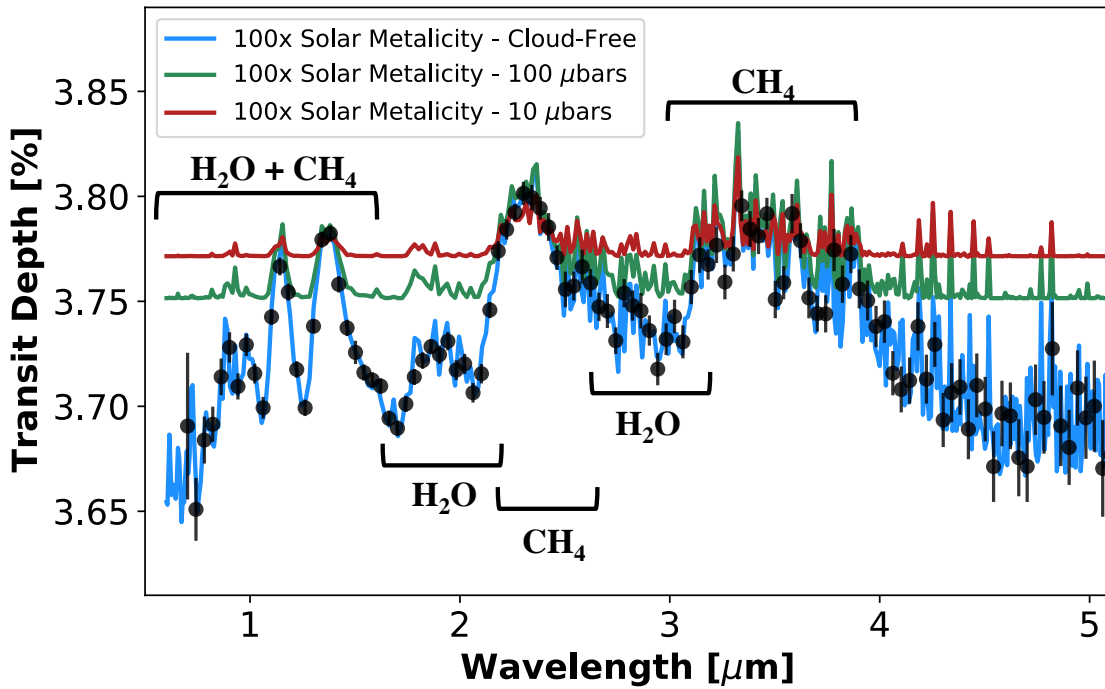
Figure 4.13: Transmission spectra generated with `ExoTransmit` for a $100\times$ Solar metallicity atmosphere in chemical equilibrium with gray-absorber aerosol layer at 10 and 100 μm. Simulated data is created using `PandExo` for two transits of JWST-NIRSpec and based on the cloud-free model. The two dominant absorbers, water and methane, are labeled for reference though other molecules including ammonia are also included in the models.

Chapter 5

Future Work

5.1   More Stars with STSP

STSP is a powerful tool that can illuminate stellar surface features on small scales. Given that the best constraints on the stellar surface involve using the transit of a companion, there are some restrictions to the systems that can be throughly modeled using STSP. However, with the large number of known exoplanet and eclipsing binary systems with high precision data from space-based missions like *Kepler*, *K2*, and TESS, there are a number of systems that could still be modeled. In order to investigate the exact systems with many starspot crossing events during transits, a through statistical search would need to be performed for the *Kepler*, *K2*, and TESS catalogs. The exact statistical measure with which to decide systems to include would need to be decided, though it would need to include a comparison between the normalized fluxes for the points in-transit versus out-of-transit when compared to a no spot transit model. This type of procedure has been done for the *Kepler* catalog by an undergraduate student with only 17 systems out of 4696 being found to have deep, non-grazing transits with a measured rotation period and high enough difference between the in-transit and out-of-transit residuals. If we assume the same number of systems could be found in the *K2* and TESS data sets, then an additional 1-2 systems could be added from the *K2* catalog and 14-16 new systems from the current TESS catalog.

There is at least one very unique red giant star with an M dwarf companion (KOI-1786) that was identified as a very good target for STSP modeling with the *Kepler* search. KOI-1786 shows signs of spots in every one of its *Kepler* transits with some spot features reaching to nearly the baseline normalized flux. With spots of that amplitude, they must be very dark and large, and they could be a direct comparison to TiO band modeling done on other red giants stars [14]. The overall goal with having more systems be modeled with STSP is to further our understanding of the relationship between the spectral type of a star (or the temperature of the star's photosphere) and the starspot properties of the star. Ideally, we would further expand the plot reproduced here from [18] by adding new data points from our photometric results. This plot is shown in Figure 5.1 and shows the temperature difference between the spot and photosphere (ΔT) versus the photospheric temperature of the star for a number of stars, including the Sun (orange squares). However, this plot especially lacks many points in the M to mid K spectral range, so more data in that range is needed. Additionally, historically these data points were made using spectroscopic methods that are

not as effective for lower temperature stars, but with high-precision photometric data, we can add more M and K type stars to the mix. Once more lower mass stars have been added to the plot, then more accurate empirical relationships can be found as was done by [18]. Additionally, since our photometric technique allows for a more robust study of the small scale surface features of the stars, we can also create similar plots and empirical relationships with other starspot properties, like mean starspot radius and fractional spotted area.

Further studies with STSP that involve a wide range of stellar types and rotation periods will also lead to important characterizations of starspot lifetimes and thus their decay rates. Studies using *Kepler* data have shown that cooler stars have spots that last for longer periods of time, but these methods use rough estimations of the starspot sizes from their full out-of-transit light curves [182, 183, 184]. With more accurate starspot models for a range of stars, the relationship between spot lifetime and stellar type could be further examined. Additionally, more accurate models of stellar surface features along with starspot temperatures estimated from ground-based photometry could allow for more accurate predictions of radial velocity jitter caused by stellar activity [185]. Lastly, differential rotation is a very important component of the Sun's magnetic activity cycle, and STSP can be used to tease out the differential rotation of stars if there is enough coverage in the *Kepler*, *K2*, or TESS data like for Kepler-17 [186]. Understanding the amount of differential rotation and the lifetimes of spots on stars similar to the Sun [187] and different to the Sun would then help to further illuminate the role of these properties in the magnetic cycle of stars. Thus, by expanding the range of stars studied and modeled using STSP and high-precision photometry, we could further our understanding of the properties of stars.

Another future step is to determine for previously modeled systems, like HAT-P-11 and KOI-340, if they have any significant more recent starspot crossing events in their TESS data. Since TESS is observing the whole sky to detect new exoplanet transits, it will also re-observe known transiting objects, which means for the systems we know host starspot crossing events there is new data to model. TESS is optimized for brighter stars, and due to the large pixel size, there is a lot of blending that can occur between any nearby objects [188]. This means the data might not be as precise as the *Kepler* data, but it should still be precise enough to model with STSP, considering we have successfully modeled ground-based light curves as well.

5.2   TOI-3884: The Future

5.2.1   Updated Transit Depth Spot Modeling

While in the process of submitting and publishing the results from our STSP modeling of TOI-3884 (see Chapter 4, another group published additional ground-based follow up on the
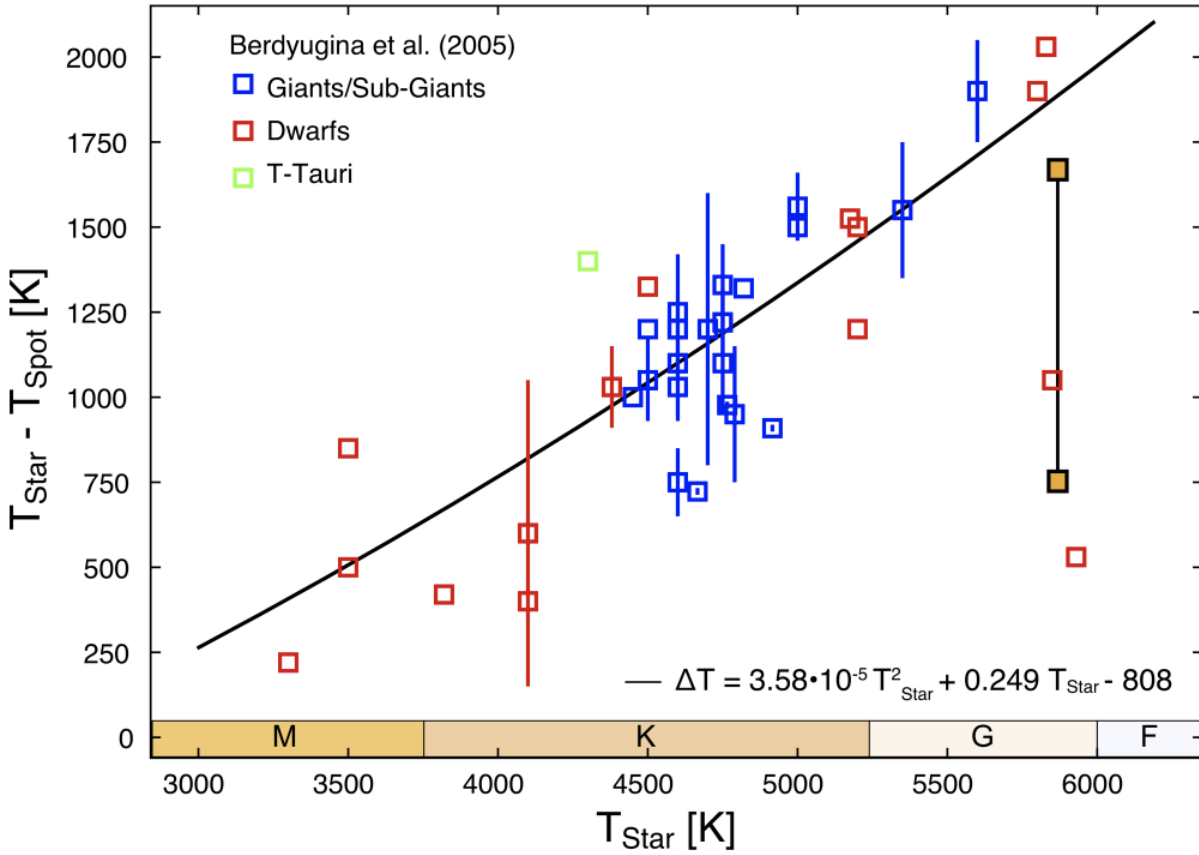
Figure 5.1: Figure from [18] that plots the difference between the spot temperature and photosphere temperature (ΔT) and the photospheric temperature for the stars (K) in [2] with giant and subgiant stars shown with blue squares, dwarf stars in red squares, T-Tauri as a green square, and the Sun as two orange squares (the bottom one is for the penumbra temperature and the top for the umbra). The black line shows the empirical fit to the data points from [2].

same object and modeled the persistent spot with a different technique [19]. They modeled the spot feature using `starry`, which is a python package that can model starspots using spherical harmonics [42]. From their modeling, they were only able to fit it as one large spot with similar stellar inclination and misalignment of the planet's orbit (i.e. $\lambda \neq 0°$). The effect of the large polar spot causes changes in the transit depth with wavelength due to the transit light source effect [1]. As mentioned, `STSP` requires knowledge of the transit model parameters themselves in order to accurately determine the spot sizes and locations, so any interference from the spot on the transit depth will impact the resultant spot properties. However, they obtained a near-infrared (near-IR) transit of the system, which minimizes the interference from the spot on the transit depth itself [19]. It is important to note that while this near-IR transit does minimize the effect of the spot on the true transit depth, it does still show signs of a spot feature, so in order to get the true transit depth, a far-IR transit would need to be obtained.

Using the updated transit depth from the near-IR data, we remodeled the SDSS i' APO transit. Though we updated the transit depth, we did not change any other transit model parameters as they were all within the uncertainties for our model [44]. For our initial remodeling of the spots, we have assumed the number of spots (3) has not changed from our previous best fit models, and we started with the same best fit contrast (corresponds to a spot temperature of 2900 K). We then ran `STSP` with an initial guess for the spot sizes and positions equal to the previous best fit solution. The updated best fit `STSP` model (red line) is shown compared to the previous model (blue line) in middle panel of Figure 5.2 with the associated projected spots shown in the Top panel of Figure 5.2. Interestingly, the biggest difference between the two models is the spot closest to the ingress of the transit is much larger in our updated model with little change to the middle and egress spots. This model does produce the lowest reduced χ^2 =2.06 of any of the `STSP` models.

While our updated model does produce a better overall fit to the SDSS i' data, one of the main concerns with our previous model is that it did not match the SDSS r' transit that was obtained around one month later. With our newly updated best fit model, we wanted to check if this model could now fit the r' transit. After changing the contrast to match the r' band while keeping the spot configuration fixed, we plotted the updated best fit model along with the previous best fit model in Figure 5.3. The updated best fit model still does not fit the SDSS r' data well, which lends more credence to possible small scale spot evolution occurring on month timescales that was proposed in [44].

While our updated i' model is a step in the right direction towards producing the best possible spot model for TOI-3884, there is still more work to be done. In addition to completing the modeling for the APO SDSS r' transit, we have observed an additional transit

this past January in another filter, Semrock [189]. Also, there is evidence in small changes between individual TESS transits, so it would be very interesting to model each TESS transit independently to further study the possible small-scale spot evolution in the system. This larger scale `STSP` modeling of every individual transit for TOI-3884 b is thus left as future work.

5.2.2   Modeling of Simultaneous Data

We have also obtained one transit of TOI-3884 b on 2023 February 16 using APO's 3.5-m ARC telescope that was observed in two filters, SDSS g' and SDSS i', simultaneously. This transit was observed using a filter swapping technique where the filter wheel moves from one filter to anther between exposures. Using this technique, we can observe the persistent starspot feature in two filters simultaneously without needing a multi-filter instrument. However, the cadence is not as optimal compared to a multi-filter instrument because there is an extra time added when moving the filter wheel, and we can only observe in one filter at a time so there are less data points for both filters per transit. Since we observe in one filter at a time, we do not lose any light do to the beam splitting that is necessary with multi-filter instruments, which is great for an object like dimmer object like TOI-3884. For this observation, the i' was observed with a 10 s exposure time, and the g' was observed with a 45 s exposure time. Unfortunately, the engineered diffuser that is available at APO was not operational on this night, so the object was instead defocused to help increase the precision of the observations. The data were reduced using AstroImageJ [190] with precision of 6 mmag in i' and 7 mmag in g'.

The modeling for these data is still ongoing; however, I will present my most recent results. Since we have previously modeled an APO i' transit, the initial modeling was based on the previous best-fit `STSP` model (see Figure 5.2). From the previous modeling, we concluded that the most likely spot temperature is 2900 K, so we started with that spot temperature for our modeling of these transits (correspond to $c_i = 0.5$ and $c_g = 0.7$). Also, the i' data is slightly higher precision and is the same filter as the previously modeled transit, so we chose to optimize the model using that transit. From my initial `STSP` modeling of this i' transit, the best fit starspot configuration is very similar to previous models with one large spot $R_{spot} = 0.37 \, R_s$ in the middle surrounded by one slightly smaller spot before $R_{spot} = 0.22 \, R_s$ and after $R_{spot} = 0.08 \, R_s$ the middle spot (see Figure 5.4). This model produces a reduced $\chi^2 = 2.53$. If we then take this spot configuration and change the contrast to match for the g' filter, we can produce the `STSP` model for that data since the spot configurations should be the exact same. This produces an `STSP` model with reduced $\chi^2 = 2.82$ for the g' transit. The comparison of these `STSP` models to the data can be seen in Figure 5.4.

While this spot model does fit the data well, this is still only a preliminary result as we have yet to fully explore the other spot temperatures, the number of spots, and the system parameters (specifically the λ and stellar inclination angle). We have also not yet compared this spot configuration and model to any of the previous transits. A complete investigation of all of the transits and possible spot temperatures is therefore left as future work.

5.2.3 TOI-3884 with JWST

Ideally, we would also observe a transit of TOI-3884 b spectroscopically as well in order to measure the temperature of the starspot using multiple techniques. However, for M dwarf stars, the usual molecular band modeling is not ideal as most of the temperature sensitive lines are present in the photospheres of these stars (e.g. TiO index). Therefore, the contributions from both the photosphere and cooler spots blend together [2]. Therefore, we need a temperature sensitive index that is catered towards M dwarf stars, like the H20 - K2 one described in [191] and shown below.

$$H20 - K2 = \frac{\langle F(2.070 - 2.090)\rangle / \langle F(2.235 - 2.255)\rangle}{\langle F(2.235 - 2.255)\rangle / \langle F(2.360 - 2.380)\rangle},$$

where $\langle F(a - b)\rangle$ denotes the median flux level in the wavelength region defined by a and b. This H20 - K2 index is an infrared index which makes space-based missions like JWST ideal. Additionally, the effect in the index versus spot temperature is subtle and requires no telluric water to be present in the spectrum, which would further require space-based spectrophotometric capabilities. Since the spot on TOI-3884 is so large, the effect of the planet would be negligible compared to the effect of the spot on the spectrum, which is good as we are interested in measuring the spot temperature rather than the exoplanet's atmosphere.

In order to investigate if we could measure the spot temperature using the proposed index, we generated synthetic spectra for TOI-3884 from 1.66-3.09 μm, binned to the resolution of the G235M grating on the NIRSpec instrument with appropriate uncertainties from the available JWST ETC for three separate points in the transit. We created an out-of-transit spectrum, an in-transit spectrum that assumes the planet is completely covering the spot, and an in-transit spectrum that assumes the planet completely covers the photosphere. The left panel of Figure 5.5 shows the ratio of the in-transit spectrum where the planet covers the spot completely compared to the out-of-transit spectrum for six different spot temperatures for a total spot covering fraction of 12%. The gray bars in this figure indicate the wavelength regions used to generate the temperature sensitive index mentioned above. We then generate the H20-K2 index for all six spot temperatures for the following set of fractional spotted areas:

12%, 14%, 16%, 18%, and 20%. This is plotted in the Right panel of Figure 5.5, which shows the calculated index versus spot temperature. Our spectroscopic index is highly sensitive to the temperature of the spot, but is largely insensitive to the fractional spotted area, which is great as the goal of this type of observation is to measure the spot temperature regardless of the fractional spotted area. Again, it is important to note that while this measurement is only feasible with JWST as the index changes are very small and thus require the absence of any Earth's atmosphere.
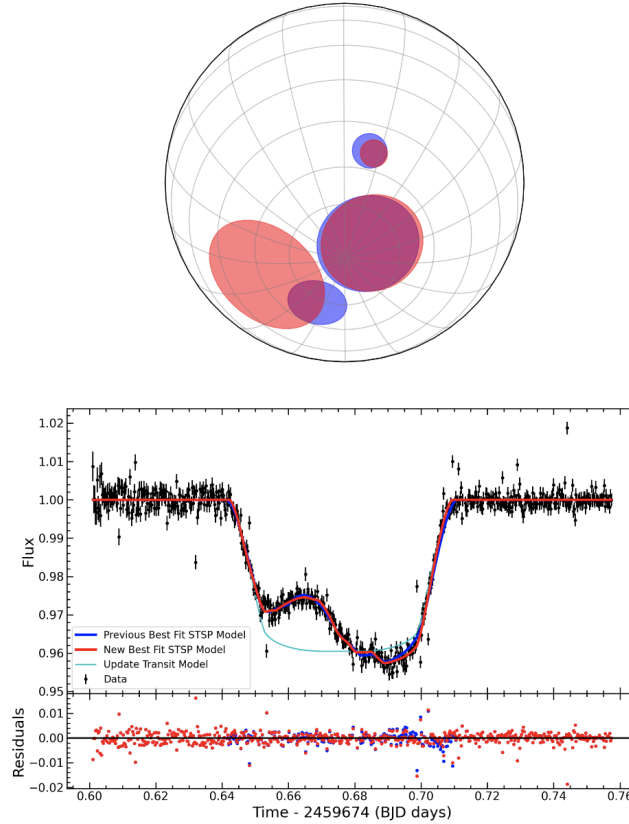
Figure 5.2: **Top:** Projected starspots on TOI-3884's stellar surface using the APO i' filter transit observed on 2022 April 05 assuming a spot temperature of 2900 K and a photospheric temperature of 3200 K (spot contrast of 0.5) with an updated transit depth to match [19]. The large spot in the middle has a relative radius $R_{spot} = 0.29$ R_s with the largest spot to the left of the middle spot having a radius $R_{spot} = 0.38$ R_s and the smallest spot to the right of the middle spot having $R_{spot} = 0.07$ R_s. The fractional spotted area in the transit chord for these stellar surface features (assuming there are no spots anywhere else on the star) is 11%. **Middle:** Best fit star spot model for previous transit depth shown in blue line compared to the updated best fit STSP model shown with red line and the updated no star spot transit model in cyan with the APO 20s i' band data as black points with error bars. **Bottom:** Residuals from the both the previous best-fit starspot model in blue points and the updated best-fit model in red points.
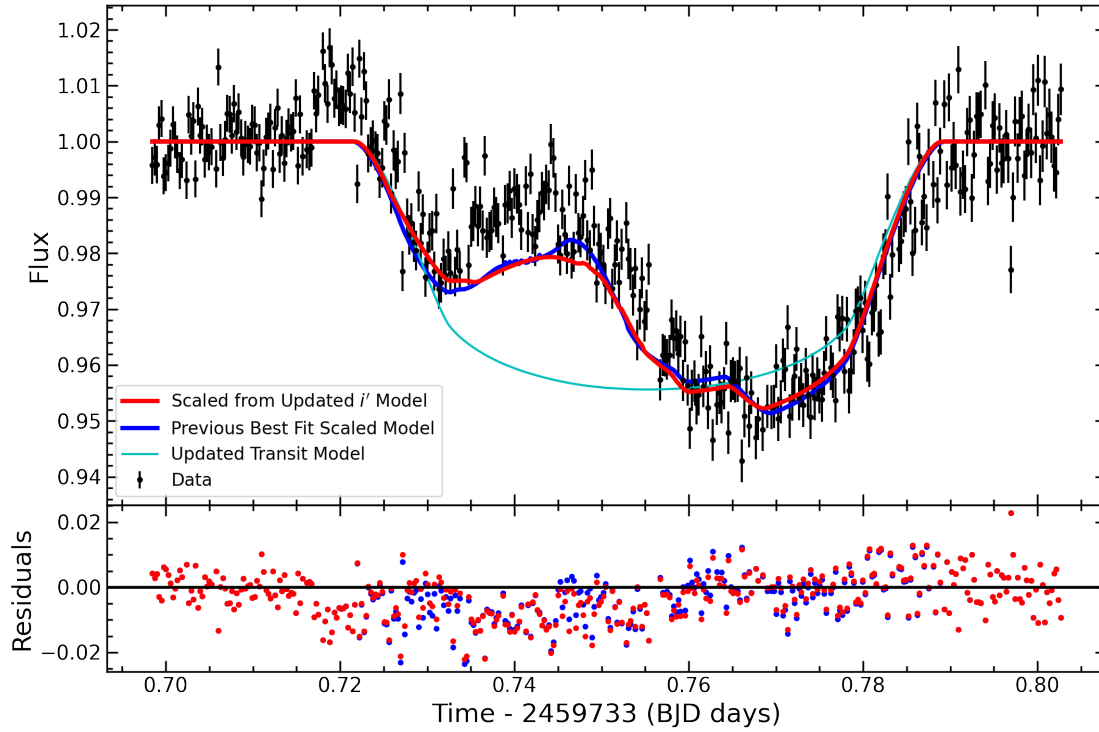
Figure 5.3: **Top:** Best fit `STSP` model scaled to the SDSS r' contrast (still assuming a spot temperature of 2900 K and a photospheric temperature of 3200 K) for the updated transit depth model (red line) and previous best fit `STSP` model (blue line) shown alongside updated no-spot transit model in cyan with APO SDSS r' data in black points.**Bottom:** Residuals from the both the previous best-fit starspot model in blue points and the updated best-fit model in red points.
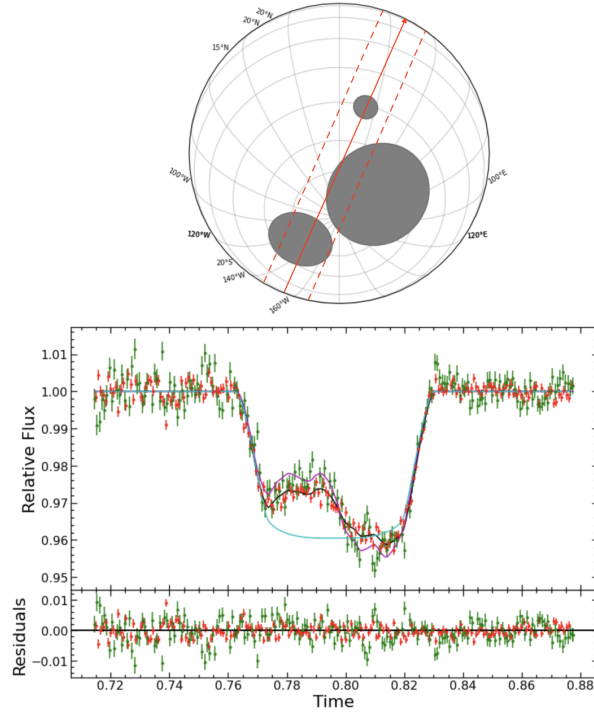
Figure 5.4: **Top:** Projected starspots on TOI-3884's stellar surface using the APO i' filter transit observed on 2023 February 16 for modeling assuming a spot temperature of 2900 K and a photospheric temperature of 3200 K ($c_i = 0.5$) with an updated transit depth to match [19]. The large spot in the middle has a relative radius $R_{spot} = 0.37$ R_s with the largest spot to the left of the middle spot having a radius $R_{spot} = 0.22$ R_s and the smallest spot to the right of the middle spot having $R_{spot} = 0.08$ R_s. The red lines show the transit chord of the planet. The fractional spotted area in the transit chord for these stellar surface features (assuming there are no spots anywhere else on the star) is 5%. **Middle:** Best fit star spot model for APO i' filter transit observed on 2023 February 16 shown in black line compared to the i' data (red points). The g' data that was taken during the same transit is shown in green points red line with the scaled `STSP` model for the g' contrast ($c = 0.7$) shown in magenta line. **Bottom:** Residuals from the both the i' best fit model compared to its data in red points and the g' best-fit model to its data in green points.
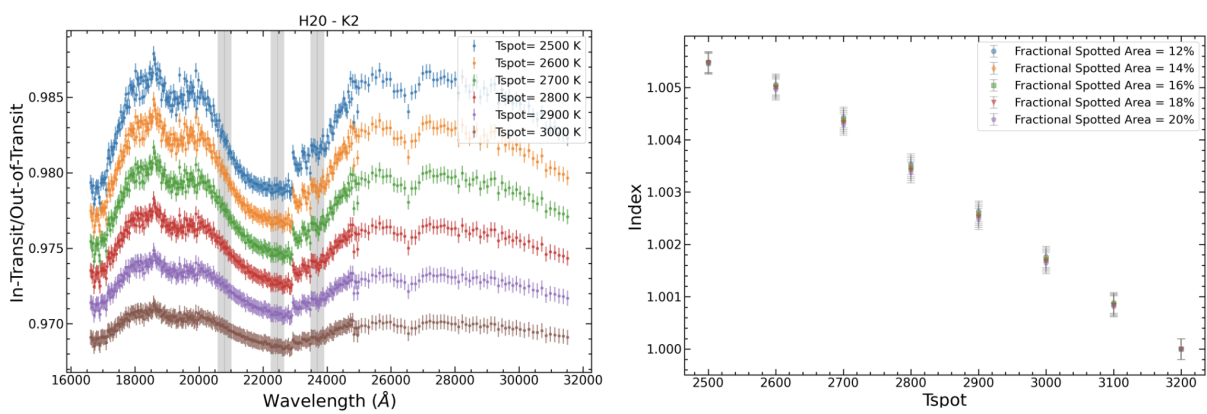
Figure 5.5: **L**eft: Ratio of the in-transit spectrum of TOI-3884 (phase=-0.013) to the out-of-transit spectrum assuming the planet is covering 100% spot. The coolest spot (top, blue line) produces relative fluxes closest to 1.0 because there is little light lost when the planet blocks a very dark, cool spot. As the spot temperature approaches the photospheric temperature, the relative fluxes will approach a flat-line with a value derived from the transit depth ($\delta = 3.6\%$). **R**ight: H20-K2 index with 1σ error bars versus T_{spot} for a range of sizes $f_{spot} = 12, 14, 16, 18, \& 20\%$ spot coverage.

References

[1] B. V. Rackham, D. Apai, and M. S. Giampapa, The Astrophysical Journal **853**, 122 (2018).

[2] S. V. Berdyugina, Living Reviews in Solar Physics **2**, 8 (2005).

[3] J. P. Wisniewski, A. F. Kowalski, J. R. A. Davenport, G. Schneider, C. A. Grady, L. Hebb, K. D. Lawson, J.-C. Augereau, A. Boccaletti, A. Brown, J. H. Debes, A. Gaspar, T. K. Henning, D. C. Hines, M. J. Kuchner, A.-M. Lagrange, J. Milli, E. Sezestre, C. C. Stark, and C. Thalmann, The Astrophysical Journall **883**, L8 (2019).

[4] B. M. Morris, L. Hebb, J. R. A. Davenport, G. Rohn, and S. L. Hawley, **846**, 99 (2017).

[5] R. Sanchis-Ojeda and J. N. Winn, The Astrophysical Journal **743**, 61 (2011).

[6] S. E. Thompson, J. L. Coughlin, K. Hoffman, F. Mullally, J. L. Christiansen, C. J. Burke, S. Bryson, N. Batalha, M. R. Haas, J. Catanzarite, J. F. Rowe, G. Barentsen, D. A. Caldwell, B. D. Clarke, J. M. Jenkins, J. Li, D. W. Latham, J. J. Lissauer, S. Mathur, R. L. Morris, S. E. Seader, J. C. Smith, T. C. Klaus, J. D. Twicken, J. E. Van Cleve, B. Wohler, R. Akeson, D. R. Ciardi, W. D. Cochran, C. E. Henze, S. B. Howell, D. Huber, A. Prša, S. V. Ramírez, T. D. Morton, T. Barclay, J. R. Campbell, W. J. Chaplin, D. Charbonneau, J. Christensen-Dalsgaard, J. L. Dotson, L. Doyle, E. W. Dunham, A. K. Dupree, E. B. Ford, J. C. Geary, F. R. Girouard, H. Isaacson, H. Kjeldsen, E. V. Quintana, D. Ragozzine, M. Shabram, A. Shporer, V. Silva Aguirre, J. H. Steffen, M. Still, P. Tenenbaum, W. F. Welsh, A. Wolfgang, K. A. Zamudio, D. G. Koch, and W. J. Borucki, The Astrophysical Journals **235**, 38 (2018).

[7] L. Kreidberg, Publications of the Astronomical Society of the Pacific **127**, 1161 (2015).

[8] K. Mandel and E. Agol, The Astrophysical Journall **580**, L171 (2002).

[9] J. Lillo-Box, D. Barrado, L. Mancini, T. Henning, P. Figueira, S. Ciceri, and N. Santos, Astronomy & Astrophysics **576**, A88 (2015).

[10] H. W. Newton, Vistas in Astronomy **1**, 666 (1955).

[11] R. Howard, P. I. Gilman, and P. A. Gilman, The Astrophysical Journal **283**, 373 (1984).

[12] D. O'Neal, J. E. Neff, and S. H. Saar, The Astrophysical Journal **507**, 919 (1998).

[13] D. O'Neal, J. E. Neff, S. H. Saar, and J. K. Mines, The Astronomical Journal **122**, 1954 (2001).

[14] D. O'Neal, J. E. Neff, S. H. Saar, and M. Cuntz, The Astronomical Journal **128**, 1802 (2004).

[15] B. M. Morris, J. L. Curtis, C. Sakari, S. L. Hawley, and E. Agol, The Astronomical Journal **158**, 101 (2019).

[16] M. Mittag, J. H. M. M. Schmitt, and K. P. Schröder, Astronomy & Astrophysics **618**, A48 (2018).

[17] S. L. Grimm, B.-O. Demory, M. Gillon, C. Dorn, E. Agol, A. Burdanov, L. Delrez, M. Sestovic, A. H. M. J. Triaud, M. Turbet, Bolmont, A. Caldas, J. de Wit, E. Jehin, J. Leconte, S. N. Raymond, V. Van Grootel, A. J. Burgasser, S. Carey, D. Fabrycky, K. Heng, D. M. Hernandez, J. G. Ingalls, S. Lederer, F. Selsis, and D. Queloz, Astronomy and Astrophysics **613**, A68 (2018).

[18] K. Herbst, A. Papaioannou, V. S. Airapetian, and D. Atri, The Astrophysical Journal **907**, 89 (2021).

[19] J. M. Almenara, X. Bonfils, T. Forveille, N. Astudillo-Defru, D. R. Ciardi, R. P. Schwarz, K. A. Collins, M. Cointepas, M. B. Lund, F. Bouchy, D. Charbonneau, R. F. Díaz, X. Delfosse, R. C. Kidwell, M. Kunimoto, D. W. Latham, J. J. Lissauer, F. Murgas, G. Ricker, S. Seager, M. Vezie, and D. Watanabe, arXiv e-prints arXiv:2210.10909 (2022).

[20] O. College, *Astronomy* (Rice University, ADDRESS, 2016).

[21] G. A. Feiden, K. Skidmore, and W.-C. Jao, The Astrophysical Journal **907**, 53 (2021).

[22] C. J. Hansen and S. D. Kawaler, *Stellar Interiors. Physical Principles, Structure, and Evolution.* (Springer-Verlag Berlin Heidelberg New York, ADDRESS, 1994).

[23] S. K. Solanki, Astronomy & Astrophysicsr **11**, 153 (2003).

[24] H. Zirin, *The Astrophysics of the Sun* (Cambridge University Press, ADDRESS, 1998).

[25] D. H. Hathaway and D. P. Choudhary, **250**, 269 (2008).

[26] A. Reiners and G. Basri, The Astrophysical Journal **684**, 1390 (2008).

[27] F. Pont, R. L. Gilliland, C. Moutou, D. Charbonneau, F. Bouchy, T. M. Brown, M. Mayor, D. Queloz, N. Santos, and S. Udry, Astronomy & Astrophysics **476**, 1347 (2007).

[28] A. V. Goncharskii, V. V. Stepanov, V. L. Kokhlova, and A. G. Yagola, Soviet Astronomy Letters **3**, 147 (1977).

[29] J. B. Rice, Astronomische Nachrichten **323**, 220 (2002).

[30] M. Semel, Astronomy & Astrophysics **225**, 456 (1989).

[31] J. F. Donati, M. Semel, B. D. Carter, D. E. Rees, and A. Collier Cameron, Monthly Notices of the Royal Astronomical Society **291**, 658 (1997).

[32] D. O'Neal, S. H. Saar, and J. E. Neff, The Astrophysical Journal **463**, 766 (1996).

[33] S. Catalano, K. Biazzo, A. Frasca, and E. Marilli, Astronomy & Astrophysics **394**, 1009 (2002).

[34] A. Frasca, K. Biazzo, S. Catalano, E. Marilli, S. Messina, and M. Rodonò, Astronomy & Astrophysics **432**, 647 (2005).

[35] D. P. Kiurkchieva, Astrophysics and Space Science **172**, 255 (1990).

[36] D. Charbonneau, T. M. Brown, D. W. Latham, and M. Mayor, The Astrophysical Journal **529**, L45 (2000).

[37] J. R. A. Davenport, L. Hebb, and S. L. Hawley, The Astrophysical Journal **806**, 212 (2015).

[38] M. C. Schutte, L. Hebb, S. Lowry, J. Wisniewski, S. L. Hawley, S. Mahadevan, B. M. Morris, P. Robertson, G. Rohn, and G. Stefansson, The Astronomical Journal **164**, 14 (2022).

[39] D. Foreman-Mackey, D. W. Hogg, D. Lang, and J. Goodman, Publications of the Astronomical Society of the Pacific **125**, 306 (2013).

[40] L. M. Walkowicz, G. Basri, and J. A. Valenti, The Astrophysical Journal Supplement **205**, 17 (2013).

[41] K. Ikuta, H. Maehara, Y. Notsu, K. Namekata, T. Kato, S. Notsu, S. Okamoto, S. Honda, D. Nogami, and K. Shibata, The Astrophysical Journal **902**, 73 (2020).

[42] R. Luger, E. Agol, D. Foreman-Mackey, D. P. Fleming, J. Lustig-Yaeger, and R. Deitrick, The Astronomical Journal **157**, 64 (2019).

[43] J. Salvatier, T. V. Wieckiâ, and C. Fonnesbeck, ascl:1610.016 (2016).

[44] J. E. Libby-Roberts, M. Schutte, L. Hebb, S. Kanodia, C. Canas, G. Stefansson, A. S. J. Lin, S. Mahadevan, W. Parts, L. Powers, J. Wisniewski, C. F. Bender, W. D. Cochran, S. A. Diddams, M. E. Everett, A. F. Gupta, S. Halverson, H. A. Kobulnicky, A. F. Kowalski, A. Larsen, A. Monson, J. P. Ninan, B. A. Parker, L. W. Ramsey, P. Robertson, C. Schwab, T. N. Swaby, and R. C. Terrien, arXiv e-prints arXiv:2302.04757 (2023).

[45] G. Á. Bakos, G. Torres, A. Pál, J. Hartman, G. Kovács, R. W. Noyes, D. W. Latham, D. D. Sasselov, B. Sipőcz, G. A. Esquerdo, D. A. Fischer, J. A. Johnson, G. W. Marcy, R. P. Butler, H. Isaacson, A. Howard, S. Vogt, G. Kovács, J. Fernandez, A. Moór, R. P. Stefanik, J. Lázár, I. Papp, and P. Sári, The Astrophysical Journal **710**, 1724 (2010).

[46] J. N. Winn, J. A. Johnson, A. W. Howard, G. W. Marcy, H. Isaacson, A. Shporer, G. Á. Bakos, J. D. Hartman, and S. Albrecht, The Astrophysical Journall **723**, L223 (2010).

[47] L. A. Balmaceda, S. K. Solanki, N. A. Krivova, and S. Foster, Journal of Geophysical Research (Space Physics) **114**, A07104 (2009).

[48] S. V. Berdyugina, Living Reviews in Solar Physics **2**, 8 (2005).

[49] G. E. Kron, The Astrophysical Journal **115**, 301 (1952).

[50] A. Skumanich, The Astrophysical Journal **171**, 565 (1972).

[51] B. V. Rackham, N. Espinoza, S. V. Berdyugina, H. Korhonen, R. J. MacDonald, B. T. Montet, B. M. Morris, M. Oshagh, A. I. Shapiro, Y. C. Unruh, E. V. Quintana, R. T. Zellem, D. Apai, T. Barclay, J. K. Barstow, G. Bruno, L. Carone, S. L. Casewell, H. M. Cegla, S. Criscuoli, C. Fischer, D. Fournier, M. S. Giampapa, H. Giles, A. Iyer, G. Kopp, N. M. Kostogryz, N. Krivova, M. Mallonn, C. McGruder, K. Molaverdikhani, E. R. Newton, M. Panja, S. Peacock, K. Reardon, R. M. Roettenbacher, G. Scandariato, S. Solanki, K. G. Stassun, O. Steiner, K. B. Stevenson, J. Tregloan-Reed, A. Valio, S. Wedemeyer, L. Welbanks, J. Yu, M. K. Alam, J. R. A. Davenport, D. Deming, C. Dong, E. Ducrot, C. Fisher, E. Gilbert, V. Kostov, M. López-Morales, M. Line, T. Močnik, S. Mullally, R. R. Paudel, I. Ribas, and J. A. Valenti, arXiv e-prints arXiv:2201.09905 (2022).

[52] T. Barclay, V. B. Kostov, K. D. Colón, E. V. Quintana, J. E. Schlieder, D. R. Louie, E. A. Gilbert, and S. E. Mullally, The Astronomical Journal **162**, 300 (2021).

[53] B. Benneke, I. Wong, C. Piaulet, H. A. Knutson, J. Lothringer, C. V. Morley, I. J. M. Crossfield, P. Gao, T. P. Greene, C. Dressing, D. Dragomir, A. W. Howard, P. R. McCullough, E. M. R. Kempton, J. J. Fortney, and J. Fraine, The Astrophysical Journal **887**, L14 (2019).

[54] E. V. Quintana, K. D. Colón, G. Mosby, J. E. Schlieder, P. Supsinskas, J. Karburn, J. L. Dotson, T. P. Greene, C. Hedges, D. Apai, T. Barclay, J. L. Christiansen, N. Espinoza, S. E. Mullally, E. A. Gilbert, K. Hoffman, V. B. Kostov, N. K. Lewis, T. O. Foote, J. Mason, A. Youngblood, B. M. Morris, E. R. Newton, J. Pepper, B. V. Rackham, J. F. Rowe, and K. Stevenson, arXiv e-prints arXiv:2108.06438 (2021).

[55] S. S. Vogt, G. D. Penrod, and A. P. Hatzes, The Astrophysical Journal **321**, 496 (1987).

[56] U. Wolter, J. H. M. M. Schmitt, K. F. Huber, S. Czesla, H. M. Müller, E. W. Guenther, and A. P. Hatzes, Astronomy & Astrophysics **504**, 561 (2009).

[57] Y. Netto and A. Valio, Astronomy & Astrophysics **635**, A78 (2020).

[58] A. Santerne, R. F. Díaz, C. Moutou, F. Bouchy, G. Hébrard, J. M. Almenara, A. S. Bonomo, M. Deleuil, and N. C. Santos, Astronomy & Astrophysics **545**, A76 (2012).

[59] J. Aceituno, S. F. Sánchez, F. Grupp, J. Lillo, M. Hernán-Obispo, D. Benitez, L. M. Montoya, U. Thiele, S. Pedraz, D. Barrado, S. Dreizler, and J. Bean, Astronomy & Astrophysics **552**, A31 (2013).

[60] J. M. Brewer and D. A. Fischer, The Astrophysical Journals **237**, 38 (2018).

[61] A. McQuillan, S. Aigrain, and T. Mazeh, Monthly Notices of the Royal Astronomical Society **432**, 1203 (2013).

[62] R. Cameron and M. Schüssler, The Astrophysical Journal **659**, 801 (2007).

[63] D. Pollacco, I. Skillen, A. Collier Cameron, B. Loeillet, H. C. Stempels, F. Bouchy, N. P. Gibson, L. Hebb, G. Hébrard, Y. C. Joshi, I. McDonald, B. Smalley, A. M. S. Smith, R. A. Street, S. Udry, R. G. West, D. M. Wilson, P. J. Wheatley, S. Aigrain, K. Alsubai, C. R. Benn, V. A. Bruce, D. J. Christian, W. I. Clarkson, B. Enoch, A. Evans, A. Fitzsimmons, C. A. Haswell, C. Hellier, S. Hickey, S. T. Hodgkin, K. Horne, M. Hrudková, J. Irwin, S. R. Kane, F. P. Keenan, T. A. Lister, P. Maxted, M. Mayor, C. Moutou, A. J. Norton, J. P. Osborne, N. Parley, F. Pont, D. Queloz, R. Ryans, and E. Simpson, Monthly Notices of the Royal Astronomical Society **385**, 1576 (2008).

[64] G. Torres, J. Andersen, and A. Giménez, Astronomy & Astrophysicsr **18**, 67 (2010).

[65] A. Claret, Astronomy & Astrophysics **363**, 1081 (2000).

[66] M. Zechmeister and M. Kürster, Astronomy & Astrophysics **496**, 577 (2009).

[67] Y. Suto, S. Sasaki, Y. Nakagawa, and O. Benomar, arXiv e-prints arXiv:2205.04836 (2022).

[68] D. Foreman-Mackey, The Journal of Open Source Software **1**, 24 (2016).

[69] S. V. Berdyugina, A. V. Berdyugin, I. Ilyin, and I. Tuominen, Astronomy & Astrophysics **340**, 437 (1998).

[70] L. Jetsu, J. Pelt, and I. Tuominen, Astronomy & Astrophysics **278**, 449 (1993).

[71] S. V. Berdyugina, J. Pelt, and I. Tuominen, Astronomy & Astrophysics **394**, 505 (2002).

[72] S. V. Berdyugina and I. G. Usoskin, Astronomy & Astrophysics **405**, 1121 (2003).

[73] E. Ducrot, M. Sestovic, B. M. Morris, M. Gillon, A. H. M. J. Triaud, J. De Wit, D. Thimmarayappa, E. Agol, Y. Almleaky, A. Burdanov, A. J. Burgasser, L. Delrez, B. O. Demory, E. Jehin, J. Leconte, J. McCormac, C. Murray, D. Queloz, F. Selsis, S. Thompson, and V. Van Grootel, The Astronomical Journal **156**, 218 (2018).

[74] B. M. Morris, E. Agol, L. Hebb, S. L. Hawley, M. Gillon, E. Ducrot, L. Delrez, J. Ingalls, and B.-O. Demory, The Astrophysical Journal **863**, L32 (2018).

[75] A. Gressier, M. Mori, Q. Changeat, B. Edwards, J. P. Beaulieu, E. Marcq, and B. Charnay, Astronomy & Astrophysics **658**, A133 (2022).

[76] B. M. Morris, E. Agol, J. R. A. Davenport, and S. L. Hawley, The Astrophysical Journal **857**, 39 (2018).

[77] H. R. Wakeford, N. K. Lewis, J. Fowler, G. Bruno, T. J. Wilson, S. E. Moran, J. Valenti, N. E. Batalha, J. Filippazzo, V. Bourrier, S. M. Hörst, S. M. Lederer, and J. de Wit, The Astronomical Journal **157**, 11 (2019).

[78] A. N. Cox and C. A. Pilachowski, Physics Today **53**, 77 (2000).

[79] B. M. Morris, J. L. Curtis, S. T. Douglas, S. L. Hawley, M. A. Agüeros, M. G. Bobra, and E. Agol, The Astronomical Journal **156**, 203 (2018).

[80] A. McQuillan, T. Mazeh, and S. Aigrain, The Astrophysical Journal **211**, 24 (2014).

[81] Y.-C. Kim and P. Demarque, The Astrophysical Journal **457**, 340 (1996).

[82] A. W. Howard, G. W. Marcy, S. T. Bryson, J. M. Jenkins, J. F. Rowe, N. M. Batalha, W. J. Borucki, D. G. Koch, E. W. Dunham, T. N. Gautier, III, J. Van Cleve, W. D. Cochran, D. W. Latham, J. J. Lissauer, G. Torres, T. M. Brown, R. L. Gilliland, L. A. Buchhave, D. A. Caldwell, J. Christensen-Dalsgaard, D. Ciardi, F. Fressin, M. R. Haas, S. B. Howell, H. Kjeldsen, S. Seager, L. Rogers, D. D. Sasselov, J. H. Steffen, G. S. Basri, D. Charbonneau, J. Christiansen, B. Clarke, A. Dupree, D. C. Fabrycky, D. A. Fischer, E. B. Ford, J. J. Fortney, J. Tarter, F. R. Girouard, M. J. Holman, J. A. Johnson, T. C. Klaus, P. Machalek, A. V. Moorhead, R. C. Morehead, D. Ragozzine, P. Tenenbaum, J. D. Twicken, S. N. Quinn, H. Isaacson, A. Shporer, P. W. Lucas, L. M. Walkowicz, W. F. Welsh, A. Boss, E. Devore, A. Gould, J. C. Smith, R. L. Morris, A. Prsa, T. D. Morton, M. Still, S. E. Thompson, F. Mullally, M. Endl, and P. J. MacQueen, The Astrophysical Journal Supplement Series **201**, 15 (2012), aDS Bibcode: 2012ApJS..201...15H.

[83] C. I. Cañas, G. Stefansson, S. Kanodia, S. Mahadevan, W. D. Cochran, M. Endl, P. Robertson, C. F. Bender, J. P. Ninan, C. Beard, J. Lubin, A. F. Gupta, M. E. Everett, A. Monson, R. F. Wilson, H. M. Lewis, M. Brewer, S. R. Majewski, L. Hebb, R. I. Dawson, S. A. Diddams, E. B. Ford, C. Fredrick, S. Halverson, F. Hearty, A. S. J. Lin, A. J. Metcalf, J. Rajagopal, L. W. Ramsey, A. Roy, C. Schwab, R. C. Terrien, and J. T. Wright, The Astronomical Journal **160**, 147 (2020).

[84] S. Kanodia, G. Stefansson, C. I. Cañas, M. Maney, A. S. J. Lin, J. P. Ninan, S. Jones, A. Monson, B. A. Parker, H. A. Kobulnicky, J. Rothenberg, C. Beard, J. Lubin, P. Robertson, A. F. Gupta, S. Mahadevan, W. D. Cochran, C. F. Bender, S. A. Diddams, C. Fredrick, S. Halverson, S. Hawley, F. Hearty, L. Hebb, R. Kopparapu, A. J. Metcalf, L. W. Ramsey, A. Roy, C. Schwab, M. Schutte, R. C. Terrien, J. Wisniewski, and J. T. Wright, The Astronomical Journal **162**, 135 (2021), aDS Bibcode: 2021AJ....162..135K.

[85] A. Jordán, J. D. Hartman, D. Bayliss, G. Bakos, R. Brahm, E. M. Bryant, Z. Csubry, T. Henning, M. Hobson, L. Mancini, K. Penev, M. Rabus, V. Suc, M. de Val-Borro, J. Wallace, K. Barkaoui, D. R. Ciardi, K. A. Collins, E. Esparza-Borges, E. Furlan, T. Gan, M. Ghachoui, M. Gillon, S. Howell, E. Jehin, A. Fukui, K. Kawauchi, J. H. Livingston, R. Luque, R. Matson, E. C. Matthews, H. P. Osborn, F. Murgas, E. Palle, and W. C. Waalkes, (2021), publication Title: arXiv e-prints ADS Bibcode: 2021arXiv211201928J Type: article.

[86] C. I. Cañas, S. Kanodia, C. F. Bender, S. Mahadevan, G. Stefánsson, W. D. Cochran, A. S. J. Lin, L. Powers, A. Monson, E. M. Green, B. A. Parker, T. N. Swaby, H. A. Kobulnicky, J. Wisniewski, A. F. Gupta, M. E. Everett, S. Jones, B. Anjakos, C. Beard, C. H. Blake, S. A. Diddams, Z. Dong, C. Fredrick, E. Hakemiamjad, L. Hebb, J. E.

Libby-Roberts, S. E. Logsdon, M. W. McElwain, A. J. Metcalf, J. P. Ninan, J. Rajagopal, L. W. Ramsey, P. Robertson, A. Roy, J. Ruhle, C. Schwab, R. C. Terrien, and J. T. Wright, (2022), publication Title: arXiv e-prints ADS Bibcode: 2022arXiv220109963C Type: article.

[87] G. Laughlin, P. Bodenheimer, and F. C. Adams, The Astrophysical Journall **612**, L73 (2004).

[88] G. R. Ricker, J. N. Winn, R. Vanderspek, D. W. Latham, G. Á. Bakos, J. L. Bean, Z. K. Berta-Thompson, T. M. Brown, L. Buchhave, N. R. Butler, R. P. Butler, W. J. Chaplin, D. Charbonneau, J. Christensen-Dalsgaard, M. Clampin, D. Deming, J. Doty, N. De Lee, C. Dressing, E. W. Dunham, M. Endl, F. Fressin, J. Ge, T. Henning, M. J. Holman, A. W. Howard, S. Ida, J. M. Jenkins, G. Jernigan, J. A. Johnson, L. Kaltenegger, N. Kawai, H. Kjeldsen, G. Laughlin, A. M. Levine, D. Lin, J. J. Lissauer, P. MacQueen, G. Marcy, P. R. McCullough, T. D. Morton, N. Narita, M. Paegert, E. Palle, F. Pepe, J. Pepper, A. Quirrenbach, S. A. Rinehart, D. Sasselov, B. Sato, S. Seager, A. Sozzetti, K. G. Stassun, P. Sullivan, A. Szentgyorgyi, G. Torres, S. Udry, and J. Villasenor, Journal of Astronomical Telescopes, Instruments, and Systems **1**, 014003 (2015).

[89] S. Kanodia, S. Mahadevan, J. Libby-Roberts, G. Stefansson, C. I. Canas, A. A. A. Piette, A. Boss, J. Teske, J. Chambers, G. Zeimann, A. Monson, P. Robertson, J. P. Ninan, A. S. J. Lin, C. F. Bender, W. D. Cochran, S. A. Diddams, A. F. Gupta, S. Halverson, S. Hawley, H. A. Kobulnicky, A. J. Metcalf, B. A. Parker, L. Powers, L. W. Ramsey, A. Roy, C. Schwab, T. N. Swaby, R. C. Terrien, and J. Wisniewski, arXiv e-prints arXiv:2209.11160 (2022).

[90] X. Bonfils, J. M. Almenara, L. Jocou, A. Wunsche, P. Kern, A. Delboulbé, X. Delfosse, P. Feautrier, T. Forveille, L. Gluck, S. Lafrasse, Y. Magnard, D. Maurel, T. Moulin, F. Murgas, P. Rabou, S. Rochat, A. Roux, and E. Stadler, **9605**, 96051L (2015).

[91] T. M. Brown, N. Baliber, F. B. Bianco, M. Bowman, B. Burleson, P. Conway, M. Crellin, É. Depagne, J. De Vera, B. Dilday, D. Dragomir, M. Dubberley, J. D. Eastman, M. Elphick, M. Falarski, S. Foale, M. Ford, B. J. Fulton, J. Garza, E. L. Gomez, M. Graham, R. Greene, B. Haldeman, E. Hawkins, B. Haworth, R. Haynes, M. Hidas, A. E. Hjelstrom, D. A. Howell, J. Hygelund, T. A. Lister, R. Lobdill, J. Martinez, D. S. Mullins, M. Norbury, J. Parrent, R. Paulson, D. L. Petry, A. Pickles, V. Posner, W. E. Rosing, R. Ross, D. J. Sand, E. S. Saunders, J. Shobbrook, A. Shporer, R. A. Street, D. Thomas, Y. Tsapras, J. R. Tufts, S. Valenti, K. Vander Horst, Z. Walker, G. White, and M. Willis, Publications of the Astronomical Society of the Pacific **125**, 1031 (2013).

[92] F. Pepe, S. Cristiani, R. Rebolo, N. C. Santos, H. Dekker, A. Cabral, P. Di Marcantonio, P. Figueira, G. Lo Curto, C. Lovis, M. Mayor, D. Mégevand, P. Molaro, M. Riva, M. R. Zapatero Osorio, M. Amate, A. Manescau, L. Pasquini, F. M. Zerbi, V. Adibekyan, M. Abreu, M. Affolter, Y. Alibert, M. Aliverti, R. Allart, C. Allende Prieto, D. Álvarez, D. Alves, G. Avila, V. Baldini, T. Bandy, S. C. C. Barros, W. Benz, A. Bianco, F. Borsa, V. Bourrier, F. Bouchy, C. Broeg, G. Calderone, R. Cirami, J. Coelho, P. Conconi, I.

Coretti, C. Cumani, G. Cupani, V. D'Odorico, M. Damasso, S. Deiries, B. Delabre, O. D. S. Demangeon, X. Dumusque, D. Ehrenreich, J. P. Faria, A. Fragoso, L. Genolet, M. Genoni, R. Génova Santos, J. I. González Hernández, I. Hughes, O. Iwert, F. Kerber, J. Knudstrup, M. Landoni, B. Lavie, J. Lillo-Box, J. L. Lizon, C. Maire, C. J. A. P. Martins, A. Mehner, G. Micela, A. Modigliani, M. A. Monteiro, M. J. P. F. G. Monteiro, M. Moschetti, M. T. Murphy, N. Nunes, L. Oggioni, A. Oliveira, M. Oshagh, E. Pallé, G. Pariani, E. Poretti, J. L. Rasilla, J. Rebordão, E. M. Redaelli, S. Santana Tschudi, P. Santin, P. Santos, D. Ségransan, T. M. Schmidt, A. Segovia, D. Sosnowska, A. Sozzetti, S. G. Sousa, P. Spanò, A. Suárez Mascareño, H. Tabernero, F. Tenegi, S. Udry, and A. Zanutta, Astronomy & Astrophysics **645**, A96 (2021).

[93] J. R. A. Davenport, L. Hebb, and S. L. Hawley, The Astrophysical Journal **806**, 212 (2015).

[94] P. Robertson, G. Stefansson, S. Mahadevan, M. Endl, W. D. Cochran, C. Beard, C. F. Bender, S. A. Diddams, N. Duong, E. B. Ford, C. Fredrick, S. Halverson, F. Hearty, R. Holcomb, L. Juan, S. Kanodia, J. Lubin, A. J. Metcalf, A. Monson, J. P. Ninan, J. Palafoutas, L. W. Ramsey, A. Roy, C. Schwab, R. C. Terrien, and J. T. Wright, The Astrophysical Journal **897**, 125 (2020), aDS Bibcode: 2020ApJ...897..125R.

[95] R. Sanchis-Ojeda and J. N. Winn, The Astrophysical Journal **743**, 61 (2011).

[96] M. C. Schutte, L. Hebb, S. Lowry, J. Wisniewski, S. L. Hawley, S. Mahadevan, B. M. Morris, P. Robertson, G. Rohn, and G. Stefansson, The Astronomical Journal **164**, 14 (2022).

[97] B. V. Rackham, D. Apai, and M. S. Giampapa, The Astrophysical Journal **853**, 122 (2018).

[98] C. X. Huang, A. Vanderburg, A. Pál, L. Sha, L. Yu, W. Fong, M. Fausnaugh, A. Shporer, N. Guerrero, R. Vanderspek, and G. Ricker, Research Notes of the AAS **4**, 204 (2020), publisher: American Astronomical Society.

[99] M. Kunimoto, E. Tey, W. Fong, K. Hesse, A. Shporer, M. Fausnaugh, R. Vanderspek, and G. Ricker, Research Notes of the American Astronomical Society **6**, 236 (2022).

[100] Lightkurve Collaboration, J. V. d. M. Cardoso, C. Hedges, M. Gully-Santiago, N. Saunders, A. M. Cody, T. Barclay, O. Hall, S. Sagear, E. Turtelboom, J. Zhang, A. Tzanidakis, K. Mighell, J. Coughlin, K. Bell, Z. Berta-Thompson, P. Williams, J. Dotson, and G. Barentsen, Astrophysics Source Code Library ascl:1812.013 (2018).

[101] J. M. Jenkins, J. D. Twicken, S. McCauliff, J. Campbell, D. Sanderfer, D. Lung, M. Mansouri-Samani, F. Girouard, P. Tenenbaum, T. Klaus, J. C. Smith, D. A. Caldwell, A. D. Chacon, C. Henze, C. Heiges, D. W. Latham, E. Morgan, D. Swade, S. Rinehart, and R. Vanderspek, **9913**, 99133E (2016).

[102] D. A. Caldwell, P. Tenenbaum, J. D. Twicken, J. M. Jenkins, E. Ting, J. C. Smith, C. Hedges, M. M. Fausnaugh, M. Rose, and C. Burke, Research Notes of the American Astronomical Society **4**, 201 (2020).

[103] A. J. Monson, R. L. Beaton, V. Scowcroft, W. L. Freedman, B. F. Madore, J. A. Rich, M. Seibert, J. A. Kollmeier, and G. Clementini, The Astronomical Journal **153**, 96 (2017).

[104] K. A. Collins, J. F. Kielkopf, K. G. Stassun, and F. V. Hessman, The Astronomical Journal **153**, 77 (2017).

[105] G. Stefansson, S. Mahadevan, L. Hebb, J. Wisniewski, J. Huehnerhoff, B. Morris, S. Halverson, M. Zhao, J. Wright, J. O'rourke, H. Knutson, S. Hawley, S. Kanodia, Y. Li, L. M. Z. Hagen, L. J. Liu, T. Beatty, C. Bender, P. Robertson, J. Dembicky, C. Gray, W. Ketzeback, R. McMillan, and T. Rudyk, The Astrophysical Journal **848**, 9 (2017).

[106] N. J. Scott, S. B. Howell, E. P. Horch, and M. E. Everett, Publications of the Astronomical Society of the Pacific **130**, 054502 (2018), aDS Bibcode: 2018PASP..130e4502S.

[107] S. B. Howell, M. E. Everett, W. Sherry, E. Horch, and D. R. Ciardi, The Astronomical Journal **142**, 19 (2011), aDS Bibcode: 2011AJ....142...19H.

[108] Gaia Collaboration, A. G. A. Brown, A. Vallenari, T. Prusti, J. H. J. de Bruijne, C. Babusiaux, M. Biermann, O. L. Creevey, D. W. Evans, L. Eyer, A. Hutton, F. Jansen, C. Jordi, S. A. Klioner, U. Lammers, L. Lindegren, X. Luri, F. Mignard, C. Panem, D. Pourbaix, S. Randich, P. Sartoretti, C. Soubiran, N. A. Walton, F. Arenou, C. A. L. Bailer-Jones, U. Bastian, M. Cropper, R. Drimmel, D. Katz, M. G. Lattanzi, F. van Leeuwen, J. Bakker, C. Cacciari, J. Castañeda, F. De Angeli, C. Ducourant, C. Fabricius, M. Fouesneau, Y. Frémat, R. Guerra, A. Guerrier, J. Guiraud, A. Jean-Antoine Piccolo, E. Masana, R. Messineo, N. Mowlavi, C. Nicolas, K. Nienartowicz, F. Pailler, P. Panuzzo, F. Riclet, W. Roux, G. M. Seabroke, R. Sordo, P. Tanga, F. Thévenin, G. Gracia-Abril, J. Portell, D. Teyssier, M. Altmann, R. Andrae, I. Bellas-Velidis, K. Benson, J. Berthier, R. Blomme, E. Brugaletta, P. W. Burgess, G. Busso, B. Carry, A. Cellino, N. Cheek, G. Clementini, Y. Damerdji, M. Davidson, L. Delchambre, A. Dell'Oro, J. Fernández-Hernández, L. Galluccio, P. García-Lario, M. Garcia-Reinaldos, J. González-Núñez, E. Gosset, R. Haigron, J. L. Halbwachs, N. C. Hambly, D. L. Harrison, D. Hatzidimitriou, U. Heiter, J. Hernández, D. Hestroffer, S. T. Hodgkin, B. Holl, K. Janßen, G. Jevardat de Fombelle, S. Jordan, A. Krone-Martins, A. C. Lanzafame, W. Löffler, A. Lorca, M. Manteiga, O. Marchal, P. M. Marrese, A. Moitinho, A. Mora, K. Muinonen, P. Osborne, E. Pancino, T. Pauwels, J. M. Petit, A. Recio-Blanco, P. J. Richards, M. Riello, L. Rimoldini, A. C. Robin, T. Roegiers, J. Rybizki, L. M. Sarro, C. Siopis, M. Smith, A. Sozzetti, A. Ulla, E. Utrilla, M. van Leeuwen, W. van Reeven, U. Abbas, A. Abreu Aramburu, S. Accart, C. Aerts, J. J. Aguado, M. Ajaj, G. Altavilla, M. A. Álvarez, J. Álvarez Cid-Fuentes, J. Alves, R. I. Anderson, E. Anglada Varela, T. Antoja, M. Audard, D. Baines, S. G. Baker, L. Balaguer-Núñez, E. Balbinot, Z. Balog, C. Barache, D. Barbato, M. Barros, M. A. Barstow, S. Bartolomé, J. L. Bassilana, N. Bauchet, A. Baudesson-Stella, U. Becciani, M. Bellazzini, M. Bernet, S. Bertone, L. Bianchi, S. Blanco-Cuaresma, T. Boch, A. Bombrun, D. Bossini, S. Bouquillon, A. Bragaglia, L. Bramante, E. Breedt, A. Bressan, N. Brouillet, B. Bucciarelli, A. Burlacu, D. Busonero, A. G. Butkevich, R. Buzzi, E. Caffau, R. Cancelliere, H. Cánovas, T. Cantat-Gaudin, R. Carballo, T. Carlucci, M. I.

124

Carnerero, J. M. Carrasco, L. Casamiquela, M. Castellani, A. Castro-Ginard, P. Castro Sampol, L. Chaoul, P. Charlot, L. Chemin, A. Chiavassa, M. R. L. Cioni, G. Comoretto, W. J. Cooper, T. Cornez, S. Cowell, F. Crifo, M. Crosta, C. Crowley, C. Dafonte, A. Dapergolas, M. David, P. David, P. de Laverny, F. De Luise, R. De March, J. De Ridder, R. de Souza, P. de Teodoro, A. de Torres, E. F. del Peloso, E. del Pozo, M. Delbo, A. Delgado, H. E. Delgado, J. B. Delisle, P. Di Matteo, S. Diakite, C. Diener, E. Distefano, C. Dolding, D. Eappachen, B. Edvardsson, H. Enke, P. Esquej, C. Fabre, M. Fabrizio, S. Faigler, G. Fedorets, P. Fernique, A. Fienga, F. Figueras, C. Fouron, F. Fragkoudi, E. Fraile, F. Franke, M. Gai, D. Garabato, A. Garcia-Gutierrez, M. García-Torres, A. Garofalo, P. Gavras, E. Gerlach, R. Geyer, P. Giacobbe, G. Gilmore, S. Girona, G. Giuffrida, R. Gomel, A. Gomez, I. Gonzalez-Santamaria, J. J. González-Vidal, M. Granvik, R. Gutiérrez-Sánchez, L. P. Guy, M. Hauser, M. Haywood, A. Helmi, S. L. Hidalgo, T. Hilger, N. Hładczuk, D. Hobbs, G. Holland, H. E. Huckle, G. Jasniewicz, P. G. Jonker, J. Juaristi Campillo, F. Julbe, L. Karbevska, P. Kervella, S. Khanna, A. Kochoska, M. Kontizas, G. Kordopatis, A. J. Korn, Z. Kostrzewa-Rutkowska, K. Kruszyńska, S. Lambert, A. F. Lanza, Y. Lasne, J. F. Le Campion, Y. Le Fustec, Y. Lebreton, T. Lebzelter, S. Leccia, N. Leclerc, I. Lecoeur-Taibi, S. Liao, E. Licata, E. P. Lindstrøm, T. A. Lister, E. Livanou, A. Lobel, P. Madrero Pardo, S. Managau, R. G. Mann, J. M. Marchant, M. Marconi, M. M. S. Marcos Santos, S. Marinoni, F. Marocco, D. J. Marshall, L. Martin Polo, J. M. Martín-Fleitas, A. Masip, D. Massari, A. Mastrobuono-Battisti, T. Mazeh, P. J. McMillan, S. Messina, D. Michalik, N. R. Millar, A. Mints, D. Molina, R. Molinaro, L. Molnár, P. Montegriffo, R. Mor, R. Morbidelli, T. Morel, D. Morris, A. F. Mulone, D. Munoz, T. Muraveva, C. P. Murphy, I. Musella, L. Noval, C. Ordénovic, G. Orrù, J. Osinde, C. Pagani, I. Pagano, L. Palaversa, P. A. Palicio, A. Panahi, M. Pawlak, X. Peñalosa Esteller, A. Penttilä, A. M. Piersimoni, F. X. Pineau, E. Plachy, G. Plum, E. Poggio, E. Poretti, E. Poujoulet, A. Prša, L. Pulone, E. Racero, S. Ragaini, M. Rainer, C. M. Raiteri, N. Rambaux, P. Ramos, M. Ramos-Lerate, P. Re Fiorentin, S. Regibo, C. Reylé, V. Ripepi, A. Riva, G. Rixon, N. Robichon, C. Robin, M. Roelens, L. Rohrbasser, M. Romero-Gómez, N. Rowell, F. Royer, K. A. Rybicki, G. Sadowski, A. Sagristà Sellés, J. Sahlmann, J. Salgado, E. Salguero, N. Samaras, V. Sanchez Gimenez, N. Sanna, R. Santoveña, M. Sarasso, M. Schultheis, E. Sciacca, M. Segol, J. C. Segovia, D. Ségransan, D. Semeux, S. Shahaf, H. I. Siddiqui, A. Siebert, L. Siltala, E. Slezak, R. L. Smart, E. Solano, F. Solitro, D. Souami, J. Souchay, A. Spagna, F. Spoto, I. A. Steele, H. Steidelmüller, C. A. Stephenson, M. Süveges, L. Szabados, E. Szegedi-Elek, F. Taris, G. Tauran, M. B. Taylor, R. Teixeira, W. Thuillot, N. Tonello, F. Torra, J. Torra, C. Turon, N. Unger, M. Vaillant, E. van Dillen, O. Vanel, A. Vecchiato, Y. Viala, D. Vicente, S. Voutsinas, M. Weiler, T. Wevers, Ł. Wyrzykowski, A. Yoldas, P. Yvard, H. Zhao, J. Zorec, S. Zucker, C. Zurbach, and T. Zwitter, Astronomy & Astrophysics **649**, A1 (2021).

[109] C. Ziegler, A. Tokovinin, C. Briceño, J. Mang, N. Law, and A. W. Mann, The Astronomical Journal **159**, 19 (2020).

[110] V. Belokurov, Z. Penoyre, S. Oh, G. Iorio, S. Hodgkin, N. W. Evans, A. Everall, S. E. Koposov, C. A. Tout, R. Izzard, C. J. Clarke, and A. G. A. Brown, Monthly Notices of the Royal Astronomical Society **496**, 1922 (2020).

[111] S. Mahadevan, L. Ramsey, C. Bender, R. Terrien, J. T. Wright, S. Halverson, F. Hearty, M. Nelson, A. Burton, S. Redman, S. Osterman, S. Diddams, J. Kasting, M. Endl, and R. Deshpande, SPIE **8446**, 84461S (2012), conference Name: Ground-based and Airborne Instrumentation for Astronomy IV Place: eprint: arXiv:1209.1686.

[112] S. Mahadevan, L. W. Ramsey, R. Terrien, S. Halverson, A. Roy, F. Hearty, E. Levi, G. K. Stefansson, P. Robertson, C. Bender, C. Schwab, and M. Nelson, SPIE **9147**, 91471G (2014).

[113] S. Kanodia, S. Mahadevan, L. W. Ramsey, G. K. Stefansson, A. J. Monson, F. R. Hearty, S. Blakeslee, E. Lubar, C. F. Bender, J. P. Ninan, D. Sterner, A. Roy, S. P. Halverson, and P. M. Robertson, SPIE Proceedings **0702**, 107026Q (2018), conference Name: Ground-based and Airborne Instrumentation for Astronomy VII ISBN: 9781510619579 Place: eprint: arXiv:1808.00557.

[114] G. Stefansson, F. Hearty, P. Robertson, S. Mahadevan, T. Anderson, E. Levi, C. Bender, M. Nelson, A. Monson, B. Blank, S. Halverson, C. Henderson, L. Ramsey, A. Roy, C. Schwab, and R. Terrien, The Astrophysical Journal **833**, 175 (2016).

[115] L. W. Ramsey, M. T. Adams, T. G. Barnes, J. A. Booth, M. E. Cornell, J. R. Fowler, N. I. Gaffney, J. W. Glaspey, J. M. Good, G. J. Hill, P. W. Kelton, V. L. Krabbendam, L. Long, P. J. MacQueen, F. B. Ray, R. L. Ricklefs, J. Sage, T. A. Sebring, W. J. Spiesman, and M. Steiner, **3352**, 34 (1998).

[116] J. P. Ninan, C. F. Bender, S. Mahadevan, E. B. Ford, A. J. Monson, K. F. Kaplan, R. C. Terrien, A. Roy, P. M. Robertson, S. Kanodia, and G. K. Stefansson, Proceedings of the SPIE **0709**, 107092U (2018).

[117] S. Kanodia and J. Wright, Research Notes of the AAS **2**, 4 (2018), publisher: American Astronomical Society.

[118] J. T. Wright and J. D. Eastman, Publications of the Astronomical Society of the Pacific **126**, 838 (2014).

[119] G. Anglada-Escudé and R. P. Butler, The Astrophysical Journals **200**, 15 (2012).

[120] M. Zechmeister, S. Dreizler, I. Ribas, A. Reiners, J. A. Caballero, F. F. Bauer, V. J. S. Béjar, L. González-Cuesta, E. Herrero, S. Lalitha, M. J. López-González, R. Luque, J. C. Morales, E. Pallé, E. Rodríguez, C. Rodríguez López, L. Tal-Or, G. Anglada-Escudé, A. Quirrenbach, P. J. Amado, M. Abril, F. J. Aceituno, J. Aceituno, F. J. Alonso-Floriano, M. Ammler-von Eiff, R. Antona Jiménez, H. Anwand-Heerwart, B. Arroyo-Torres, M. Azzaro, D. Baroch, D. Barrado, S. Becerril, D. Benítez, Z. M. Berdiñas, G. Bergond, P. Bluhm, M. Brinkmöller, C. del Burgo, R. Calvo Ortega, J. Cano, C. Cardona Guillén, J. Carro, M. C. Cárdenas Vázquez, E. Casal, N. Casasayas-Barris, V. Casanova, P. Chaturvedi, C. Cifuentes, A. Claret, J. Colomé, M. Cortés-Contreras, S. Czesla, E. Díez-Alonso, R. Dorda, M. Fernández, A. Fernández-Martín, B. Fuhrmeister, A. Fukui, D. Galadí-Enríquez, I. Gallardo Cava, J. Garcia de la Fuente, A. Garcia-Piquer, M. L. García Vargas, L. Gesa, J. Góngora Rueda, E. González-Álvarez, J. I.

González Hernández, R. González-Peinado, U. Grözinger, J. Guàrdia, A. Guijarro, E. de Guindos, A. P. Hatzes, P. H. Hauschildt, R. P. Hedrosa, J. Helmling, T. Henning, I. Hermelo, R. Hernández Arabi, L. Hernández Castaño, F. Hernández Otero, D. Hintz, P. Huke, A. Huber, S. V. Jeffers, E. N. Johnson, E. de Juan, A. Kaminski, J. Kemmer, M. Kim, H. Klahr, R. Klein, J. Klüter, A. Klutsch, D. Kossakowski, M. Kürster, F. Labarga, M. Lafarga, M. Llamas, M. Lampón, L. M. Lara, R. Launhardt, F. J. Lázaro, N. Lodieu, M. López del Fresno, M. López-Puertas, J. F. López Salas, J. López-Santiago, H. Magán Madinabeitia, U. Mall, L. Mancini, H. Mandel, E. Marfil, J. A. Marín Molina, D. Maroto Fernández, E. L. Martín, P. Martín-Fernández, S. Martín-Ruiz, C. J. Marvin, E. Mirabet, P. Montañés-Rodríguez, D. Montes, M. E. Moreno-Raya, E. Nagel, V. Naranjo, N. Narita, L. Nortmann, G. Nowak, A. Ofir, M. Oshagh, J. Panduro, H. Parviainen, J. Pascual, V. M. Passegger, A. Pavlov, S. Pedraz, A. Pérez-Calpena, D. Pérez Medialdea, M. Perger, M. A. C. Perryman, O. Rabaza, A. Ramón Ballesta, R. Rebolo, P. Redondo, S. Reffert, S. Reinhardt, P. Rhode, H.-W. Rix, F. Rodler, A. Rodríguez Trinidad, A. Rosich, S. Sadegi, E. Sánchez-Blanco, M. A. Sánchez Carrasco, A. Sánchez-López, J. Sanz-Forcada, P. Sarkis, L. F. Sarmiento, S. Schäfer, J. H. M. M. Schmitt, P. Schöfer, A. Schweitzer, W. Seifert, D. Shulyak, E. Solano, A. Sota, O. Stahl, S. Stock, J. B. P. Strachan, T. Stuber, J. Stürmer, J. C. Suárez, H. M. Tabernero, M. Tala Pinto, T. Trifonov, G. Veredas, J. I. Vico Linares, F. Vilardell, K. Wagner, V. Wolthoff, W. Xu, F. Yan, and M. R. Zapatero Osorio, Astronomy and Astrophysics **627**, A49 (2019).

[121] G. Stefánsson, R. Kopparapu, A. Lin, S. Mahadevan, C. I. Cañas, S. Kanodia, J. P. Ninan, W. D. Cochran, M. Endl, L. Hebb, J. Wisniewski, A. Gupta, M. Everett, C. F. Bender, S. A. Diddams, E. B. Ford, C. Fredrick, S. Halverson, F. Hearty, E. Levi, M. Maney, A. J. Metcalf, A. Monson, L. W. Ramsey, P. Robertson, A. Roy, C. Schwab, R. C. Terrien, and J. T. Wright, The Astronomical Journal **160**, 259 (2020).

[122] T. D. Morton, ascl:1503.010 (2015).

[123] K. C. Chambers, E. A. Magnier, N. Metcalfe, H. A. Flewelling, M. E. Huber, C. Z. Waters, L. Denneau, P. W. Draper, D. Farrow, D. P. Finkbeiner, C. Holmberg, J. Koppenhoefer, P. A. Price, A. Rest, R. P. Saglia, E. F. Schlafly, S. J. Smartt, W. Sweeney, R. J. Wainscoat, W. S. Burgett, S. Chastel, T. Grav, J. N. Heasley, K. W. Hodapp, R. Jedicke, N. Kaiser, R. P. Kudritzki, G. A. Luppino, R. H. Lupton, D. G. Monet, J. S. Morgan, P. M. Onaka, B. Shiao, C. W. Stubbs, J. L. Tonry, R. White, E. Bañados, E. F. Bell, R. Bender, E. J. Bernard, M. Boegner, F. Boffi, M. T. Botticella, A. Calamida, S. Casertano, W. P. Chen, X. Chen, S. Cole, N. Deacon, C. Frenk, A. Fitzsimmons, S. Gezari, V. Gibbs, C. Goessl, T. Goggia, R. Gourgue, B. Goldman, P. Grant, E. K. Grebel, N. C. Hambly, G. Hasinger, A. F. Heavens, T. M. Heckman, R. Henderson, T. Henning, M. Holman, U. Hopp, W. H. Ip, S. Isani, M. Jackson, C. D. Keyes, A. M. Koekemoer, R. Kotak, D. Le, D. Liska, K. S. Long, J. R. Lucey, M. Liu, N. F. Martin, G. Masci, B. McLean, E. Mindel, P. Misra, E. Morganson, D. N. A. Murphy, A. Obaika, G. Narayan, M. A. Nieto-Santisteban, P. Norberg, J. A. Peacock, E. A. Pier, M. Postman, N. Primak, C. Rae, A. Rai, A. Riess, A. Riffeser, H. W. Rix, S. Röser, R. Russel, L. Rutz, E. Schilbach, A. S. B. Schultz, D. Scolnic, L. Strolger,

A. Szalay, S. Seitz, E. Small, K. W. Smith, D. R. Soderblom, P. Taylor, R. Thomson, A. N. Taylor, A. R. Thakar, J. Thiel, D. Thilker, D. Unger, Y. Urata, J. Valenti, J. Wagner, T. Walder, F. Walter, S. P. Watters, S. Werner, W. M. Wood-Vasey, and R. Wyse, (2016), publication Title: arXiv e-prints ADS Bibcode: 2016arXiv161205560C Type: article.

[124] E. A. Magnier, E. F. Schlafly, D. P. Finkbeiner, J. L. Tonry, B. Goldman, S. Röser, E. Schilbach, S. Casertano, K. C. Chambers, H. A. Flewelling, M. E. Huber, P. A. Price, W. E. Sweeney, C. Z. Waters, L. Denneau, P. W. Draper, K. W. Hodapp, R. Jedicke, N. Kaiser, R. P. Kudritzki, N. Metcalfe, C. W. Stubbs, and R. J. Wainscoat, The Astrophysical Journal Supplement Series **251**, 6 (2020), aDS Bibcode: 2020ApJS..251....6M.

[125] E. L. Wright, P. R. M. Eisenhardt, A. K. Mainzer, M. E. Ressler, R. M. Cutri, T. Jarrett, J. D. Kirkpatrick, D. Padgett, R. S. McMillan, M. Skrutskie, S. A. Stanford, M. Cohen, R. G. Walker, J. C. Mather, D. Leisawitz, I. Gautier, Thomas N., I. McLean, D. Benford, C. J. Lonsdale, A. Blain, B. Mendez, W. R. Irace, V. Duval, F. Liu, D. Royer, I. Heinrichsen, J. Howard, M. Shannon, M. Kendall, A. L. Walsh, M. Larsen, J. G. Cardon, S. Schick, M. Schwalm, M. Abid, B. Fabinsky, L. Naes, and C.-W. Tsai, The Astronomical Journal **140**, 1868 (2010).

[126] R. M. Cutri, M. F. Skrutskie, S. van Dyk, C. A. Beichman, J. M. Carpenter, T. Chester, L. Cambresy, T. Evans, J. Fowler, J. Gizis, E. Howard, J. Huchra, T. Jarrett, E. L. Kopan, J. D. Kirkpatrick, R. M. Light, K. A. Marsh, H. McCallon, S. Schneider, R. Stiening, M. Sykes, M. Weinberg, W. A. Wheaton, S. Wheelock, and N. Zacarias, *2MASS All Sky Catalog of point sources.* (PUBLISHER, ADDRESS, 2003).

[127] G. M. Green, E. Schlafly, C. Zucker, J. S. Speagle, and D. Finkbeiner, The Astrophysical Journal **887**, 93 (2019), aDS Bibcode: 2019ApJ...887...93G.

[128] J. D. Eastman, J. E. Rodriguez, E. Agol, K. G. Stassun, T. G. Beatty, A. Vanderburg, B. S. Gaudi, K. A. Collins, and R. Luger, arXiv e-prints arXiv:1907.09480 (2019).

[129] G. Stefansson, C. Cañas, J. Wisniewski, P. Robertson, S. Mahadevan, M. Maney, S. Kanodia, C. Beard, C. F. Bender, P. Brunt, J. C. Clemens, W. Cochran, S. A. Diddams, M. Endl, E. B. Ford, C. Fredrick, S. Halverson, F. Hearty, L. Hebb, J. Huehnerhoff, J. Jennings, K. Kaplan, E. Levi, E. Lubar, A. J. Metcalf, A. Monson, B. Morris, J. P. Ninan, C. Nitroy, L. Ramsey, A. Roy, C. Schwab, S. Sigurdsson, R. Terrien, and J. T. Wright, The Astronomical Journal **159**, 100 (2020).

[130] A. W. Mann, G. A. Feiden, E. Gaidos, T. Boyajian, and K. von Braun, The Astrophysical Journal **804**, 64 (2015).

[131] X. Bonfils, N. Astudillo-Defru, R. Díaz, J. M. Almenara, T. Forveille, F. Bouchy, X. Delfosse, C. Lovis, M. Mayor, F. Murgas, F. Pepe, N. C. Santos, D. Ségransan, S. Udry, and A. Wünsche, Astronomy & Astrophysics **613**, A25 (2018).

[132] E. R. Newton, J. Irwin, D. Charbonneau, Z. K. Berta-Thompson, J. A. Dittmann, and A. A. West, The Astrophysical Journal **821**, 93 (2016), aDS Bibcode: 2016ApJ...821...93N.

[133] E. R. Newton, J. Irwin, D. Charbonneau, P. Berlind, M. L. Calkins, and J. Mink, The Astrophysical Journal **834**, 85 (2017).

[134] B. R. Roulston, P. J. Green, and A. Y. Kesseli, The Astrophysical Journals **249**, 34 (2020).

[135] H. B. Yuan, X. W. Liu, Z. Y. Huo, M. S. Xiang, Y. Huang, B. Q. Chen, H. H. Zhang, N. C. Sun, C. Wang, H. W. Zhang, Y. H. Zhao, A. L. Luo, J. R. Shi, G. P. Li, H. L. Yuan, Y. Q. Dong, G. W. Li, Y. H. Hou, and Y. Zhang, Monthly Notices of the Royal Astronomical Society **448**, 855 (2015).

[136] M. S. Xiang, X. W. Liu, H. B. Yuan, Z. Y. Huo, Y. Huang, C. Wang, B. Q. Chen, J. J. Ren, H. W. Zhang, Z. J. Tian, Y. Yang, J. R. Shi, J. K. Zhao, J. Li, Y. H. Zhao, X. Q. Cui, G. P. Li, Y. H. Hou, Y. Zhang, W. Zhang, J. L. Wang, Y. Z. Wu, Z. H. Cao, H. L. Yan, T. S. Yan, A. L. Luo, H. T. Zhang, Z. R. Bai, H. L. Yuan, Y. Q. Dong, Y. J. Lei, and G. W. Li, Monthly Notices of the Royal Astronomical Society **467**, 1890 (2017).

[137] K. G. Stassun, R. J. Oelkers, J. Pepper, M. Paegert, N. De Lee, G. Torres, D. W. Latham, S. Charpinet, C. D. Dressing, D. Huber, S. R. Kane, S. Lépine, A. Mann, P. S. Muirhead, B. Rojas-Ayala, R. Silvotti, S. W. Fleming, A. Levine, and P. Plavchan, The Astronomical Journal **156**, 102 (2018).

[138] A. A. Henden, S. Levine, D. Terrell, D. L. Welch, U. Munari, and B. K. Kloppenborg, American Astronomical Society Meeting Abstracts #232 **232**, 223.06 (2018).

[139] D. Foreman-Mackey, R. Luger, E. Agol, T. Barclay, L. Bouma, T. Brandt, I. Czekala, T. David, J. Dong, E. Gilbert, T. Gordon, C. Hedges, D. Hey, B. Morris, A. Price-Whelan, and A. Savel, The Journal of Open Source Software **6**, 3285 (2021).

[140] R. Luger, E. Agol, D. Foreman-Mackey, D. P. Fleming, J. Lustig-Yaeger, and R. Deitrick, The Astronomical Journal **157**, 64 (2019).

[141] M. Rabus, R. Alonso, J. A. Belmonte, H. J. Deeg, R. L. Gilliland, J. M. Almenara, T. M. Brown, D. Charbonneau, and G. Mandushev, Astronomy & Astrophysics **494**, 391 (2009).

[142] T. O. Husser, S. Wende-von Berg, S. Dreizler, D. Homeier, A. Reiners, T. Barman, and P. H. Hauschildt, Astronomy & Astrophysics **553**, A6 (2013).

[143] N. Sugiura, Communications in Statistics - Theory and Methods **7**, 13 (1978).

[144] F. J. Masci, R. R. Laher, B. Rusholme, D. L. Shupe, S. Groom, J. Surace, E. Jackson, S. Monkewitz, R. Beck, D. Flynn, S. Terek, W. Landry, E. Hacopians, V. Desai, J. Howell, T. Brooke, D. Imel, S. Wachter, Q.-Z. Ye, H.-W. Lin, S. B. Cenko, V. Cunningham, U. Rebbapragada, B. Bue, A. A. Miller, A. Mahabal, E. C. Bellm, M. T. Patterson,

M. Jurić, V. Z. Golkhou, E. O. Ofek, R. Walters, M. Graham, M. M. Kasliwal, R. G. Dekany, T. Kupfer, K. Burdge, C. B. Cannella, T. Barlow, A. Van Sistine, M. Giomi, C. Fremling, N. Blagorodnova, D. Levitan, R. Riddle, R. M. Smith, G. Helou, T. A. Prince, and S. R. Kulkarni, Publications of the Astronomical Society of the Pacific **131**, 018003 (2019).

[145] C. S. Kochanek, B. J. Shappee, K. Z. Stanek, T. W. S. Holoien, T. A. Thompson, J. L. Prieto, S. Dong, J. V. Shields, D. Will, C. Britt, D. Perzanowski, and G. Pojmański, Publications of the Astronomical Society of the Pacific **129**, 104502 (2017), aDS Bibcode: 2017PASP..129j4502K.

[146] J. L. Tonry, L. Denneau, A. N. Heinze, B. Stalder, K. W. Smith, S. J. Smartt, C. W. Stubbs, H. J. Weiland, and A. Rest, Publications of the Astronomical Society of the Pacific **130**, 064505 (2018).

[147] R. J. Jackson and R. D. Jeffries, Monthly Notices of the Royal Astronomical Society **423**, 2966 (2012).

[148] X. Dumusque, I. Boisse, and N. C. Santos, The Astrophysical Journal **796**, 132 (2014).

[149] A. Reiners, J. L. Bean, K. F. Huber, S. Dreizler, A. Seifahrt, and S. Czesla, The Astrophysical Journal **710**, 432 (2010).

[150] M.-T. Wang, H.-G. Liu, J. Zhu, and J.-L. Zhou, The Astronomical Journal **162**, 258 (2021).

[151] S. Ida and D. N. C. Lin, The Astrophysical Journal **626**, 1045 (2005).

[152] M. Endl, W. D. Cochran, M. Kürster, D. B. Paulson, R. A. Wittenmyer, P. J. MacQueen, and R. G. Tull, The Astrophysical Journal **649**, 436 (2006).

[153] J. A. Johnson, K. M. Aller, A. W. Howard, and J. R. Crepp, Publications of the Astronomical Society of the Pacific **122**, 905 (2010), aDS Bibcode: 2010PASP..122..905J.

[154] J. Maldonado, E. Villaver, C. Eiroa, and G. Micela, Astronomy & Astrophysics, Volume 624, id.A94, <NUMPAGES>7</NUMPAGES> pp. **624**, A94 (2019).

[155] S. Sabotta, M. Schlecker, P. Chaturvedi, E. W. Guenther, I. M. Rodríguez, J. C. M. Sánchez, J. A. Caballero, Y. Shan, S. Reffert, I. Ribas, A. Reiners, A. P. Hatzes, P. J. Amado, H. Klahr, J. C. Morales, A. Quirrenbach, T. Henning, S. Dreizler, E. Pallé, M. Perger, M. Azzaro, S. V. Jeffers, A. Kaminski, M. Kürster, M. Lafarga, D. Montes, V. M. Passegger, and M. Zechmeister, Astronomy & Astrophysics (2021), arXiv: 2107.03802.

[156] J. B. Pollack, O. Hubickyj, P. Bodenheimer, J. J. Lissauer, M. Podolak, and Y. Greenzweig, Icarus **124**, 62 (1996).

[157] J. J. Fortney, M. S. Marley, and J. W. Barnes, The Astrophysical Journal **659**, 1661 (2007).

[158] E. M. R. Kempton, J. L. Bean, D. R. Louie, D. Deming, D. D. B. Koll, M. Mansfield, J. L. Christiansen, M. López-Morales, M. R. Swain, R. T. Zellem, S. Ballard, T. Barclay, J. K. Barstow, N. E. Batalha, T. G. Beatty, Z. Berta-Thompson, J. Birkby, L. A. Buchhave, D. Charbonneau, N. B. Cowan, I. Crossfield, M. de Val-Borro, R. Doyon, D. Dragomir, E. Gaidos, K. Heng, R. Hu, S. R. Kane, L. Kreidberg, M. Mallonn, C. V. Morley, N. Narita, V. Nascimbeni, E. Pallé, E. V. Quintana, E. Rauscher, S. Seager, E. L. Shkolnik, D. K. Sing, A. Sozzetti, K. G. Stassun, J. A. Valenti, and C. von Essen, Publications of the Astronomical Society of the Pacific **130**, 114401 (2018), aDS Bibcode: 2018PASP..130k4401K.

[159] K. J. Zahnle and M. S. Marley, The Astrophysical Journal **797**, 41 (2014).

[160] E. M. R. Kempton, R. Lupu, A. Owusu-Asare, P. Slough, and B. Cale, Publications of the Astronomical Society of the Pacific **129**, 044402 (2017), aDS Bibcode: 2017PASP..129d4402K.

[161] J. J. Fortney, C. Visscher, M. S. Marley, C. E. Hood, M. R. Line, D. P. Thorngren, R. S. Freedman, and R. Lupu, The Astronomical Journal **160**, 288 (2020), aDS Bibcode: 2020AJ....160..288F.

[162] R. Hu, The Astrophysical Journal **921**, 27 (2021).

[163] K. I. Öberg and R. Wordsworth, The Astronomical Journal **158**, 194 (2019).

[164] D. Turrini, E. Schisano, S. Fonte, S. Molinari, R. Politi, D. Fedele, O. Panić, M. Kama, Q. Changeat, and G. Tinetti, The Astrophysical Journal **909**, 40 (2021).

[165] R. Hobbs, O. Shorttle, and N. Madhusudhan, Monthly Notices of the Royal Astronomical Society **516**, 1032 (2022).

[166] K. I. Öberg, R. Murray-Clay, and E. A. Bergin, The Astrophysical Journall **743**, L16 (2011).

[167] S. Dash, L. Majumdar, K. Willacy, S.-M. Tsai, N. Turner, P. B. Rimmer, M. S. Gudipati, W. Lyra, and A. Bhardwaj, The Astrophysical Journal **932**, 20 (2022).

[168] C. V. Morley, J. J. Fortney, E. M. R. Kempton, M. S. Marley, C. Visscher, and K. Zahnle, The Astrophysical Journal **775**, 33 (2013).

[169] P. Gao, M. S. Marley, K. Zahnle, T. D. Robinson, and N. K. Lewis, The Astronomical Journal **153**, 139 (2017).

[170] S.-M. Tsai, E. K. H. Lee, D. Powell, P. Gao, X. Zhang, J. Moses, E. Hébrard, O. Venot, V. Parmentier, S. Jordan, R. Hu, M. K. Alam, L. Alderson, N. M. Batalha, J. L. Bean, B. Benneke, C. J. Bierson, R. P. Brady, L. Carone, A. L. Carter, K. L. Chubb, J. Inglis, J. Leconte, M. Lopez-Morales, Y. Miguel, K. Molaverdikhani, Z. Rustamkulov, D. K. Sing, K. B. Stevenson, H. R. Wakeford, J. Yang, K. Aggarwal, R. Baeyens, S. Barat, M. d. V. Borro, T. Daylan, J. J. Fortney, K. France, J. M. Goyal, D. Grant, J. Kirk, L. Kreidberg, A. Louca, S. E. Moran, S. Mukherjee, E. Nasedkin, K. Ohno,

B. V. Rackham, S. Redfield, J. Taylor, P. Tremblin, C. Visscher, N. L. Wallack, L. Welbanks, A. Youngblood, E.-M. Ahrer, N. E. Batalha, P. Behr, Z. K. Berta-Thompson, J. Blecic, S. L. Casewell, I. J. M. Crossfield, N. Crouzet, P. E. Cubillos, L. Decin, J.-M. Désert, A. D. Feinstein, N. P. Gibson, J. Harrington, K. Heng, T. Henning, E. M. R. Kempton, J. Krick, P.-O. Lagage, M. Lendl, M. Line, J. D. Lothringer, M. Mansfield, N. J. Mayne, T. Mikal-Evans, E. Palle, E. Schlawin, O. Shorttle, P. J. Wheatley, and S. N. Yurchenko, arXiv e-prints arXiv:2211.10490 (2022).

[171] I. J. M. Crossfield and L. Kreidberg, The Astronomical Journal **154**, 261 (2017).

[172] A. H. Dymont, X. Yu, K. Ohno, X. Zhang, and J. J. Fortney, (2021), publication Title: arXiv e-prints ADS Bibcode: 2021arXiv211206173D Type: article.

[173] X. Yu, C. He, X. Zhang, S. M. Hörst, A. H. Dymont, P. McGuiggan, J. I. Moses, N. K. Lewis, J. J. Fortney, P. Gao, E. M. R. Kempton, S. E. Moran, C. V. Morley, D. Powell, J. A. Valenti, and V. Vuitton, Nature Astronomy **5**, 822 (2021).

[174] Y. Kawashima, R. Hu, and M. Ikoma, The Astrophysical Journall **876**, L5 (2019).

[175] N. E. Batalha, A. Mandell, K. Pontoppidan, K. B. Stevenson, N. K. Lewis, J. Kalirai, N. Earl, T. Greene, L. Albert, and L. D. Nielsen, Publications of the Astronomical Society of the Pacific **129**, 064501 (2017), aDS Bibcode: 2017PASP..129f4501B.

[176] G. Stefànsson, S. Mahadevan, C. Petrovich, J. N. Winn, S. Kanodia, S. C. Millholland, M. Maney, C. I. Cañas, J. Wisniewski, P. Robertson, J. P. Ninan, E. B. Ford, C. F. Bender, C. H. Blake, H. Cegla, W. D. Cochran, S. A. Diddams, J. Dong, M. Endl, C. Fredrick, S. Halverson, F. Hearty, L. Hebb, T. Hirano, A. S. J. Lin, S. E. Logsdon, E. Lubar, M. W. McElwain, A. J. Metcalf, A. Monson, J. Rajagopal, L. W. Ramsey, A. Roy, C. Schwab, H. Schweiker, R. C. Terrien, and J. T. Wright, The Astrophysical Journall **931**, L15 (2022).

[177] V. Bourrier, C. Lovis, H. Beust, D. Ehrenreich, G. W. Henry, N. Astudillo-Defru, R. Allart, X. Bonfils, D. Ségransan, X. Delfosse, H. M. Cegla, A. Wyttenbach, K. Heng, B. Lavie, and F. Pepe, Nature **553**, 477 (2018).

[178] C. Petrovich, D. J. Muñoz, K. M. Kratter, and R. Malhotra, The Astrophysical Journall **902**, L5 (2020).

[179] S. W. Yee, E. A. Petigura, B. J. Fulton, H. A. Knutson, K. Batygin, G. Á. Bakos, J. D. Hartman, L. A. Hirsch, A. W. Howard, H. Isaacson, M. R. Kosiarek, E. Sinukoff, and L. M. Weiss, The Astronomical Journal **155**, 255 (2018).

[180] C. Piaulet, B. Benneke, R. A. Rubenzahl, A. W. Howard, E. J. Lee, D. Thorngren, R. Angus, M. Peterson, J. E. Schlieder, M. Werner, L. Kreidberg, T. Jaouni, I. J. M. Crossfield, D. R. Ciardi, E. A. Petigura, J. Livingston, C. D. Dressing, B. J. Fulton, C. Beichman, J. L. Christiansen, V. Gorjian, K. K. Hardegree-Ullman, J. Krick, and E. Sinukoff, The Astronomical Journal **161**, 70 (2021).

[181] S. H. Albrecht, R. I. Dawson, and J. N. Winn, Publications of the Astronomical Society of the Pacific **134**, 082001 (2022).

[182] H. A. C. Giles, A. Collier Cameron, and R. D. Haywood, Monthly Notices of the Royal Astronomical Society **472**, 1618 (2017).

[183] G. Basri, T. Streichenberger, C. McWard, I. Edmond, Lawrence, J. Tan, M. Lee, and T. Melton, The Astrophysical Journal **924**, 31 (2022).

[184] B. M. Morris, The Astrophysical Journal **893**, 67 (2020).

[185] W. S. Howard, J. Teske, H. Corbett, N. M. Law, S. X. Wang, J. K. Ratzloff, N. W. Galliher, R. Gonzalez, A. V. Soto, A. L. Glazier, and J. Haislip, The Astronomical Journal **162**, 147 (2021).

[186] K. Namekata, J. R. A. Davenport, B. M. Morris, S. L. Hawley, H. Maehara, Y. Notsu, S. Toriumi, K. Ikuta, S. Notsu, S. Honda, D. Nogami, and K. Shibata, The Astrophysical Journal **891**, 103 (2020).

[187] A. R. G. Santos, S. Mathur, R. A. García, A. M. Broomhall, R. Egeland, A. Jiménez, D. Godoy-Rivera, S. N. Breton, Z. R. Claytor, T. S. Metcalfe, M. S. Cunha, and L. Amard, Astronomy & Astrophysics **672**, A56 (2023).

[188] G. R. Ricker, J. N. Winn, R. Vanderspek, D. W. Latham, G. Á. Bakos, J. L. Bean, Z. K. Berta-Thompson, T. M. Brown, L. Buchhave, N. R. Butler, R. P. Butler, W. J. Chaplin, D. Charbonneau, J. Christensen-Dalsgaard, M. Clampin, D. Deming, J. Doty, N. De Lee, C. Dressing, E. W. Dunham, M. Endl, F. Fressin, J. Ge, T. Henning, M. J. Holman, A. W. Howard, S. Ida, J. M. Jenkins, G. Jernigan, J. A. Johnson, L. Kaltenegger, N. Kawai, H. Kjeldsen, G. Laughlin, A. M. Levine, D. Lin, J. J. Lissauer, P. MacQueen, G. Marcy, P. R. McCullough, T. D. Morton, N. Narita, M. Paegert, E. Palle, F. Pepe, J. Pepper, A. Quirrenbach, S. A. Rinehart, D. Sasselov, B. Sato, S. Seager, A. Sozzetti, K. G. Stassun, P. Sullivan, A. Szentgyorgyi, G. Torres, S. Udry, and J. Villasenor, Journal of Astronomical Telescopes, Instruments, and Systems **1**, 014003 (2015).

[189] G. Stefansson, S. Mahadevan, L. Hebb, J. Wisniewski, J. Huehnerhoff, B. Morris, S. Halverson, M. Zhao, J. Wright, J. O'rourke, H. Knutson, S. Hawley, S. Kanodia, Y. Li, L. M. Z. Hagen, L. J. Liu, T. Beatty, C. Bender, P. Robertson, J. Dembicky, C. Gray, W. Ketzeback, R. McMillan, and T. Rudyk, The Astrophysical Journal **848**, 9 (2017).

[190] K. A. Collins, J. F. Kielkopf, K. G. Stassun, and F. V. Hessman, The Astronomical Journal **153**, 77 (2017).

[191] B. Rojas-Ayala, K. R. Covey, P. S. Muirhead, and J. P. Lloyd, The Astrophysical Journal **748**, 93 (2012).